Graphene-based materials: Synthesis and gas sorption, storage and separation

CrossMark

Srinivas Gadipelli*, Zheng Xiao Guo*

Department of Chemistry, University College London, 20 Gordon Street, London WC1H 0AJ, United Kingdom

A R T I C L E   I N F O

A B S T R A C T

Graphene-based materials have generated tremendous interest in a wide range of research activities. A wide variety of graphene related materials have been synthesised for potential applications in electronics, energy storage, catalysis, and gas sorption, storage, separation and sensing. Recently, gas sorption, storage and separation in porous nanocarbons and metal–organic frameworks have received increasing attention. In particular, the tuneable porosity, surface area and functionality of the lightweight and stable graphene-based materials open up great scope for those applications. Such structural features can be achieved by the design and control of the synthesis routes. Here, we highlight recent progresses and challenges in the syntheses of graphene-based materials with hierarchical pore structures, tuneable high surface area, chemical doping and surface functionalization for gas (H_2, CH_4, CO_2, N_2, NH_3, NO_2, H_2S, SO_2, etc.) sorption, storage and separation.

Contents

---

* Corresponding authors.
  E-mail addresses: gsrinivasphys@gmail.com (S. Gadipelli), z.x.guo@ucl.ac.uk (Z.X. Guo).

1. Introduction

Graphene is a two-dimensional (2D) sp^2 bonded carbon sheet, arranged in a hexagonal honeycomb lattice [1–4]. From a fundamental point of view, graphene is nothing but a single layer of graphite, which is an infinite three-dimensional (3D) material made up of stacked layers of graphene. The layers in graphite interact weakly through van der Waals (vdW) forces. In terms of properties graphene is unique; it is a soft membrane and at the same time possesses a high Young's modulus, and good thermal and electrical conductivities [4–6]. In addition, a single-layer graphene is a zero band gap material and highly transparent, exhibits optical transmittance of 97.7%. With its high theoretical specific surface area of ~2600 m^2/g graphene provides a rich platform for surface chemistry [7–12]. The combined extraordinary physical and chemical properties of graphene, in turn, has ignited extensive research in nanoelectronics, supercapacitors, fuel-cells, batteries, photovoltaics, catalysis, gas sorption, separation and storage, and sensing [13–28]. A roadmap of graphene materials is described in a recent review [4]. It is important to note that most of the graphene properties are sensitive to structural defects and the number of layers [4,29–31]. Thus in order to exploit most of the proposed applications, the synthesis routes and conditions is important in tuning the structure and properties of graphene. There are a number of reviews on graphene related materials for possible applications in relation to optical, electronic, photocatalytic and electrochemical properties [1–50]. However, there is a lack of consideration on their important molecular interactions, e.g. for molecular adsorption and storage. This article attempts to address such issues.

Several large scale processing methods have been involved for different graphene based materials through either graphitic top-down or molecular carbon precursor bottom-up approaches, as summarised in Fig. 1. The flexibility in modification and functionalization of the graphene surface has opened up many possibilities for the development of tailored functional materials. For example, surface modification has been applied to tune the band-gap of single-layer graphene for microelectronic devices. Similarly, the intrinsic non-porous 2D graphene is tuned to highly porous 3D architectures for electrochemical devises (batteries, fuel-cells and supercapacitors) and gas sorption, storage, separation and sensing.

On a relatively large scale, graphene is mostly obtained from graphite precursors through oxidation–exfoliation–reduction, i.e. in the form of graphene oxide (GO) as schematically shown in Fig. 1a [4,33,49–52]. The GO structure contains abundant oxygen-rich functional groups; hydroxide and epoxide groups on the basal plane and carbonyl and carboxyl groups on edges of the graphene
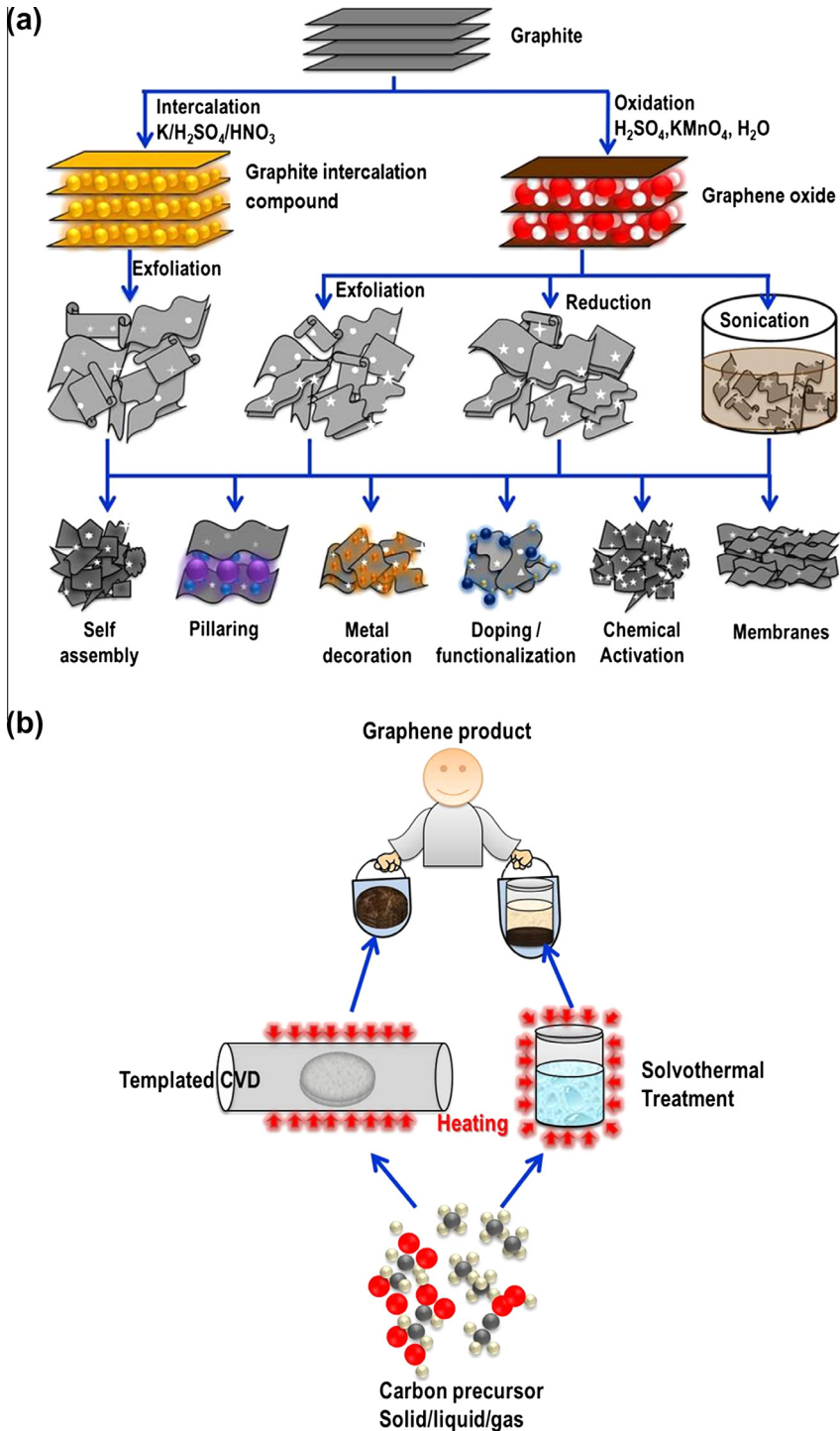
Fig. 1. (a) Graphitic top-down approach and (b) molecular carbon precursor bottom-up approach for producing wide variety of graphene based materials in large quantities.

sheets. Thus the GO is hydrophilic in nature and soluble in water and several solvents. GO with its lamellar water, a largely expanded and tuneable layer structure provides a rich platform for engineering a wide range of functionalities and reaction sites for chemical modifications. Generally, the oxidation and reduction creates many defective sites on the graphene, which offers clear advantage in gas sorption, storage and separation and further functionalization.

Continued increase in energy demand and the urgency in reducing CO_2 emission require rapid development of alternative and clean energy technologies [53–56]. Efficient ways of storing H_2 [56–63] and capturing CO_2 [54,55,64–72] are key challenges in the development of hydrogen fuel-cell vehicles and carbon capture systems, respectively. Among the different methods, gas sorption and storage by physical adsorption in porous media is considered as a promising approach. Here the gas sorption and storage capacity is mainly governed by a high accessible surface area and pore structure. Many efforts have been made to synthesise a wide variety of tailor-made porous materials, such as zeolites, carbons, polymers, metal–organic frameworks (MOFs), and covalent organic frameworks (COFs) as adsorbents for H_2 and CH_4 storage, and carbon capture and separation from the flue gas [73–82]. The US Department of Energy (DOE) has set certain targets for H_2 and CH_4 storage materials for their practical applications [83–86]. Currently, the on-board H_2 storage targets are: 5.5 wt% (gravimetric) and 40 g/L (volumetric) near ambient temperature. Similarly, a new CH_4 storage program has set the following targets: 0.5 g(CH_4) per g(sorbent) for gravimetric capacity and 11.741 mmol/cm^3 (ρ = 0.188 g/cm^3) for volumetric capacity, which corresponds to the density of compressed natural gas (CNG) at 250 bar and 298 K. The new volumetric target is equal to 263 cm^3 (STP: 273.15 K,
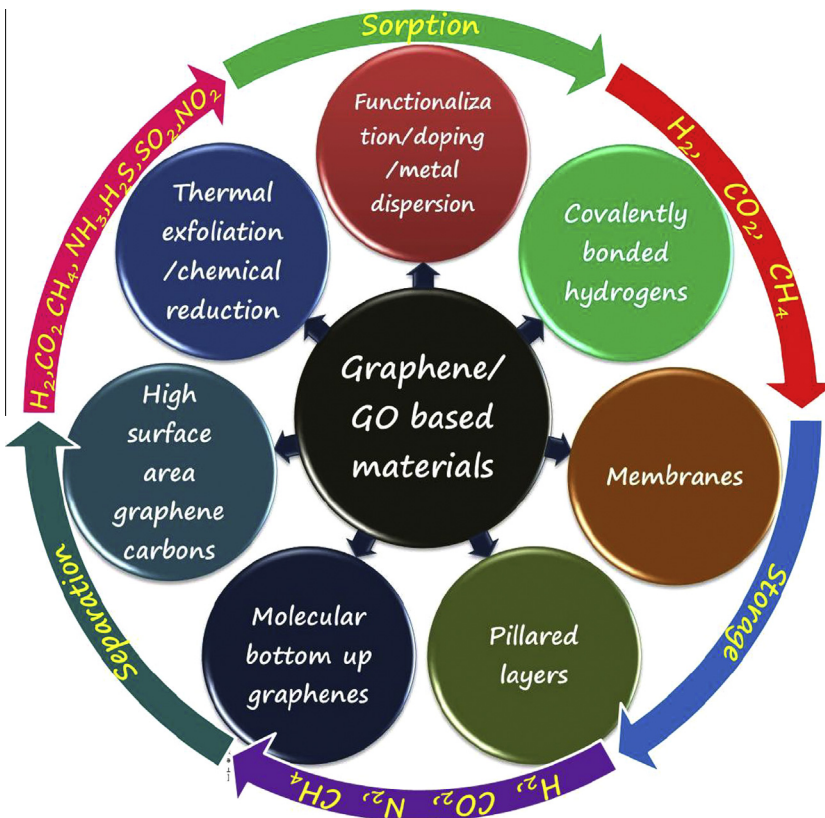

Fig. 2. Graphene based materials for gas sorption, storage and separation.

1 bar) per cm^3, which is significantly higher than the previous target of 180 cm^3 (STP) per cm^3 at 35 bar.

Carbon based materials have been considered for promising gas sorption, storage, and separation because of the abundance, robust pore structure, tuneable porosity and surface area, light-weight, high thermal and chemical stability, and easy synthesis in industrial scale. There is a considerable amount of interest in graphene related materials for gas sorption, storage and separation but still a lack of comprehensive review on such a topic [7,34,36,43,87–89]. Here, we present an up-to-date overview of the theoretical predictions and experimental results on the graphene-based materials towards gas sorption, storage, and separation with particular emphasis on H_2, CO_2, and CH_4. In addition, a detailed account is also provided on the adsorptive removal of toxic gas pollutants, such as NH_3, NO_2, SO_2 and H_2S. Fig. 2 represents the overall overview of graphene-based materials and their possible applications in molecular adsorption and storage.

2. Gas sorption, storage and separation: principles and methodology

Gas sorption, storage and separation in carbon materials are mainly based on physisorption on the surfaces and particularly depend on the electrostatic and dispersion (i.e., vdW) interactions. The former can be tuned by introducing charge variations in the material, and the latter by chemical substitution. The strength of the interaction is determined by the surface characteristics of the adsorbent and the properties of targeted adsorbate molecule, including but not limited to the size and shape of the adsorbate molecule along with its polarizability, magnetic susceptibility, permanent dipole moment, and quadrupole moment. Li et al. summarise the adsorption-related physical parameters of many gas or vapour adsorbates, and herein Table 1 we show a few of those of interest, H_2, N_2, CO, CO_2, CH_4, NH_3, SO_2 and H_2S [90]. For instance, an adsorbent with a high specific surface area is a good candidate for adsorption of a molecule with high polarizability but no polarity. Adsorbents with highly polarised surfaces are good for adsorbate molecules with a high dipole moment. The adsorbents with high electric field gradient surfaces are found to be ideal for the high quadrupole moment adsorbate molecules [91]. Normally, the binding or adsorption strength with a carbon nanostructure is relatively low for H_2 and N_2; intermediate for CO, CH_4 and CO_2; and relatively high for H_2S, NH_3 and H_2O. Thus, surface modifications, such as doping, functionalization and improving the pore structure and specific surface area of nanocarbons, are important to enhance gas adsorption. For this purpose, graphene offers a great scope for tailor-made carbonaceous adsorbents.

Experimentally, at a given temperature, the quantity of adsorbed gas can be determined by an adsorption isotherm, generally carried out by one of the two methods: volumetric or gravimetric. The adsorption isotherm (namely equilibrium isotherm) characterises the adsorption equilibrium. The adsorptive isotherms of individual pure gases are also considered as a promising way to evaluate

Table 1
Some of the physical parameters of selected gaseous adsorbates.

Adsorbate	Normal BP (K)	T_C (K)	V_C (cm^3/ mol)	P_C (bar)	Kinetic diameter (nm)	Polarizability $\times 10^{25}$ (cm^3)	Dipole moment $\times 10^{18}$ (esu cm)	Quadrupole moment $\times 10^{26}$ (esu cm^2)
He	4.30	5.19	57.30	2.27	0.2551	2.04956	0	0
H_2	20.27	32.98	64.20	12.93	0.2827–0.289	8.042	0	0.662
N_2	77.35	126.20	90.10	33.98	0.364–0.380	17.403	0	1.52
O_2	90.17	154.58	73.37	50.43	0.3467	15.812	0	0.39
CO	81.66	132.85	93.10	34.94	0.3690	19.5	0.1098	2.50
CO_2	216.55	304.12	94.07	73.74	0.33	29.11	0	4.30
NO_2	302.22	431.01	–	101.00	–	30.2	0.316	–
SO_2	263.13	430.80	122.00	78.84	0.4112	37.2–42.8	1.633	–
H_2S	212.84	373.40	98.00	89.63	0.3623	37.82–39.5	0.9783	–
NH_3	239.82	405.40	72.47	113.53	0.2900	21.0–28.1	1.4718	–
H_2O	373.15	647.14	55.95	220.64	0.2641	14.5	1.8546	–
CH_4	111.66	190.56	98.60	45.99	0.3758	25.93	0	0

the adsorptive separation. In case of membrane separation, the kinetic diameter of test gas plays an important role, where gas molecules with a kinetic diameter smaller or larger than the membrane pore diameter are separated by molecular sieving. Molecular separation can also be facilitated by large differences in diffusion kinetics across a relatively thick porous membrane.

3. Theoretical insights and predictions

3.1. Hydrogen storage

3.1.1. Expanded and pillared graphene layers

The planar sheet of graphene with its inherent specific surface area of ~2630 m^2/g [92] in the ideal case has further motivated theoretical calculations for gas adsorption from the well-established carbon nanotubes and graphitic structures. The adsorption of a monolayer of H$_2$ on a single side of graphene sheet can lead to about 3 wt% of H$_2$ (H/C = 0.18). However, it is thermodynamically impossible for H$_2$ molecules to penetrate between the graphene layers of graphite. Deng et al. design a Li-doped pillared graphene sheets (Li-PGS) and single-wall carbon nanotubes (Li-P-SWNT) [93]. Grand canonical Monte Carlo (GCMC) simulations predict a H$_2$ storage capacity of 6.5 wt% at 20 bar and room temperature in Li-PGS with a doping ratio of Li:C = 1:3 and an interlayer distance of 1.0 nm (Fig. 3). The Li dopants act as positive (acidic) cores to attract H$_2$ molecules with a binding energy of ~0.3 eV. An interlayer spacing of around 0.6 nm with Li:C = 1:6 leads to over 3 wt% of H$_2$ adsorption. This interlayer spacing [94] or pore width [95] allows H$_2$ molecules to interact both sides of graphene. Thus the spatial distribution of molecular hydrogen adsorption on the graphene plane is very delocalised (Fig. 4). The H$_2$ interaction with graphene in bulk graphite is a localised phenomenon therefore adsorption generally restricted to the outermost graphene plane [96]. A maximum of 3.3 wt% of H$_2$ is achieved with one monolayer adsorption between two graphene layers separated by 0.6 nm (Fig. 4). At most two H$_2$ monolayers could fit between the graphene layers when the layers are separated by 0.9 nm, yielding a maximum capacity of 6.6 wt% of H$_2$. Up to 16 kJ/mol binding energy is obtained for an interlayer distance of ~0.6 nm [94,97,98]. For larger pore widths or interlayer spacing, the binding due to the second graphene layer/surface weakens [95]. For smaller separations, the exchange repulsion reduce the free energy and becomes positive for interlayer separations of <0.5 nm. Thus energetically the H$_2$–graphite system at shorter separations is purely repulsive. The gravimetric and volumetric H$_2$ storage capacities in the C$_{60}$ intercalated graphite (CIG) [99] approach the values obtained for Li-doped graphenes [93] at low temperatures. In another case, a capacity of 3 wt% of H$_2$ is estimated at ambient in ~0.7 nm spaced carbon nanoscrolls followed by alkali doping [100]. First-principles calculations predict 3.4 wt% of H$_2$ and binding energy of (10–22) kJ/mol in the Li and organic molecules (benzene and tetrahydrofuran) co-intercalated graphite with an interlayer
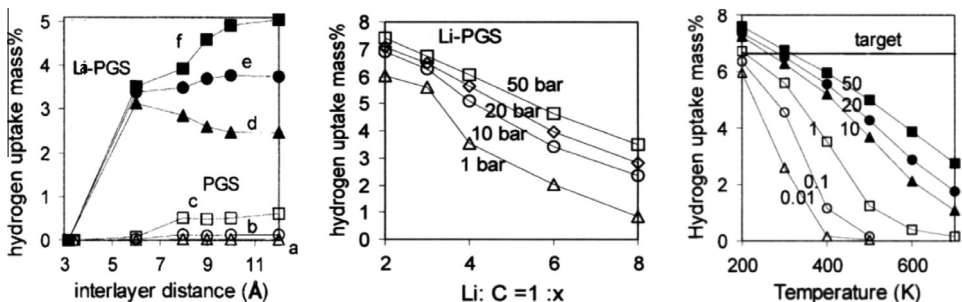
Fig. 3. Left: Dependence of H$_2$ storage capacity on the interlayer distances (ILD) under various pressures for (a) PGS (white) and Li-GIC or Li-PGS (black); the doping concentration is Li:C = 1:6. The pressures are square, 50 bar; circle, 10 bar, and triangle, 1 bar. Middle: Effects of Li-doping concentration on the H$_2$ storage capacity under various pressures. ILD = 1.0 nm. Right: Temperature and pressure (unit: bar) effects on the H$_2$ storage capacity in Li-PGS: Li:C = 1:3 and ILD = 1.0 nm. The horizontal line represents the US Department of Energy (DOE) target [93].
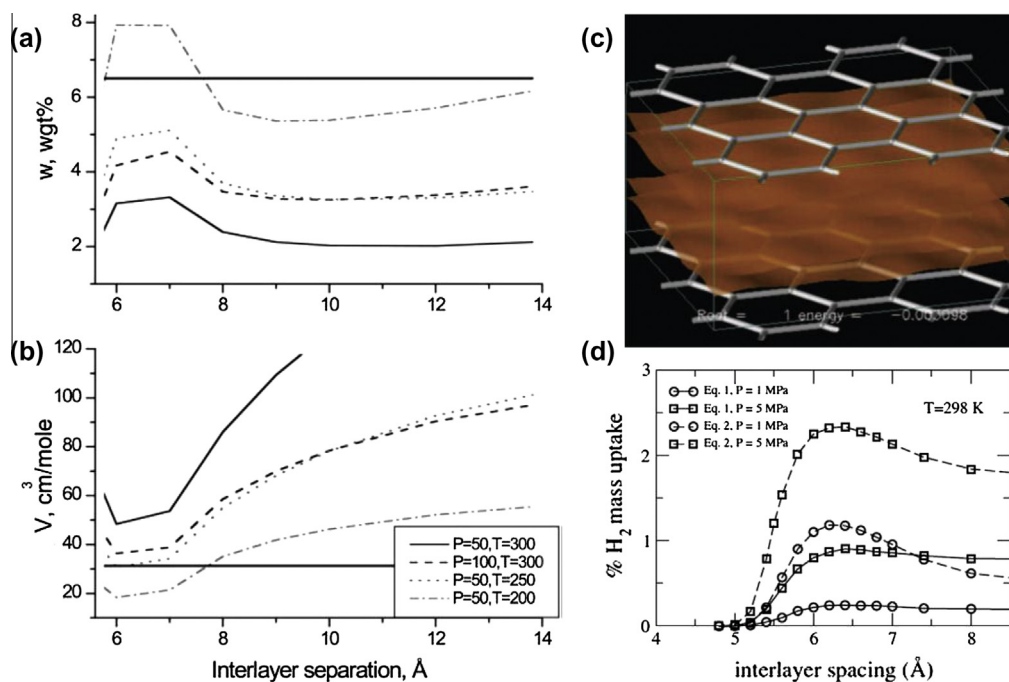
Fig. 4. Gravimetric (a) and volumetric (b) H_2 storage capacities of layered graphite structures, calculated from the real gas equation of state, as a function of interlayer separation. The DOE targets ($w = 6.5\%$, $v = 31.2$ cm^3/mol) are indicated by solid horizontal lines. (c) Storing H_2 between rationally spaced graphene sheets. The figure shows probability densities for selected lowest eigenstates of the translational nuclear Hamiltonian. The lowest in-phase eigenstates for the double-layer structure are shown (interlayer distance of 0.8 nm) [94]. (d) H_2 absorption as a function of graphite interlayer spacing at 298 K for 10 bar (circles) and 50 bar (squares) pressures [95].

graphene distance of ∼0.77 nm [101]. Furthermore, the charged graphenes show enhanced H_2 binding energy up to ∼9 kJ/mol compared to ∼5.8 kJ/mol in a pristine graphene. Similar binding energies are also achieved in Li-doped single-walled carbon nanotube (CNT) pillared graphene structures with intertube and interlayer distance of 1.5 nm and 1.2 nm, respectively [102]. The molecular dynamics simulations estimate H_2 adsorption of up to 6 wt% at 77 K and 3 wt% at 300 K in the CNT pillared graphenes [103].

Furthermore, a detailed analysis and the theoretical limits of H_2 adsorption and storage capacity of slit pores is also presented [104–106]. For example, practicable H_2 adsorption capacity at room temperature is possible for graphene carbons with a slit-pore size between (0.8–1.1) nm, adsorption energy of ⩾15 kJ/mol and a specific surface area of ∼2600 m^2/g. The porous materials with micropores smaller than 0.7 nm are not useful for storage application because of low delivery efficiency and large pores (>1.2 nm) have difficulty in fulfilling the volumetric goals at room temperature. The optimal volumetric storage is expected when the pore volume accommodate 1 or 2 layers of H_2.

3.1.2. Pillared graphene oxide structures

The loosely stacked layers in GO similar to graphite but with a much wider interlayer spacing (0.6–0.9) nm, would be more convenient to store H_2. However, it is very important to consider how accessible is the surface area between graphene layers when the GO layers are stacked together with the presence of surface functional groups and lamellar water molecules [107]. Under normal conditions, GO usually contains different oxy-functional groups, thus not all of the available sp^2 carbons and interlayer spaces are accessible for gas sorption or storage. In recent investigations, some open GO structures are modelled with pillared GO layers, in which further increase in the interlayer distance to

about 1.1 nm is shown as optimal for practicable H_2 storage [107,108]. Burress et al. design a series of idealised pillared-GO model systems with a phenyldiboronic acid linker, called GO frameworks (GOFs) (Fig. 5) [107]. The variation in linker concentration produces different interlayer distances, pore sizes, pore volumes and surface areas. The GOF-32 structure is characterised by one linker per 32 graphene carbons predicted to hold ca. 6.1 wt% of H_2 at 77 K and 1 bar. In another case, Li-doped CNT pillared GO (Li-PGO) model structures with an interlayer distance of 1.1 nm and pore size of 2.3 nm show a gravimetric and volumetric H_2 capacity >10 wt% and 55 g/L, respectively at 77 K and 100 bar [109]. The interaction binding energy of H_2 in the system is ~15.5 kJ/mol. First-principles computations on the Ti-grafted GO show gravimetric and volumetric H_2 storage of 4.9 wt% and 64 g/L, respectively [110]. Similar to the Li in Li-PGO, the Ti atoms bind strongly to the oxygen sites on the GO thus preventing them from clustering. It is also estimated that each Ti binds multiple H_2 molecules with suitable binding energy of (14–41) kJ/mol. The interlayer distance between 1.2 and 1.4 nm shows an optimal volumetric density of (64–74) g/L. First-principles calculations on the covalently bonded graphenes (CBGs) show enhanced H_2 binding energy of 20–150% or more compared to the isolated graphene [111]. The stable porous CBGs are formed through sp^3 carbons at edges of the graphenes. CBGs with adsorbed Ti atoms show ≥4 wt% of H_2 adsorption depending on the pore size and length of the metal chains.

3.1.3. Doped, functionalised and metal dispersed graphenes

Simple graphene-based nanostructures show weak binding energy thus low H_2 adsorption capacity at ambient conditions. Thus chemical doping or structural modifications in the nanostructures has been carried out. A considerable amount of theoretical work has been reported on the modified graphene structures with doping and/or surface metal (alkali: Li, Na, K; alkaline earth: Mg, Ca; simple: B, Al; transition: Sc, Ti, V, Ni, etc.; and noble: Pd, Pt) dispersion. This strategy increases the binding energy and adsorption of H_2 due to the polarisation of H_2 molecules by an electric field and/or hybridization of H_2 σ or σ^* orbitals with transition metal d orbitals (the so-called the Kubas interaction [112]) [112–114]. Lochan and Head-Gordon reported interesting theoretical results, which describes that the ionic
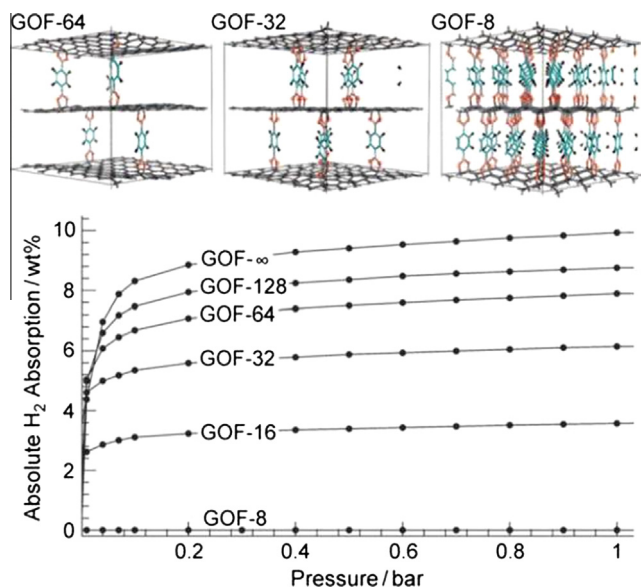

Fig. 5. Top: GCMC simulations for ideal GOF-n structures with n graphene carbons per linker. The structures of three examples with n = 64, 32, and 8. Bottom: The simulated H_2 adsorption isotherms at 77 K for several representative GOF structures [107].

metal atoms, such as Li^+, Na^+, Mg^{2+} and Al^{3+}, hold up to six H_2 molecules with moderate to very strong binding energies between (12–340) kJ/mol, which further depends on the cluster size and complexes [115]. Furthermore, to avoid the issue of structural instability and poor reversibility in metal atomic dispersion (because of the large cohesive energy of bulk transition metals, the aggregation/clustering seems to occur instead of being atomistically dispersed) the structural or chemical defects/doping are introduced in the substrate [111,116,117]. It has been showed that the alkali- and alkaline earth-metal adsorption on graphene surface leads to a metallic state due to charge transfer (Fig. 6) [118,119]. For instance, as shown in Fig. 6, up to 16 wt% of H_2 is predicted in the Li and B adsorbed graphene with a binding energy of ~24 kJ/mol [119–123]. H_2 adsorption of up to 14.4 wt% per molecule with an average binding energy of ~40 kJ/mol in ethylene–Ti complex is estimated [124,125]. A tensile strain of 10% on graphene increases the adsorption energy of Li (Ti) atom by around 75% (71%) and the gravimetric H_2 storage up to 15.4 wt% (9.5 wt%) with an optimal binding energy of about 19 kJ/mol [126]. By controlling the corrugation of individual layers of graphene, the density functional theory (DFT) calculations estimate up to 8 wt% of H_2 [127]. The corrugation of the graphene sheet and the controlled inversion of its curvature show a fast storage (on convex sites) and release (on graphene concave sites) of H_2 at ambient conditions.
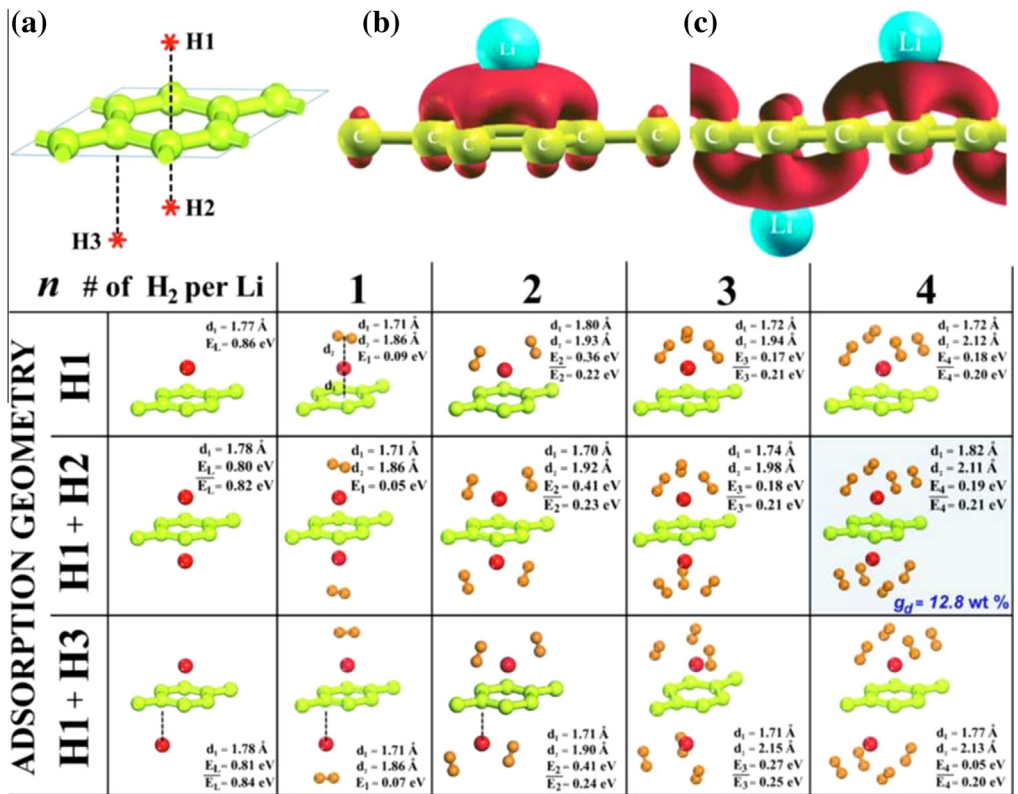
Fig. 6. Top: (a) Various adsorption sites H1, H2 and H3 on the (2×2) cell, (b) charge accumulation, $\Delta\rho^+$, calculated for one Li atom adsorbed to a single side specified as H1, (c) same as (b) for one Li atom adsorbed to H1 site, second Li adsorbed to H3 site of the (2×2) cell of graphene. Bottom: Adsorption sites and energetics of Li adsorbed to the (2×2) cell of graphene and absorption of H_2 molecules by Li atoms. E_L is the binding energy of Li atom adsorbed to H1 site, which is a minimum energy site. For H1 + H2 or H1 + H3 configuration corresponding to double sided adsorption, E_L is the binding energy of second Li atom and $\overline{E}_L$ is the average binding energy. For H1, H1 + H2 and H1 + H3 configurations, $E1$ is the binding energy of the first H_2 absorbed by each Li atom; E_n ($n = 2$–4) is the binding energy of the last nth H_2 molecule absorbed by each Li atom, and $\overline{E}_n$ is the average binding energy of nH_2 molecules absorbed by each Li. Shaded panel indicates the most favourable H_2 absorption configuration [119].

The B-doping is found to form an electron-deficient structure that enhances the H_2 interaction energy [128–131]. The energy surface seems to extend over several graphene carbon sites, making the surface more heterogeneous. B-doping in graphene also enhances the Li and Ca bonding strength on the graphene [130–133]. The DFT calculations estimate approximately (13, 9.9 and 7.9) wt% of H_2 adsorption for the adsorbed Li, Al, and Ti atoms, respectively on the B-doped graphenes [133,134]. Lu et al. show a H_2 adsorption of (6.4 and 6.8) wt% (at 298 K and 100 bar) in a Li- and Ca-decorated B doped (pore rim of polyphenylene) porous graphene (Fig. 7) [135]. Up to 15 wt% of H_2 uptake is predicted in Be adsorbed on B-doped graphene with an average adsorption energy of ∼29 kJ/mol [136]. The H_2 adsorption capacity of 2.4 wt% is also proposed in Si-doped graphene [137].

H_2 adsorption of (6–9) wt% is estimated in the Ca-adsorbed/decorated graphene surfaces [132,138–141]. The Ca adsorption on zigzag edge, porous or covalent-bonded graphenes (CBGs) is also reported [142–144]. CBGs doped with B and decorated with Ca clusters show up to 6 wt% of H_2 adsorption [144]. The Ca atoms prefer to bind more strongly on the sp^3 vertex sites of the pores than to planar graphene sites. This leads to formation of Ca chain structures and exhibit mixed characteristics of multipole Coulomb and Kubas interactions with H_2 molecules depending on the occupation of Ca s or d orbital-derived states. A similar Mg-doped GO shows 5.6 wt% of H_2 adsorption at 200 K [145]. The hydroxyl groups are reduced and Mg atom is bound to the surface of GO by the ring-opening reaction of epoxy in the form of $-(C-O)_x-Mg$ (x = 1, 2). On the surface the positively charged Mg sites and negatively charged O sites produce local electric fields separately to adsorb H_2 molecule with a binding
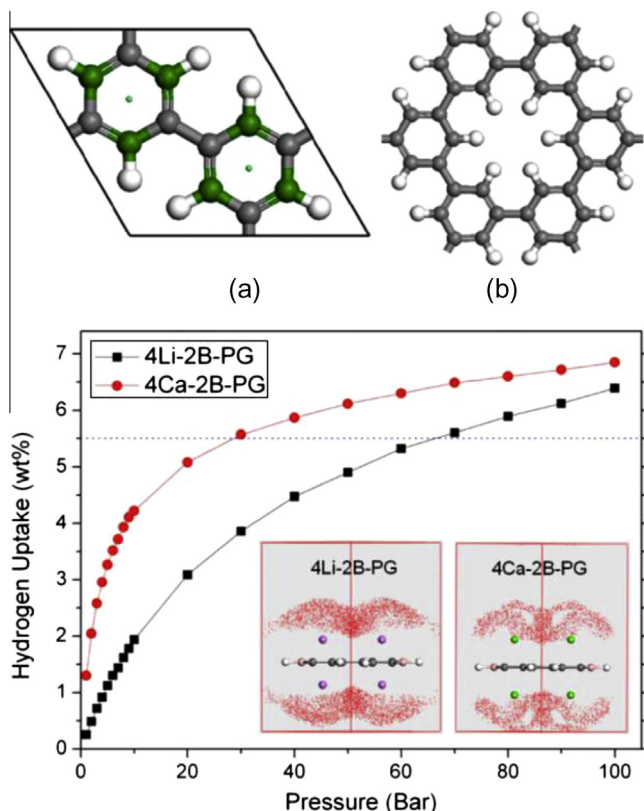
Fig. 7. Top: (a) Unit cell of 2D porous graphene sheet. Grey balls, C; white balls, H; green balls, substitutional sites for B or N doping; small green balls, adsorption sites of Li or Ca above the hexagonal centre. (b) Schematic diagram containing one pore. Bottom: Computed excess gravimetric H_2 adsorption isotherms at 298 K. The dotted line corresponds to the 2017 DOE target. The insets show the snapshots of adsorbed hydrogen molecule density from GCMC simulations at 100 bar and 298 K. Grey balls, C; white balls, H; pink balls, B; purple balls, Li; green balls, Ca [135].

energy of (14.5 and 24) kJ/mol at O and Mg site, respectively. The calculations on Al-doped graphenes also revealed interesting results for H_2 adsorption [146–148].

The H_2 uptake by light transition-metal (LTM = Sc, Ti, V) atom decorated graphenes has also been studied. Each of the LTM atom seems to adsorb on both sides of graphene and hold up to four H_2 molecules to give >6 wt% of H_2 adsorption with the average binding energies between (29–48) kJ/mol [149]. The Sc decorated on either armchair or zigzag edges of graphene nanoribbons show >9 wt% of H_2 adsorption [150]. Ni atomic dispersion on graphene yields about 3 wt% of H_2 but is expected to reduce experimentally due to the clusterization and nanoparticle formation [151].

3.1.4. Graphane based materials

Graphane is nothing but the graphene with alternately covalent bonded hydrogen atoms on each carbon atom on both sides of graphene sheet, as shown in Fig. 8 [152]. Structurally graphane is crumpled, rather than planar, because each hydrogen atom bonded to carbon pulls it a small distance out of the plane. First-principles studies show that the chemisorption of hydrogen on both sides of graphene, i.e., with full coverage of hydrogen (C_nH_n, i.e., 8 wt%) is the lowest energy structure due to the strain associated with the sp^2 to sp^3 conversion [153]. Due to its stable structure and small size, graphane has been also considered as a potential candidate for H_2 storage if doped with alkali- and alkaline-earth metal (M) [154]. The H_2 adsorption mechanism on these doped graphanes is explained by considering the fact that positively charged M^+ ions polarise the H_2 molecules, which are then held to the M^+ ions by the vdW attractive forces. *Ab initio* calculations by Antipina et al. show that the graphane with chemically bonded alkali metals adsorbs up to 12 wt% of H_2, with a binding energy of ∼19 kJ/mol [154]. The calculations by Hussain and Ahuja's group also predict practicable H_2 adsorption in the Li- and Ca-doped graphane with and without strain [152,155,156]. The optimised structure for the case of maximum coverage (5 H_2 molecules, each on both sides of Ca atoms) is shown in Fig. 8.

3.1.5. Hydrogen spillover

The H_2 adsorption by hydrogen spillover is a hydrogen dissociative atomic adsorption, and it has been found to be other alternative to enhance H_2 adsorption in the carbonaceous materials. The spillover is expected in some of the graphene based materials with functionalized/doped structures [157–162]. For example, the stability of hydrogenation states of graphene and conditions for hydrogen spillover are described by Han et al. [161]. The mechanism in metal-doped carbon materials and other solid porous media is explained by George et al. [162]. In brief, it can be explained in three elementary steps as shown in Fig. 9; (i) the activation or dissociation of H_2 molecules on catalytic metal sites, (ii) a
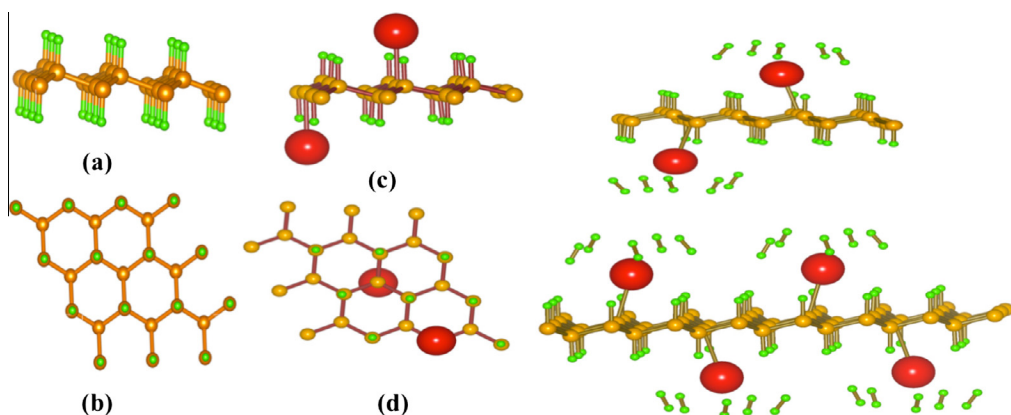
Fig. 8. Left: (a and b) are the side and top view of the optimised structures of pure graphane, respectively, (c and d) show the side and top views of the optimised structures of Ca adsorbed graphane, respectively. Right: The optimised structure of the fully hydrogenated Ca adsorbed graphane with maximum number of hydrogen molecules adsorbed around each Ca atom. The extended structure of relaxed Ca adsorbed graphane with adsorbed H_2 molecules is also shown [152].

transition of atomic hydrogen across the metal–receptor interface, and (iii) the migration of atomic hydrogen throughout the receptor surface. The whole process is denoted as 1, 2; 3, 4; and 5, 6, respectively. The receptor, 'R' is considered inert towards the unactivated H_2 and thus only accepts the activated atomic hydrogen that migrates from the catalyst, 'C'. The receptor surface is expected to be the key that simultaneously provides appropriate thermodynamic stability (binding energy) and kinetic mobility (migration). Fig. 9 also shows stability of the hydrogen chemisorption state of graphene in comparison with the chemical potential of H_2 gas.

Effective dissociation of H_2 molecules into H atoms is observed with the firmly bound catalytic Pt_4 metal cluster on B-doped graphene [160]. The H atoms then migrate from the bridge site of the H-saturated Pt_4 metal to the supporting graphene sheet. By DFT calculations, Cabria et al. reveal that the adsorption and dissociation of H_2 on Pd clusters on the graphene is due to either (a) the adsorption of the H_2 in an activated state or (b) the dissociation of the H_2 and the chemisorption of the two hydrogen atoms [163]. In an activated state, the H_2 bond length is slightly stretched but not broken. The binding energies of the activated H_2 are between (0.4–1) eV/molecule, close to the estimated energies required to obtain reversible H_2 storage at room temperature and moderate pressures. Tight-binding model describes that the C–Pd–H_2 interaction is much weaker than the C–Pd–H bonding [164]. The DFT studies also suggest that the graphene-like materials comprising of curved graphene fragments and many edge atoms, such as microporous carbon, strongly interact with the spillover hydrogen atoms [165]. At 300 K, Li anchored on the graphene vacancies show 6.2 wt% of H_2 dissociative adsorption with a strong binding energy of ~84 kJ/mol [166]. Lueking et al. show that both the B substitutionally doped graphene and hydroxylated graphene satisfies the constraints for reversible room-temperature hydrogenation [167]. A significant enhancement in the binding of H_2 on N-doped graphenes is expected through dissociative adsorption and diffusion on the surface with an externally applied field [168,169]. Under an applied electric field, the N-doped graphenes exhibit a relatively low dissociative adsorption energy barrier for H_2 and low diffusion energy barrier of H atoms.

3.2. CH_4 and CO_2: sorption, storage and separation

Similar to H_2 adsorption, the graphenes with ripples, defects, pores, functional groups, metal dispersion or doping and pillaring also show favourable CH_4 and CO_2 adsorptions [170–181]. The GCMC
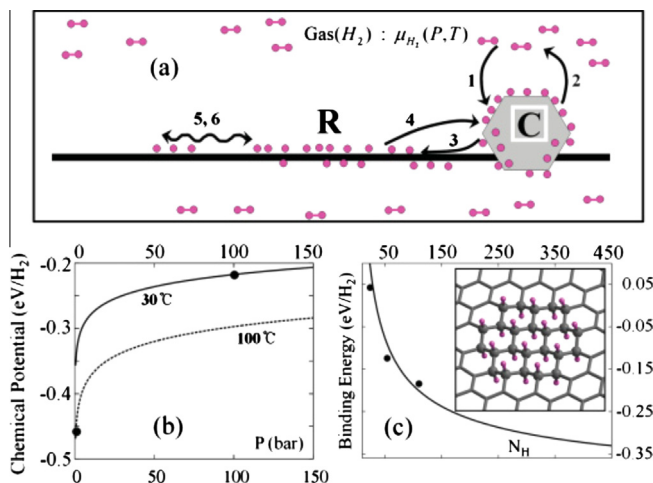
Fig. 9. (a) Schematic description of the H_2 spillover process. C and R indicate the catalytic metal island and the receptor surface, respectively. (b) Chemical potential (eV) of H_2 gas with respect to the zero-temperature static energy of the H_2 molecule. (c) Static chemisorption binding energy (eV) per H_2 onto graphene. The inset shows the chemisorption geometry of 24 hydrogen atoms in the chair-like aggregated configuration. Small (pink) balls represent hydrogen atoms. The carbon atoms to which hydrogen atoms are attached are described with larger grey balls. Other parts of the graphene are denoted only with the wire frame [161].

simulations on fullerene intercalated graphene nano-containers show enhanced CO_2 adsorption with increasing fullerene concentration. The pore with an effective diameter of ca. 0.5 nm is found to be optimum for the effective CO_2 adsorption at low pressures due to the energetically favourable surface interactions [170]. In a relatively large slit-pore, (1.0–2.4) nm the high CO_2 adsorption occurs at relatively high pressures due to multilayer molecular adsorption, similar to the H_2 adsorption characteristics discussed above. In another study, molecular simulations demonstrate the CH_4 adsorption in multilayer graphene nanostructures with and without Li-doping (MGNs and Li-MGNs) and function of interlayer distance [171]. The MGNs and Li-MGNs with an interlayer distance of (0.34–0.51) nm (0.34 + 0.17) show no CH_4 adsorption due to steric effect of the adsorption space, whereas an interlayer distance between (0.68–2.04) nm yield a good CH_4 adsorption (Fig. 10). A maximum uptake of 310 v(STP)/v of CH_4 is obtained at 35 bar, with an adsorption energy of 27.2 kJ/mol. The structures also show a higher H_2S–CH_4 adsorption than CO_2–CH_4 in case of biogas separation. Several main influencing factors for CH_4 storage and acid gas separation in MGNs and Li–MGNs are identified, including the binding energy between gas molecules and substrates, the optimal layer spacing for CH_4 adsorption,
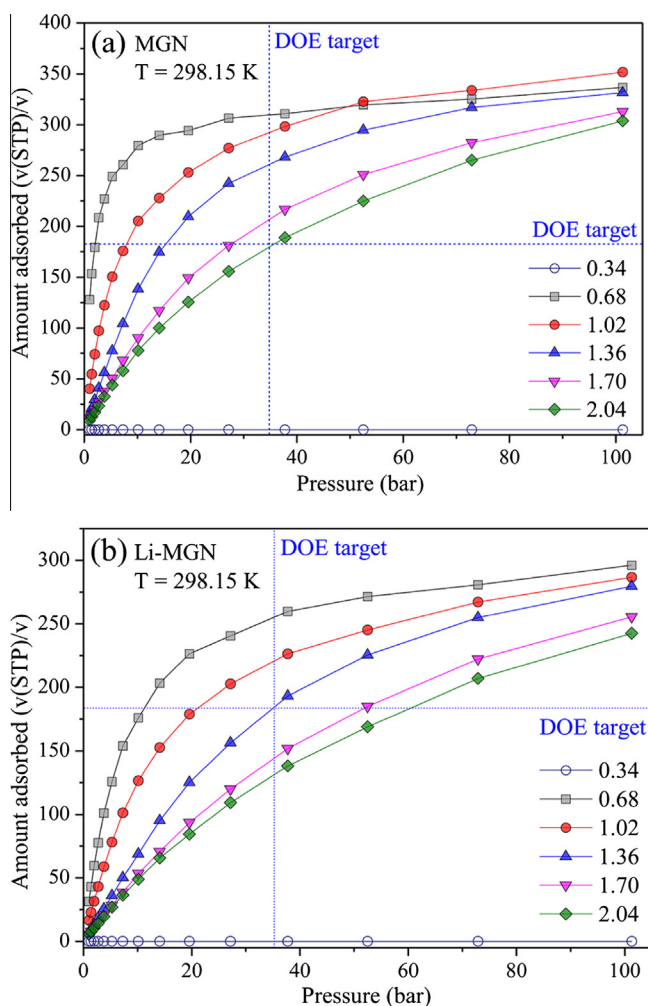

Fig. 10. Comparison of adsorption isotherms of pure CH_4 in (a) MGNs, and (b) Li-MGNs with different graphene layer distances in the range of 0.34–2.04 nm at 298.15 K [171].

and the Li doping strategy. Li cation is able to enhance the binding of CH_4 and H_2S molecules with the graphene substrate surface via nonbonding interactions. The CO_2 molecule interacts with Li cation through chemical bond attributed to the high electronegativity of O atoms.

DFT calculations on the graphene layer modified with Ti at high metal coverage (C_2Ti) show a dissociative and associative adsorptive behaviour for both CO_2 and CH_4, respectively at 300 K and 1 bar [172]. First-principles calculations on the Ti-decorated GO (Ti-GO) show a selective adsorption of CO over CO_2, N_2, CH_4 either in single component or mixture with computed binding energy of ~70 kJ/mol for CO, ~20 kJ/mol for N_2 and <5 kJ/mol for CO_2 and CH_4 [173]. The strong interaction between CO molecule and Ti is a result of dative bond, i.e., hybridization between an empty *d* orbital of Ti and an occupied *p* orbital of CO. The plane-wave electronic DFT calculations suggest that CO_2 binds stronger to the defective site on graphene surface (with one carbon atom missing, i.e., monovacancy) than a perfect graphene with a physisorption energy of ~20 kJ/mol, approximately 4 times stronger than a perfect graphene surface [174]. The adsorption and reactivity of CO_2 on a defective graphene sheet shows strong physisorption energy of ~136 meV [175]. Chemisorption of CO_2 is expected by forming a lactone group with the C atoms surrounding the vacancy after overcoming an energy barrier of ~1 eV. Further dissociation of the CO_2 occurs through the formation of stable epoxy groups with ~614 meV. *Ab initio* and molecular mechanics calculations show that the periodic nature of the vdW potential energy stored between CH_4 and perfect sheet is altered due to the insertion of vacancies (missing lattice atom) and sinusoidal ripples. The CH_4 molecule avoids to be around vacant cites and on top of the peaks [176]. The produced vdW energy surface indicates that around the vacant cites the energy increases. On the perfect graphene, DFT calculations reveal that the adsorption of CH_4 is essentially driven by dispersion interaction with a reasonable binding energy of 0.17 eV [177].

First-principles simulations show the large CO_2 uptake capacities (~0.4–0.6 g CO_2/g sorbent) by decomposition-mediated adsorption in Ca-decorated graphenes [178]. In the CO_2 uptake process, decomposition into CO and formation of CaO is found to be thermodynamically favourable. Thus enhancement in CO_2 adsorption is attributed to a secondary process, where further absorption of CO_2 in a CaO leads to formation of $CaCO_3$. The Ca-decorated graphene also shows an improved CO_2/N_2 selectivity, because of stronger binding of CO_2 than N_2, e.g. 2.731 eV/CO_2 against 0.645 eV/N_2 in case of 12.5% Ca-graphene. Ohba and Kanoh show the edge effects of graphene on Ar, CH_4, N_2, CO_2, and H_2O gas adsorption [179]. The edge sites provide strong Coulombic interactions thus molecules with a strong dipole or quadrupole moment (H_2O or CO_2) are selectively adsorbed on the edge sites. The dispersion interaction-dominated molecules (Ar, CH_4, and N_2) are selectively adsorbed on the basal planes. Furthermore edge functionalized graphenes with the polar groups, including –COOH, –NH_2, –NO_2 and –H_2PO_3, show enhanced CO_2 and CH_4 adsorption due to strong binding of activating exposed edges and terraces [180,181].

3.3. Gas separation membranes

Pristine and porous 2D graphene membranes with and without functionalization have been investigated for gas purification [182]. The pristine graphene is impermeable to He and H_2 [183–185]. Calculations by Miao et al. show that protons can readily pass through a perfect graphene sheet with a low tunnelling barrier compared to a substantially higher barrier for H_2 [184]. Fig. 11 shows initial and final energy states for the tunnelling of an H atom through the centre of a hexagonal carbon ring (hollow site). H_2 is physisorbed at a distance of 0.286 nm with a high energetic activation barrier of 2.86 eV. The tunnelling of an H atom through the benzene ring causes the ring to expand and then contract between a diameter of 0.285 nm and 0.291 nm in the initial/final and transition states, respectively. The strong orbital overlap between the electrons from the H atom and the graphene at −21.62 eV and 2.08 eV for C-2s and H-1s, and C-2p and H-2s respectively, revealing a strong interaction between the H atom and graphene sheet at the transition state (Fig. 11b). The penetration barrier decreases exponentially with the size of the defects, expressed by the number of carbon atoms involved in formation of defect. The potential energy as a function of the distance of an H atom from graphene indicates that a larger defect size result in a smaller penetration barrier. For example, the barrier is reduced largely to 0.66 eV for DV (divacancies) and 1.17 eV for 555–777 (one reconstruction
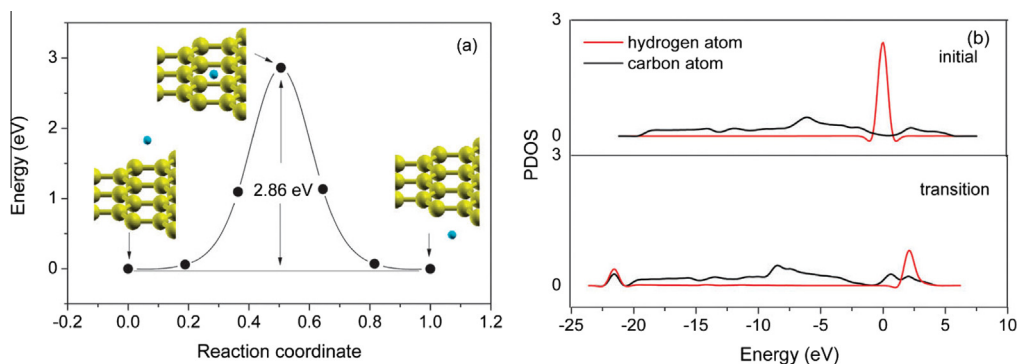
Fig. 11. (a) Reaction energy profile for a hydrogen atom directly penetrating a graphene sheet. (b) PDOS (partial density of states) of initial and transition states for hydrogen penetration (zero energy corresponds to the Fermi level) [184].

from a DV) defects compared to the 2.64 eV of a perfect graphene. For this defect sites the stable states of H atom found at different distances between 0.12 nm and 0.15 nm.

First-principles DFT calculations estimate that the H_2/CH_4 diffusion selectivities are on the order of 10^8 and 10^{23} for the N- and all H-functionalized pores, respectively [186]. The pores are created by the removal of two neighbouring benzene rings on a single-layer graphene. A CO_2/N_2 selectivity of around 300 with a free energy barrier for permeation of 24.7 kJ/mol and 9.6 kJ/mol for CO_2 and N_2, respectively, is reported for the same porous graphene using classical molecular dynamics simulations [187]. A sandwich-like model of porous graphene with the dimensions of 10 nm × 10 nm and the nanopore density of 0.04 per nm^2 shows a linear dependence of flux on CO_2 pressure. The smaller pores of graphene with periodically "one missing" phenyl rings (the polyphenylene unit cell) and line-defect-graphene with missing octagons show a high selectivity for H_2 (e.g., 10^{17} for H_2/CO_2 and 10^{23} for H_2/NH_3) separation from O_2, N_2, NH_3, CH_4, CO_2 and CO, since CO_2, CO and CH_4 has larger kinetic diameter and H_2 is about width of the pore [188–190]. A controllable selectivity and permeable separation of H_2/N_2 is demonstrated in a series of porous graphene membranes with different pore sizes and shapes created by removing 11–16 carbons [191]. For example, the pore size of ∼0.65 nm (pore-16) show best selectivity of N_2 from H_2 because of the vdW interactions with graphene membrane that leads N_2 molecules to distribute within a single molecule layer around the graphene surface. Gas permeation in various limits of gas diffusion, surface adsorption, or pore translocation as the rate-limiting step is described by analytical expressions [192].

First-principles DFT and MD simulations on 0.135 nm pore membrane show a high selectivity for H_2 over other gases with the energy barrier of (0.12, 0.26, 0.25 and 0.82) eV for H_2, N_2, CO and CH_4, respectively [193]. Clearly, it is the electron overlap between the gas molecules and the pore that causes the energy barrier and hinders the molecules from passing through the pores. Thus the energy barrier for gas molecules passing through the membrane generally increases with decreasing pore size or increasing molecule kinetic diameter. Lu et al. demonstrate a high permeable selectivity for H_2 relative to CH_4, CO, and CO_2 in a B or N doped pore rim of (polyphenylene) of porous graphene (PG, one hexagon missing) [135]. The 4B-PG shows a highest selectivity (1.2×10^{78}) for H_2/CH_4 much higher than the PG (6.0×10^{58}) with respective energy barrier of 0.91 eV and 0.68 eV. Substitutional doping leads to a change in the original bond length of PG, where stretching and shortening of the bond is observed by B (BH) and N (NH), respectively. Thus the 3B-PG and 4N-PG with change in pore size possess high selectivity (5.0×10^{37} and 2.0×10^{36}) for H_2/CO (20 times) and H_2/CO_2 (5 orders) respectively, compared to the PG. In the N-doped pore rim graphene (replacement of the unsaturated two C atoms with two N) a Lewis-acid–base type interaction leads to a bound state of CO_2 with a binding energy of about 21 kJ/mol [194], which show no barrier for N_2. Due to similar kinetic diameters and no electric dipole moments, it is difficult to separate CO_2 from N_2; and pore functionalization is needed to enhance the electrostatic interaction. The modified graphene membrane with –CH_3, –OH, –NH_2,

–COOH shows a higher permeability for both N_2 and CO_2 compared to the unmodified one [195]. The results show that the porous graphene membrane with all-N modified pore-16 exhibits a higher CO_2 selectivity over N_2 (∼11) due to the enhanced electrostatic interactions compared to the unmodified graphene membrane. Functional groups also increase the active surface area thereby enhancing the uptake and diffusion onto the membrane surface for more permeation. The CO_2 adsorption ability of functionalized graphene is in the following order: –OH > –COOH > –NH_2 > –CH_3. The porous membrane with carbon atoms bonding to three carbons and to two carbons with hydrogen generates non-uniform charge surfaces and strongly interacts with polar adsorbate molecules. A high selectivity for SO_2 adsorption (SO_2/N_2, SO_2/CO_2) is reported on fluorinated porous graphene due to reduced dispersive interactions, e.g., for CO_2 [196]. Furthermore, in a porous graphene the enhanced diffusion rates of H_2, O_2 and CO_2 up to 2, 5, 9 and 7, 13, 20 orders of magnitude are obtained by application of 10% of the uniaxial tensile strain and symmetrical stretch strain, respectively [197].

Clearly theoretical simulations have offered further insights into the mechanisms of molecular interactions with graphene-based structures. Pristine graphene only show weak binding with most of the molecules. Enhancement of binding interactions can be achieved by careful design of microporosities, surface doping, defect engineering, and high density of edge/boundary defects. However, the binding energy needs to be retained at a level to cause "chemical activation" of the molecules, typically (10–40) kJ/mol, rather than their complete decomposition. Separation of such molecules is another challenge, given the little differences in the kinetic diameters of the molecules of interest. Modifications that can cause preferential binding of a certain molecules are desirable to promote selectivity of the sorbent materials. The following section will examine some of the experimental developments along those directions.

4. Experimental developments

4.1. Chemically reduced/thermally exfoliated graphenes

Graphenes in the bulk quantities have been synthesised by liquid phase oxidation–reduction/exfoliation of graphite (Fig. 1a). The degree of oxidation and exfoliation or reduction conditions yield individual single-layer graphenes to loosely packed multi-layer graphenes with a wide range of pore structures, different degree of residual functional groups and accessible specific surface areas (unless otherwise specified, hereafter the term 'specific surface area (SSA)', is generally determined using the Brunauer, Emmett and Teller (BET) [198] method from nitrogen gas adsorption–desorption isotherm measurement at 77 K). In many cases, the reduction of GO and agglomeration limits the microstructure and SSA. For example, in a report by Ma et al., the graphenes obtained by thermal exfoliation of GO followed by hydrogen reduction show a much limited SSA (156 m^2/g) due to the severe agglomeration of crumpled graphene sheets [199]. The sample adsorbs about (0.4 and 0.2) wt% of H_2 at 77 K and 290 K under 1 bar and 60 bar, respectively. The exfoliated graphenes show an enhanced heat of H_2 adsorption of ∼6 kJ/mol compared to carbon nanofibers and active carbons [200].

A considerably improved SSA and gas sorption in graphenes have been obtained from different post-synthesis treatments of GO. Srinivas et al. report an enhanced SSA (640 m^2/g) in a hydrazine hydrate reduced colloidal suspension of exfoliated GO (Fig. 12) [201]. The sample is characterised with interconnected, wrinkled and disordered graphene sheets with regions of agglomerated multiple layers and a partial restoration of graphitic structure. The gravimetric H_2 uptake measurements at (77–298) K and up to 10 bar show a heat of adsorption of ∼6 kJ/mol at low coverage, and the maximum adsorption of 1.2 wt% at 77 K and 0.1 wt% (and up to 0.72 wt% by extrapolating pressure to 100 bar) at 298 K (Fig. 12). A thermally reduced GO by simple out-gassing at 423 K overnight shows an improved H_2 adsorption of about 1.2 wt% at 77 K and 1 bar with a SSA of 477 m^2/g due to enhanced microporosity and pore volume of ∼1.0 cm^3/g [202]. In another case, a mild chemical reduction of GO with glucose yields a highly enhanced SSA up to 1200 m^2/g with a mesoporous structure [203]. Surprisingly, a high H_2 adsorption of 2.7 wt% at 298 K under 25 bar is obtained, a much higher than for most of the carbon nanostructures. Lee and Park report H_2 uptake of up to 1.8 wt% at 298 K under 100 bar (Fig. 13) in a series of exfoliated GO's by CO_2 pressure swing [204]. GO exfoliation is carried
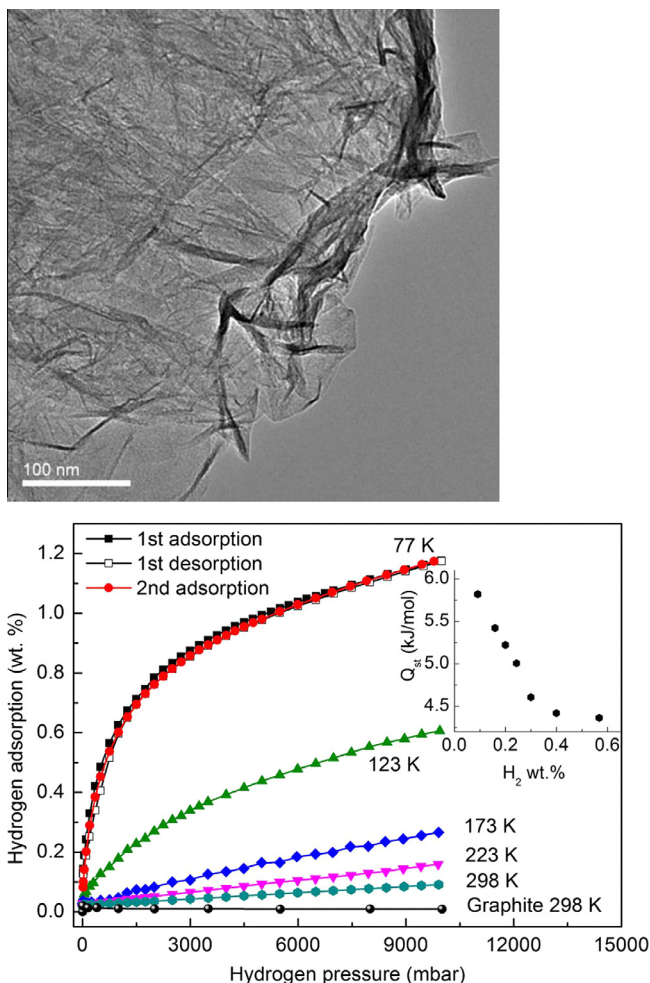
Fig. 12. Top: TEM image of graphene material. Bottom: Hydrogen adsorption–desorption isotherms of graphene material measured at different temperatures and pressures up to 10 bar using gravimetric analyser, for comparison, the hydrogen uptake isotherm for 1–2 μm synthetic graphite powder is also measured. Inset shows the isosteric heat of adsorption of graphene powder [201].

out at 373 K under high pressure of CO_2 up to 40 bar followed by rapid release to vacuum to produce graphenes with a maximum SSA of 547 m^2/g. Magnesium combustion derived graphene sample shows a more or less linear H_2 uptake with increasing H_2 pressure up to 300 bar with the final capacity of 0.9 wt% at 293 K [205]. Bulk graphene sample is produced via high temperature combustion of magnesium in a CO_2 atmosphere using dry ice black, which exhibits a more ordered carbon lattice than other bulk graphenes derived from GO.

Rao's group prepare various types of graphenes from thermal exfoliation of GO (EG), pyrolysis of camphor (CG), and conversion of nanodiamond (DG) [206,207], which shows a wide range of SSA: 46 m^2/g, (280–1013) m^2/g and (639–1550) m^2/g for CG, DG and EG, respectively. H_2 adsorption at 77 K and 1 bar reveals an average linear trend with the SSA, in good agreement with other porous carbons. From this trend, the single-layer graphene, i.e. for the SSA of 2630 m^2/g, is estimated to hold about 3 wt% of H_2, in other words, about 1.2 wt% of H_2 for every 1000 m^2/g of SSA, at 77 K and 1 bar. In addition, a considerably higher H_2 adsorption up to 3 wt% at 298 K and 100 bar is reported.

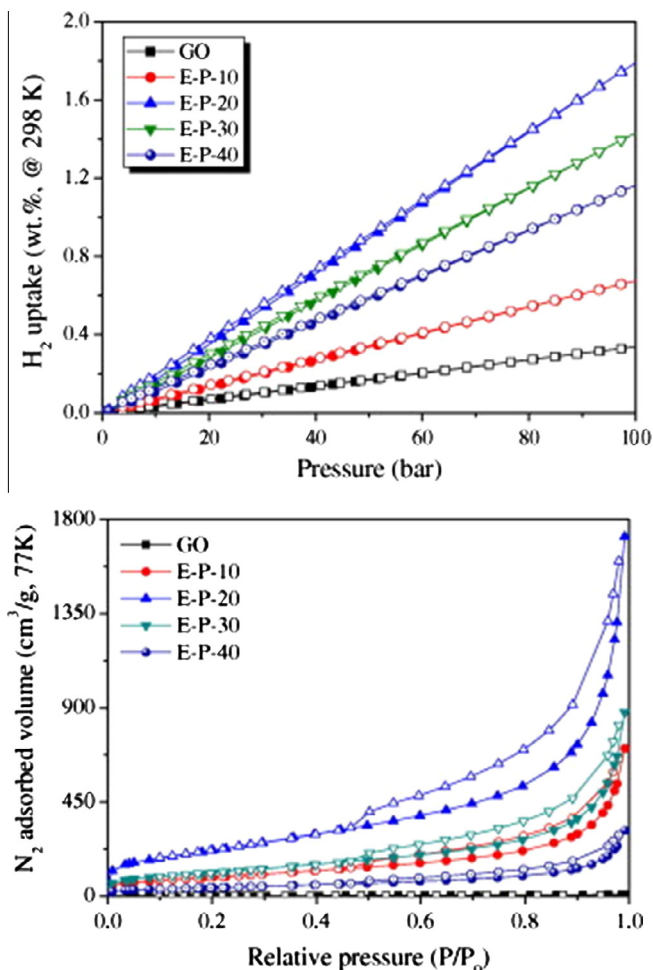**Fig. 13.** H_2 uptake (top) at 298 K and N_2 (bottom) at 77 K adsorption and desorption isotherms of the various exfoliated graphene oxide samples (filled and hollow symbols correspond to the adsorption and desorption profiles). The exfoliated GO samples obtained are designated by the applied pressure (unit: bar), i.e., GO (for the unmodified sample), E-P-10, E-P-20, E-P-30, and E-P-40 [204].

Guo et al. obtain a highly improved H_2 adsorption of 4.0 wt% at 77 K and 1 bar in a hierarchical pore structure graphene with a SSA of 1305 m^2/g [208]. Briefly, the sample is synthesised by exfoliation of GO at 423 K under vacuum followed by further heat treatment at 873 K. The pore structure analysis from the N_2 (at 77 K) and CO_2 (at 273 K) adsorption–desorption isotherm measurements reveal a hierarchical mesopore and ultramicropore structure. This ultra-microporosity leads to an enhanced H_2 uptake at low-pressure as well as a high heat of H_2 adsorption, 9.5 kJ/mol.

The graphene nanoribbons (GNRs) with in-plane and edge sp^2- and sp^3-hybridized carbons show a strong irreversible adsorption of CO_2 (0.22 mmol/g) at 303 K and 1 bar [209]. GNRs are synthesised through CVD via aerosol pyrolysis using ferrocene/thiophene/ethanol precursors. Adsorption of 6.4 mmol/g of CO_2 at 30 bar and 298 K is obtained in a CO_2 pressure swing exfoliated GO with a SSA of 547 m^2/g and a total pore volume of 2.47 cm^3/g [204]. Furthermore, a greatly enhanced CO_2 adsorption of 21.6 mmol/g at 11 bar and 298 K is reported in a hydrogen exfoliated graphene (HEG) with a wide distribution of mesopores and SSA of 443 m^2/g [210]. Surprisingly even higher CO_2

adsorption of up to 56 mmol/g is measured in a vacuum exfoliated GO compared to the maximum of (8, 15 and 39) mmol/g for zeolite-13X, activated carbon and conventional graphene nanosheets, respectively at 298 K and 30 bar (Fig. 14) [211]. The samples exhibit corresponding SSA and total pore volume of (480, 839, 1453 and 701) m^2/g and (1.730, 0.396, 1.382 and 0.727) cm^3/g, respectively. The high CO_2 uptake isotherms in graphene samples exhibit unconventional adsorption behaviour than other porous solids. At low or moderate pressures up to 10 bar, the CO_2 adsorption in graphenes is not comparatively better than others. The improvement at high pressures is linked to the higher interior void volume.

The chemical functionalization and surface grafting of graphenes with basic groups is also demonstrated to obtain increased CO_2 binding and adsorption capacities through enhanced Lewis base–acid interactions [212,213]. Amine-grafted GO synthesised from different amines, including ethylenediamine, diethylenetriamine and triethylene tetramine and aqueous GO by vigorous stirring and reflux at 353 K followed by washing shows about 1.2 mmol/g of CO_2 adsorption in the breakthrough experiments [212]. An unprecedented CO_2 uptake of over 70 mmol/g of CO_2 (at 10 bar and 298 K) is obtained in the HEG–polyaniline composites [213]. However due to the very strong chemical binding of CO_2, the heat treatment under vacuum is necessary to desorb the CO_2.

4.2. Layered graphenes: simple expansion to pillaring with metals and organic ligands

As described in the theoretical predictions there is an optimum interlayer distance between graphene sheets to maximise the H_2 uptake. Such a range of distance reflects the energetically favourable interaction of one H_2 layer between graphene layers. In order to demonstrate the importance of an interlayer distance for effective H_2 storage a variety of hybrid structures have been designed. Below we summarise the experimental results on graphene layer structures synthesised through intercalating various chemical species starting with simple metals/oxides, molecules to organic ligands and combination of these. The best example for this case is the well-known graphite intercalation compounds (GICs) [214–217]. GICs are highly ordered periodic layer structures, known for their very large graphene–graphene inter-layer spacing, made up of layers of foreign atoms/molecules sandwiched between single to n-graphene layers, depending on the stage-n compound. Stage-n represents the n-number of graphene layers present between two intercalated layers. For example, the stage-1 and stage-2 potassium GICs, KC_8 and KC_{24} contains one and two graphene layers between two adjacent potassium intercalated layers (Fig. 15) [218]. This results in increased interlayer distance over 0.540 nm, sufficient to reversibly adsorb H_2 at low temperatures. In particular, the series of stage-2 GICs of stoichiometry MC_{24} (M = K, Rb, Cs) are reversibly and rapidly adsorb H_2 up to ~$2H_2$/M, without dissociation and behaves as a molecular sieve (Fig. 16) [218,219]. The charge transfer to the graphene
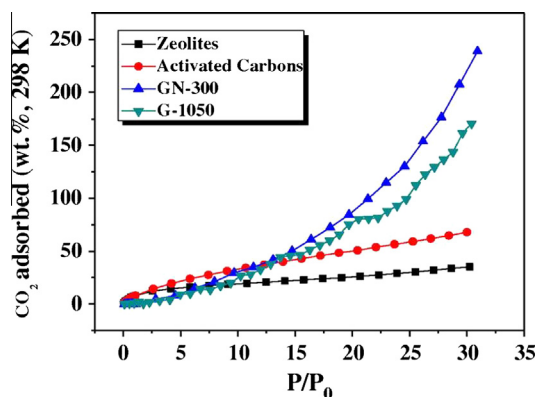

Fig. 14. CO_2 adsorption isotherms of GNs, zeolite-13X, activated carbons, and conventional graphene [211].
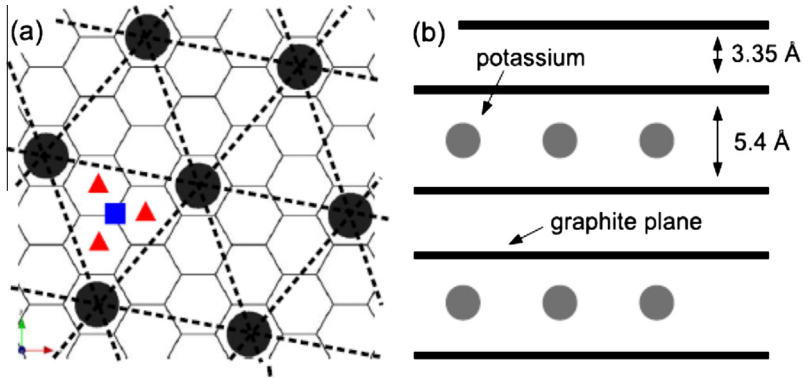
Fig. 15. (a) The $\sqrt{7} \times \sqrt{7}\,R19.11°$ structure, frequently used as an approximation of the low-temperature in-plane arrangement of KC_{24}. This model has a stoichiometry of KC_{28}. The sorption site (blue square) and neighbouring sites (red triangles) are depicted for a single trigonal subunit cell. (b) Schematic side view of a stage-2 alkali-metal graphite intercalation compound [218].
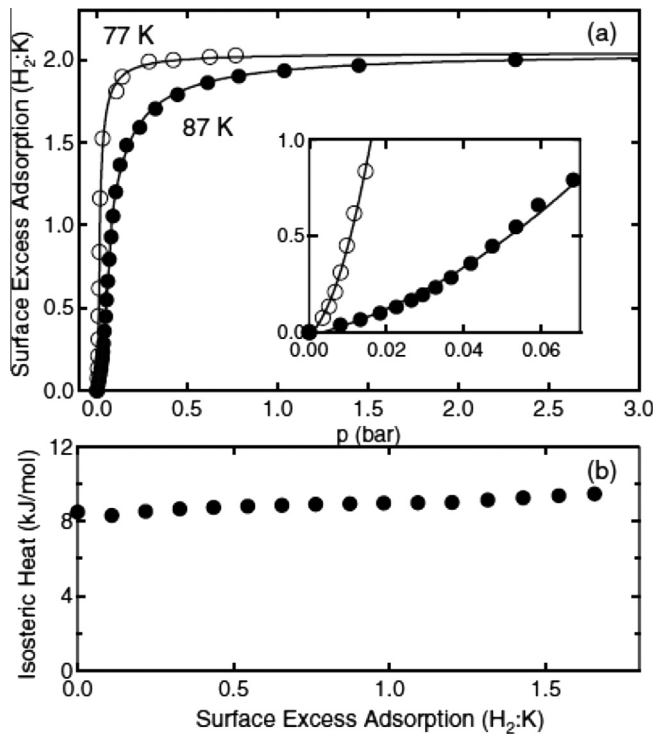
Fig. 16. (a) Volumetric H_2 adsorption isotherms of KC_{24} measured at 77 and 87 K. The *y* axis gives the specific surface excess adsorption as a mole ratio of H_2 to K. The inset enlarges the low pressure region of the isotherm. (b) Isosteric heat of adsorption (kJ/mol) as a function of surface excess adsorption [218].

planes lead to enhanced binding energy for H_2 adsorption (8.4 kJ/mol) in KC_{24} that is about twice to bare graphite.

An enhanced H_2 adsorption is observed in the herringbone graphite nanofibers (GNFs) when expanded the graphite lattice using intercalation of concentrated sulphuric/nitric acid mixture

followed by a thermal shock [220]. The SSA of 47 m^2/g in GNFs is increased to (67 and 555) m^2/g when treated at 973 K and 1273 K, respectively. Thus expanded GNFs show a multifold increase in H_2 adsorption (1.2 wt% and 0.29 wt% at 77 K and 300 K, respectively at 20 bar) compared to unexpanded GNFs. In order to achieve an optimum interlayer distance, Kim et al. obtain the H_2 isotherms in a series of pillared-GO at 77 K and 1 bar [221]. Interlayer distance is controlled using pillaring diaminoalkanes ($NH_2(CH_2)_nNH_2$, n = 2, 6, 10) and subsequent thermal annealing between (300–598) K. The structures show a maximum H_2 uptake for an optimum interlayer distance of 0.63 nm, in good agreement with the first-principles calculations for graphitic materials. In their earlier work [222], the GO itself used to tune the interlayer distance without inserting other pillaring supports. A careful reduction in a controlled thermal annealing not only retains the layered structure and also shows improvement in SSA, up to 192 m^2/g and pore volume, 0.689 cm^3/g, compared to 57 m^2/g and 0.076 cm^3/g for the initial GO. Nuclear magnetic resonance (NMR) measurements confirm a considerable reduction of O– and OH– functional groups in the annealed GO. As high as 4.8 wt% of H_2 adsorption at 77 K and 90 bar is measured in the annealed GO with an interlayer distance of 0.64 nm. A considerable reduction in the H_2 uptake is observed with a little increase in layer spacing over 0.64 nm.

In another approach, the porous networks of graphenes engineered by bridging the graphene layers and metal-oxide particles through surface functional groups. For example, the GO-transition metal-oxide composites; GO/V_2O_5 and GO/TiO_2 are developed through binding of C–OH species of GO and the oxygen on the transition metal-oxide via a dehydration reaction [223]. The hydrothermally designed porous graphene–Mn_3O_4 nanocomposites from the aqueous GO dispersion and $MnO(OH)_2$ colloids yield an enhanced SSA up to 680 m^2/g [224]. The composite shows ~2.5 mmol/g of CO_2 adsorption at ambient pressure and temperature compared to ~1.75 mmol/g in a controlled graphene. The solvothermally synthesised graphene–iron-oxide hybrid structures reveal an enhanced microporosity with SSA ranging between (418 and 901) m^2/g [225]. The nanoporous graphene–polyoxometalate (GPOM) hybrid structures are synthesised from *in-situ* hydrazine hydrate reduction of GO aqueous solution and cross-linker phosphomolybdic acid [226]. POM is a polyatomic ion, usually an anion that consists of three or more transition metal oxyanions linked together by shared oxygen atoms to form a large, closed 3D framework. The polynuclear metal-oxo structured POM is a versatile building block cluster for construction of functional hybrid materials. The hierarchical pore GPOM shows a pore volume of 0.57 cm^3/g and SSA of 680 m^2/g, considerably larger than SSA of 23 m^2/g for GO and 8 m^2/g for POM. A highly increased interlayer spacing of 3.2 nm and 3.6 nm is achieved in GPOM and o-GPOM (oxidation of GPOM by hydrogen peroxide), respectively from 0.4 nm in a reduced GO. H_2 adsorption of 0.8 wt% and 1.3 wt% in GPOM and o-GPOM respectively, is obtained at 77 K and 1 bar. From the results, it is worth noting that the (micro)pore size distribution, adsorption enthalpy, exposed metal-sites and functional groups play a critical role in enhancing H_2 adsorption.

Using a well-known reactivity between boronic acids and hydroxyl groups, Taner's group [107,227] develop a novel pillared GO structures, called GO frameworks (GOFs) by linking the various phenylboronic acids between GO layers (Fig. 17). For the past few years, boronic acids have been considered as versatile building blocks for the construction of a variety of molecular architectures [78,228]. The interaction between boronic acids and diols has been used recently to construct a variety of crystalline porous frameworks, called covalent organic frameworks (COFs) [78]. Thus the rich surface oxy-functional groups on the graphene leads to the development of GOFs by forming strong boronate ester bonds as shown in Fig. 17. The structures are synthesised through a solvothermal method using methanol solution from various concentrations of GO and phenylboronic acid. GOFs show a systematic increase in the interlayer distance from 0.75 nm to 1.05 nm and SSA from 10 m^2/g to 470 m^2/g. About 1 wt% of H_2 uptake at 77 K and 1 bar with relatively high (~9 kJ/mol) heat of H_2 adsorption at low coverage is achieved. The H_2 adsorption capacity for a given SSA and heat of adsorption appears twice as large as typical porous carbons ([82,199,201], typically about 0.5 wt% of H_2 uptake at 77 K and 1 bar for every 500 m^2/g of SSA and heat of adsorption of 4–6 kJ/mol). GOFs also show a good room temperature CO_2 adsorption of ~2.7 mmol/g at 4 bar with again high heat of CO_2 adsorption of 35 kJ/mol. The micropore structure with slit-like pores and strong surface interactions with functional groups are favourable factors enhancing their capacity for gas adsorption and binding. Similarly, cross-linked and functionalized graphene sheets from diazonium (product 1) and tert-butylaniline or 4-chloroaniline (product 2) as reagents in chlorosulphonic acid or oleum are synthesised aiming at improved H_2
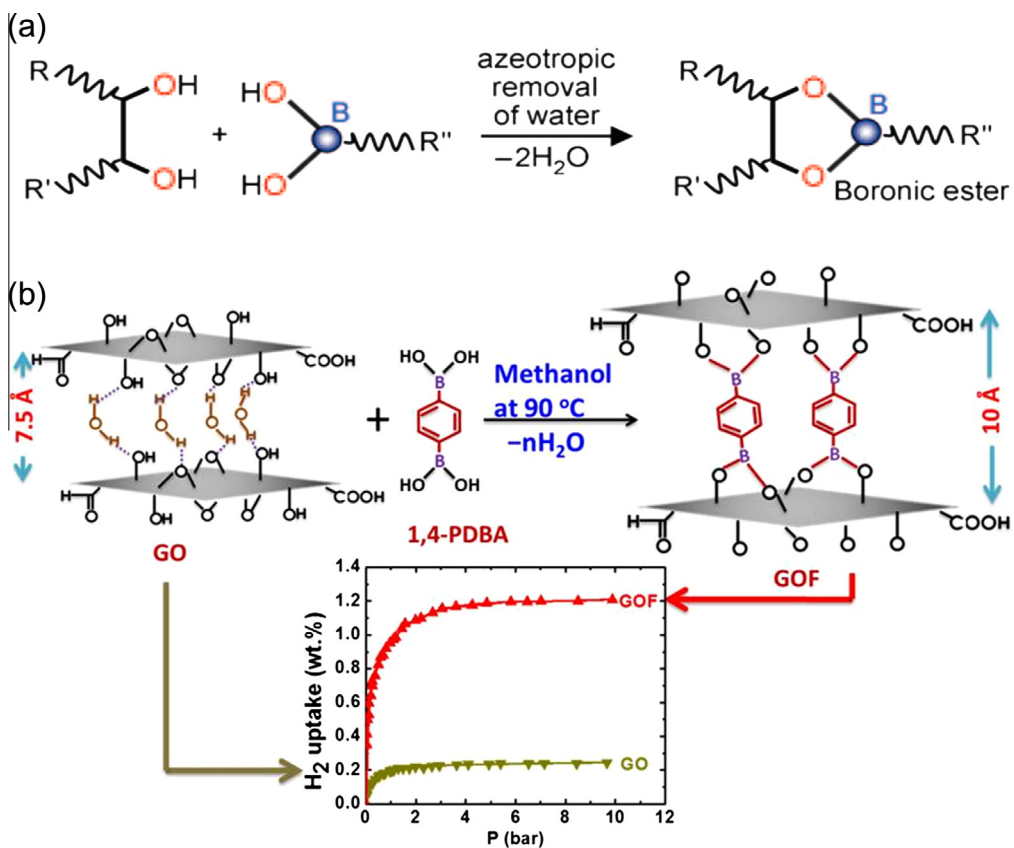
Fig. 17. Representations of (a) boronic ester [107] and (b) GOF formation by benzenediboronic acid pillars in GO, and the H_2 uptake in respective structures [227].

adsorption [229]. Products 1 and 2 show a calculated interlayer spacing of ~0.96 nm and ~0.76 nm and SSA of ~440 m^2/g and 350 m^2/g, respectively. Enhanced H_2 adsorption of up to 1.6 wt% at 77 K and 2 bar is obtained compared to ~1 wt% in the starting exfoliated graphenes. The enhanced H_2 adsorption again suggests importance of tuning the interlayer separation, microporosity, and functionalization. Zhou et al. design a porous graphene structures by cross-linking non-planar terpyridine complexes using azide–alkyne click reaction [230]. The structures show up to 440 m^2/g of SSA and a CO_2 adsorption of 2.6 mmol/g at 273 K and 1 atm.

The hybrid monolith aerogels of chitosan (CTS, an environmentally-benign biopolymer) with GO, prepared using freeze-drying, show dramatic increase in both the porosity (from 153 m^2/g to 415 m^2/g) and cyclic CO_2 uptake (from 1.92 mmol/g to 4.15 mmol/g at 25 °C and 1 bar) for a GO loading of 20 wt% [231]. The DAB poly(propyleneimine) dendrimer (DAB) cross-linked GO-based hybrids display good CO_2 adsorption of ~2 mmol/g (P/P_0 = 0.35) upon wetting [232]. Under humid conditions the sample exhibits ~3 times the adsorption capacity with fast kinetics, compared with the dry state, due to the presence of amino groups of DAB which can form carbamates through zwitterions (primary amines) and bicarbonates (tertiary amines). The formation of these groups is enhanced in the presence of a base (hydroxyl groups of water).

In a work by Matsuo et al., the pillared graphenes are synthesised by pyrolysis of various silsesquioxane bridged GOs [233]. The structures are highly microporous in nature (calculated pore widths of about 0.7 nm) and show an interlayer spacing between 1.34 nm and 1.6 nm and SSA up to 940 m^2/g, which leads to an H_2 excess adsorption of 0.6 wt% at ambient temperature and 200 bar

with a high heat of H_2 adsorption of (8–11) kJ/mol. A further enhanced H_2 adsorption of 1.4 wt% and 2.6 wt% at room temperature and 50 bar is obtained in a liquid crystal (LC) route prepared macroscopically ordered layer-by-layer 3D framework of GO and GO-MWCNTs composites, respectively (Fig. 18) [234]. MWCNTs act as 1D spacer between graphene sheets that result in large increased interlayer spacing up to ~7 nm. The high H_2 adsorption is attributed to the synergistic effect of the well-spaced GO sheets and debundling of MWCNTs to enhance the accessible surface area. It is worth noting that the ~1.4 wt% of H_2 in a LC-GO with its interlayer spacing of around 0.8 nm is also comparatively higher than an earlier reported value of 0.2 wt% at 77 K in GO [107].

The enhanced H_2 uptake capacities are also realised in graphene incorporated clay materials [235,236]. The samples are prepared by impregnation of the natural clay (montmorillonite and sepiolite) substrates by caramel in aqueous media, followed by a thermal treatment in the absence of oxygen, gives rise to graphene-like materials, which remain strongly bound to the silicate support. These carbon–clay nanocomposites shows ~0.4 wt% of H_2 at 298 K and 200 bar related to the carbon mass. These uptakes are still far from the predicted value of (3–4) wt% from model simulations. A very high isosteric heat of H_2 adsorption of 14.5 kJ/mol shows a strong stabilization of the H_2 molecule within the structure. The controlled clays without graphene, thermally treated under the same conditions
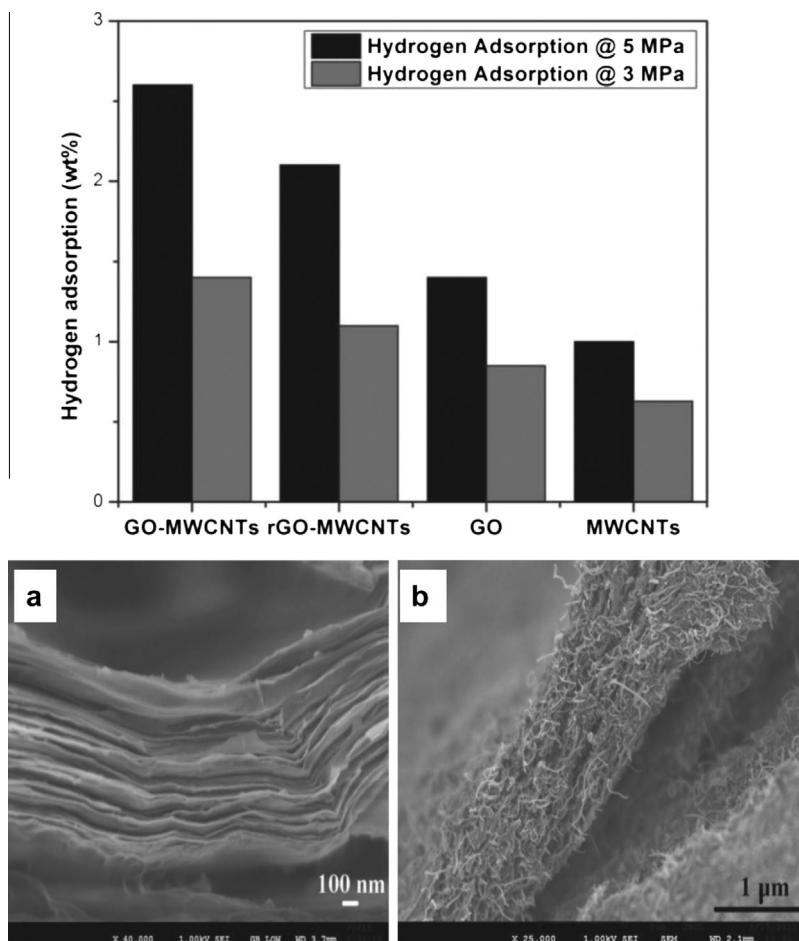

Fig. 18. Top: Comparative H_2 adsorption in GO, MWCNTs, GO-MWCNTs and rGO-MWCNTs at room temperature under different hydrogen pressures. Bottom: SEM micrographs of (a) GO paper, (b) layer-by-layer assembled GO platelets decorated by MWCNTs [234].

did not show any appreciable H_2 adsorption. The samples also show about (0.6 and 1.7) wt% of H_2 uptake related to the total mass of the system and carbon mass, respectively, at 77 K.

In another case the enhanced adsorptive gas storage is achieved by pore engineering of highly porous MOFs with GO [237–240]. The MOFs are a type of crystalline and highly porous solids made up of metal clusters linked with organic ligands. For example, Petit et al. synthesise the MOF-GO composites by solvothermal method, with the addition of GO up to 50% by weight to the MOF precursors [237]. The successful retention of porosity suggesting that the building process of the composites occur via the reaction/binding of the copper dimers from the HKUST-1 (Cu-MOF, also known as Cu-BTC) with/to the functional groups in GO (epoxy, carboxylic, hydroxylic, sulphonic). At the optimal GO content, the composites show about 15% and 18% increase in a micro- and total porosity, and SSA up to 1000 m^2/g compared to a 900 m^2/g in HKSUT-1. While the composites with the higher GO contents show smeared SSA (600–700) m^2/g due to the formation of nonporous reduced graphene stacks from the excess, unreacted GO. H_2 adsorption of (2.0–2.5) wt% at 77 K and 1 bar in these structures is consistent with the enhanced microporosity. Later, Liu et al. report a further enhancement in SSA and H_2 adsorption as well as CO_2, CH_4 and N_2 adsorptive separation in a similar Cu-MOF and GO composites, named as CG (Fig. 19) [238]. The authors also reveal more insights in the growth mechanism of the Cu-
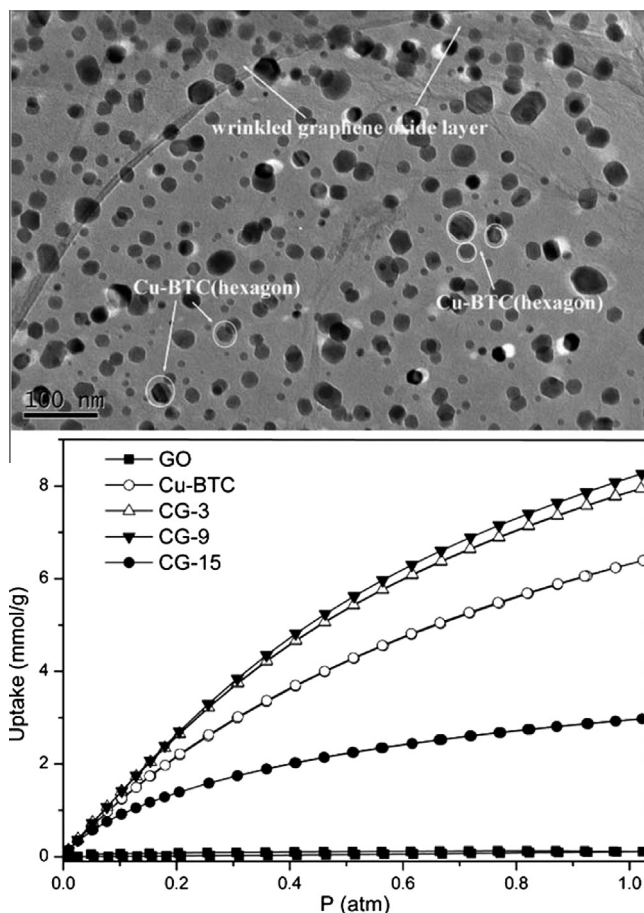

Fig. 19. Top: HRTEM image of the composite CG-9. Bottom: CO_2 adsorption isotherms of Cu-MOF, CG-3, CG-9 and CG-15 at 273 K. The SSA (m^2/g), 1305, 1470, 1532, 500, and total pore volume (cm^3/g), 0.518, 0.610, 0.645, 0.312 for Cu-MOF, CG-3, CG-9, and CG-15, respectively. In CG-*n*, *n* is a weight percent of GO added to the MOF precursors before synthesis [238].

MOF crystals on GO substrate in the composite through DFT calculations (in a VASP). The results show strong interaction energy of Cu to the GO defect of 15.12 eV, more favourable than those on the –OH (3.92 eV) and –O– groups (1.60 eV) of the GO surface. Furthermore, the epoxy groups and the defects of the GO layers act as seed and termination sites, respectively for formation of nanosized and well-dispersed Cu-BTC on the layers of GO (Fig. 19). Thus the composites show about a 30% increase in CO_2 and H_2 adsorption (from 6.39 mmol/g of Cu-BTC to 8.26 mmol/g of CG-9 at 273 K and 1 bar for CO_2; from 2.81 wt% of Cu-BTC to 3.58 wt% of CG-9 at 77 K and 42 bar for H_2). A similar CO_2 adsorption is observed in a GO-Cu-BTC with stronger interaction energies (activation energies of (68.6 and 56.7) kJ/mol for CO_2 on the composite and Cu-BTC, respectively) and enhanced CO_2/CH_4 adsorption selectivity, twice that of Cu-BTC for an equimolar CO_2 and CH_4 mixture [239]. Furthermore, the composites of Cu-BTC and GO modified by urea show enhanced CO_2 adsorption of 4.23 mmol/g [240]. The incorporation of aminated GO into a MOF structure shows synergistic effect; the porosity modification with new micro-pores at the interface and basic groups on the surface, which are expected to increase the physical adsorption forces and acid–base interactions, respectively. This would not only increase the adsorption capacity but also the selectivity.

Sandwich-like graphene-silica sheets with incorporation of polyethyleneimine (PEI/G-silica, with about 12 wt% graphene and 60 wt% PEI, amine based solids for CO_2 adsorption) show a high CO_2 adsorption of 4.3 mmol/g at 348 K under 7.4 bar with good cyclic stability [241]. The G-silica sheets obtained through the hydrolysis of tetraethylorthosilicate on the surface of GO with the aid of a cationic surfactant (cetyltrimethyl ammonium bromide) followed by pyrolysation at 973 K under Ar. PEI impregnation is made via a solution route using methanol solvent. PEI/G-silica sheets show a pore size of (0.7–2.0) nm with a SSA of 32 m^2/g, much smaller than that of G-silica sheets ($\sim$2.0 nm and 930 m^2/g). Clear advantage of graphene sheets is observed in an enhanced CO_2 adsorption at low equilibrium pressures (<1 bar), whereas the PEI/G-silica sheets show a significantly higher CO_2 adsorption than PEI/silica sheets. Sui et al. synthesise 3D cross-linked GO hydrogels with a polyethylenimine (PEI) [242]. As shown in Fig. 20, the structures are developed through gel formation from aqueous GO dispersion with PEI solution at 25 °C followed by freeze-drying. The monoliths possess a low density in the range of (0.02–0.03) g/cm^3 due to the open-pore structures interpenetrating the skeleton of GO sheets. This is also well observed in the XRD patterns. Compared with GO, an increase in the interlayer spacing up to 1.56 nm, indicating successful cross-linking of the GO sheets. Therefore, the open-structures show enhanced SSA of up to 476 m^2/g and CO_2 adsorption of $\sim$2.4 mmol/g at 273 K and 1 bar compared to 1.8 mmol/g in a controlled GO with a high SSA (876 m^2/g). Clearly, the functional basic sites enhance the CO_2 adsorption capacity.

4.3. Spillover and dissociative atomic hydrogen sorption

As explained in Section 3.1.5, hydrogen spillover is a dissociation of H_2 on the catalytic metal nanoparticles, followed by subsequent atomic adsorption onto the substrate surface sites. It is considered as one of the effective ways to enhance H_2 storage capacity in the carbonaceous structures [80,243]. In the study by Hu et al., the H_2 uptake by low temperature physisorption and room temperature chemisorption is clearly demonstrated in a high Pd (about 24 wt%) dispersed graphene nanocomposite [244]. The chemisorptive H_2 uptake in Pd nanoparticles shows a two-phase behaviour of isotherms. Initially formed solid solution region at low pressures (α-phase), is transformed to a hydride phase (β-phase) at higher pressure through a coexistence of two-phase region ($\alpha + \beta$), plateau range, very similar to the typical pressure–concentration–temperature curves of H_2 storage materials [245,246]. The isotherms also show a Pd particle size, (4–24) nm, dependence; a clear transition from α- to β-phase is observed with increase in a Pd particle size. A high H_2 uptake of 3.2 wt% at 77 K and 1.1 bar for a given SSA of 230 m^2/g and a pore volume of 0.3 cm^3/g suggest a clear spillover effect. Furthermore, an exfoliated graphene (with a SSA of 755 m^2/g) decorated by Pd and Pt nanoparticles, (2–5) nm, via an electroless deposition technique also shows enhanced room temperature spillover of H_2 uptake [247]. The observed uptake of 4.3 H/Pd is much larger than that of actual chemisorbed hydrogen in the bulk Pd with a stoichiometry of 0.6 H/Pd. The room temperature H_2 spillover capacity in a mixture of the activated carbon (AC, Maxsorb) as "secondary spillover receptor" and Pd-exfoliated graphene (in a 9:1 weight ratio) shows reversible H_2 uptake of 0.82 wt%, 49% more (0.55 wt% of H_2)
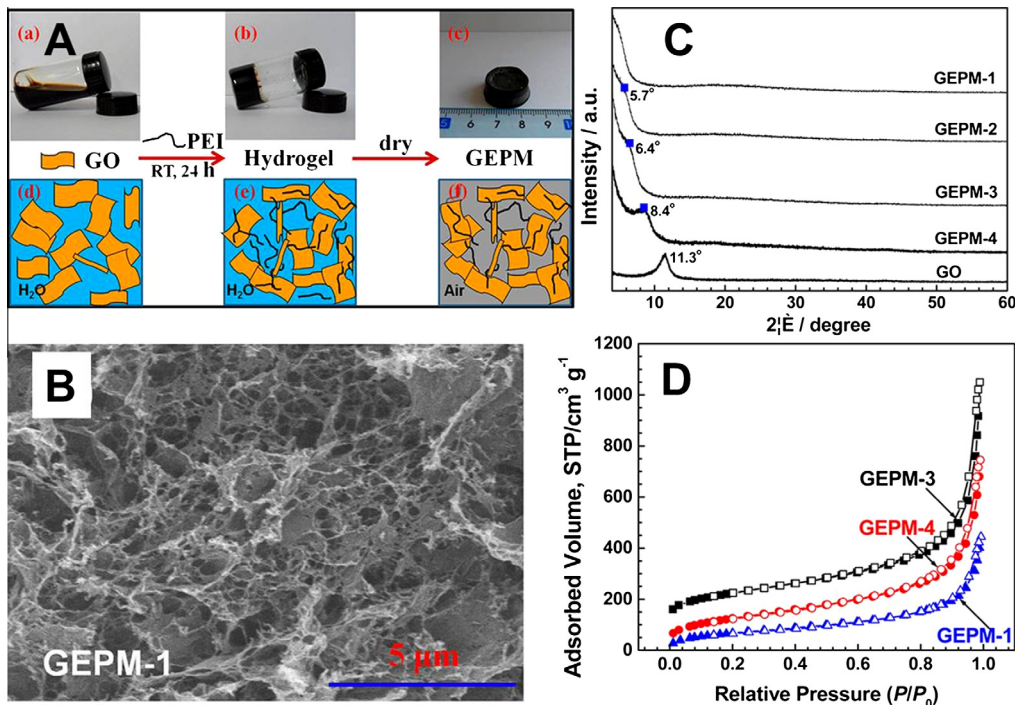
Fig. 20. (A) Illustration of the preparation process of the GO-PEI porous materials (GEPMs): digital pictures of aqueous GO dispersion (a), GO-PEI hydrogel (b), and GEPM (c) and schematic diagram of aqueous GO dispersion (d), GO-PEI hydrogel (e), and GEPM (f). (B) SEM image of the GEPM. (C) Wide-angle X-ray diffraction patterns of the GEPMs (solid square for shoulder peak position). (D) 77 K N_2 sorption isotherms of GEPM-1, GEPM-3, and GEPM-4 (solid symbols for adsorption and empty symbols for desorption). The isotherm of GEPM-3 is offset by 100 units. GEPM-1, GEPM-2, GEPM-3, GEPM-4, and GEPM-5 are for the different PEI to GO weight ratios, 3:1, 2:1, 1:1, 1:3, and 1:6, respectively [242].

than Pd-free AC-exfoliated graphene under 80 bar [248]. The spillover is also revealed by a high isosteric heat of H_2 adsorption of $\sim$14 kJ/mol, compared to $\sim$8 kJ/mol for AC.

Ramaprabhu's group report up to 3 wt% and 4 wt% of H_2 in a Pd (20 wt%) nanoparticle decorated graphenes before and after N-doping (ca. 7%), respectively at 298 K and 40 bar (Fig. 21) [249–252]. The values are comparatively higher than $\sim$0.7 wt% and $\sim$1.5 wt% in a Pd free graphenes before and after N-doping, respectively. A clear influence of N-doping can be observed. A combined physisorption and chemisorption process gives a high heat of H_2 adsorption over 12.5 kJ/mol. The hydrogen exfoliated GO at 523 K is used to synthesise N-doping and Pd-decoration through nitrogen plasma treatment and reduction of $PdCl_2$, respectively. The Pd/N-G sample accounts 48% of the spillover capacity enhancement in the total H_2 storage capacity. Wang et al. develop a nonprecious and air stable Ni–B nanoalloy dispersed graphenes to enhance the H_2 adsorption [253,254]. As much as 4.4 wt% of H_2 is achieved at 77 K and 1 bar in the graphene with Ni (0.83 wt%) and B (1.09 wt%) (graphene–$Ni_{0.83}B_{1.09}$) compared to 1.35 wt% of H_2 in the undoped graphene. The composites are obtained via $NaBH_4$ chemical reduction of aqueous solutions of GO and $Ni(CH_3OOH)_2$. The H_2 capacity seems excellent among above Pd–graphene and all other carbon-based materials. Up to 12 kJ/mol of isosteric heat of H_2 adsorption is reported.

Further higher H_2 storage capacity of over 5 wt% at 298 K and 20 bar and heat of adsorption, >30 kJ/mol at low coverage and $\sim$14 kJ/mol at high surface coverage is reported in the Pd/Hg nanoalloy and Pd nanoparticle loaded GO-like foams (GLFs) [255–257]. Porous GLFs (nominal composition C_2OH) are synthesised by simple calcination of the molecular precursor, sodium chloranilate dihydrate in air at 573 K [255]. GLFs consist of interconnected bundles of turbostratically stacked few-layer graphenes
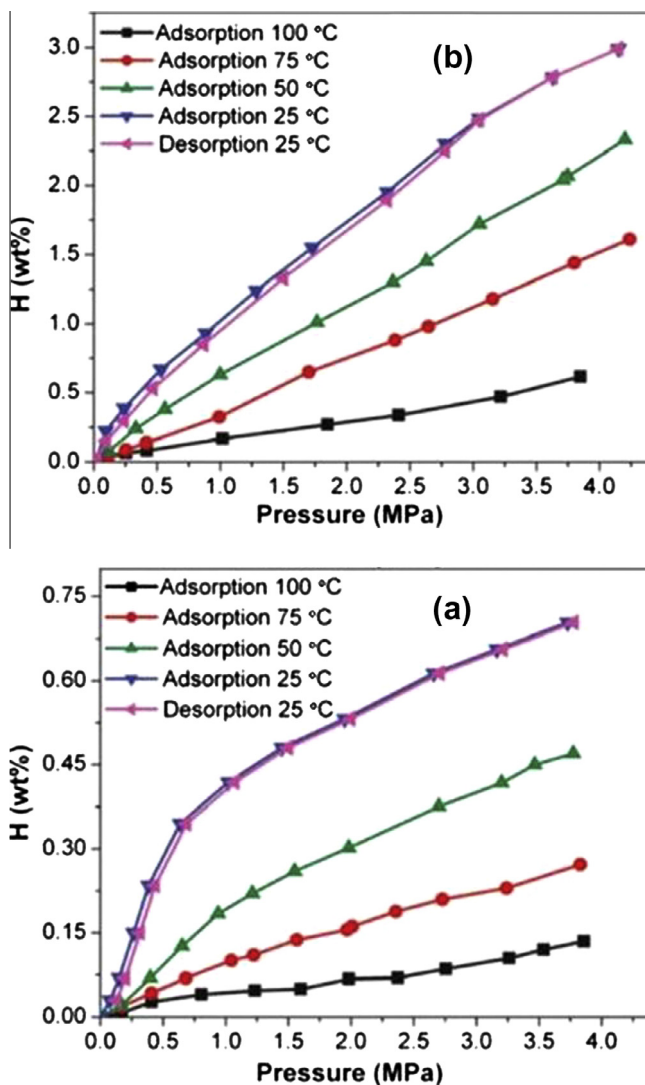
Fig. 21. H_2 adsorption–desorption isotherms of (a) HEG and (b) Pd/f-HEG [249].

build-up of aromatic and aliphatic domains with oxygen rich functional groups on the surfaces. GLFs with SSA of 510 m^2/g and pore volume of 0.89 cm^3/g selectively absorb CO_2 (about 2 mmol/g) over N_2 (0.4 mmol/g), CH_4 (0.7 mmol/g), H_2 (negligible) and CO (0.7 mmol/g) at 10 bar and room temperature. The Pd_4Hg particle loaded (12 wt%) GLFs (Fig. 22) with its inherent carbon-based radicals near the edge and defect sites yield an enormously enhanced H_2 uptake of about 5 wt% at room temperature and 20 bar compared to a negligible H_2 uptake in undoped GLFs [256]. The Pd–Hg alloy loading is obtained through $NaBH_4$ reduction of aqueous GLFs, $PdCl_2$ and $HgCl_2$ mixture. In other study, Wang et al. show an important comparison of H_2 uptake by spillover in Pd loaded (10 wt%) GLFs (Pd/GLFs) and super-activated carbon (Pd/AX-21), and oxygen modified AX-21 (Pd/AX-21-O) [257]. By comparing H_2 absorption, the authors conclude that the existence of abundant oxygen functional groups on the surface and edges in Pd/GLFs lead to enhanced H_2 uptake with a high heat of adsorption, >30 kJ/mol at low coverage and ~14 kJ/mol at high surface coverage compared to those of Pd/AX-21 and Pd/
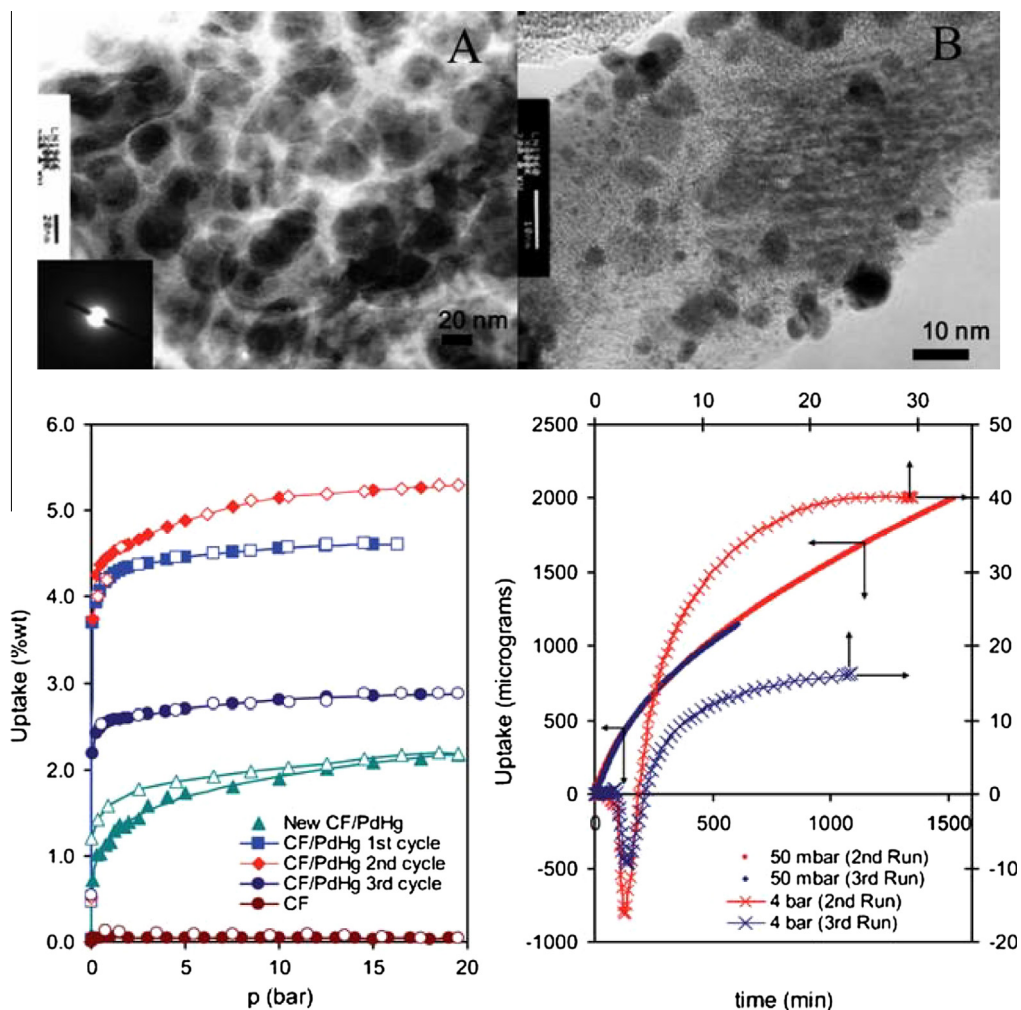
Fig. 22. Top: (a) HRTEM image and ED pattern (inset) of GLF. The image is inverted for clarity (carbon matrix is white). (b) HRTEM of GLF/Pd$_4$Hg. Bottom left: H$_2$ sorption–desorption isotherm (at 298 K) of the GLF, original GLF–Pd$_4$Hg (3 cycles) and a 2nd GLF–Pd/Hg sample (prepared from trihydrate). Bottom right: kinetic uptake examples for equilibration pressures of 50 mbar and 4 bar (data from 2nd and 3rd cycle-original GLF–Pd$_4$Hg) [256].

AX-21-O. The H$_2$ dissociative adsorption is also observed in simple modified graphenic structures without metal dispersions. The volumetric H$_2$ storage of 5 wt% is also reported in exfoliated turbost-ratic carbon nanofibers (CNFs) at 77 K and 100 bar compared to 1.5 wt% in the as-produced CNFs [258]. This enhancement is attributed to the simultaneous molecular and dissociative H$_2$ adsorption in combination with more defective surface, increased SSA (from 103 m^2/g to 227 m^2/g) and pore vol-ume (0.39–0.52 cm^3/g). A graphite exfoliation technique using intercalation of acids and thermal shock is employed to expand the CNFs.

4.4. Bottom-up solution-phase synthesised graphenes

Using the bottom-up solution-phase method, graphenes of gram scales are produced from simple laboratory reagents of sodium and ethanol in a 1:1 M ratio by solvothermal method [259,260]. The

subsequent rapid pyrolysation leads to a porous graphene in relatively large quantities (∼0.1 g for 1 ml ethanol). The sample with a high SSA of 2139 m^2/g shows a high-pressure H_2 uptake of 0.9 wt% at room temperature with a high heat of adsorption of 12 kJ/mol [261]. The adsorption is attributed to dissociation of H_2 at the zigzag edges of the graphene, or combined effects of residual oxygen and sodium functionalities. In other study, the heteroatom (boron, phosphorous, or nitrogen) substituted carbon scaffolds (micrometer sized flake-like few-layered graphene structure assembled by (3–5) nm sized domains) show H_2 capacities of (2.2–2.4) wt% per SSA of 1000 m^2/g at 77 K and 2 bar relative to 1.8 wt% for the pristine carbon scaffold or ∼2 wt% for common carbonaceous materials [262]. The heteroatom substituted scaffolds also show H_2 binding energies between (5–9) kJ/mol.

4.5. Highly porous graphene carbons from templating, CVD and KOH chemical activation

As demonstrated above, all the methods; functionalization, exfoliation and pillaring hybrid designs generated a promising gas sorption and storage. However the structures have limited accessible surface areas and pore volumes. To obtain a relatively higher SSA with tuneable pore structure, self- or sacrificial-templating from the ordered structures, CVD and chemical activation methods are employed [263–267]. As shown in Fig. 23, the chemical activation of precursor GO with activator KOH yields a very high SSA of up to 3100 m^2/g graphene-carbons. The exfoliated GO by thermal shock or microwave irradiation is thoroughly mixed with various amounts of KOH either by solution or dry milling followed by activation at temperatures between 873 K and 1173 K. For example, Srinivas et al. report a range of SSA (up to 1900 m^2/g), pore volume (up to 1.65 cm^3/g), pore size and size distribution in GODCs (GO derived carbons) by changing the GO/KOH concentration and activation temperature [263]. The large fraction of smaller pores is transformed to large pores when increasing KOH concentration and/or activation temperature. As shown in Fig. 24, the GODCs show favourable gas adsorption for CO_2 and CH_4, compared with other high surface area carbons for a given SSA.
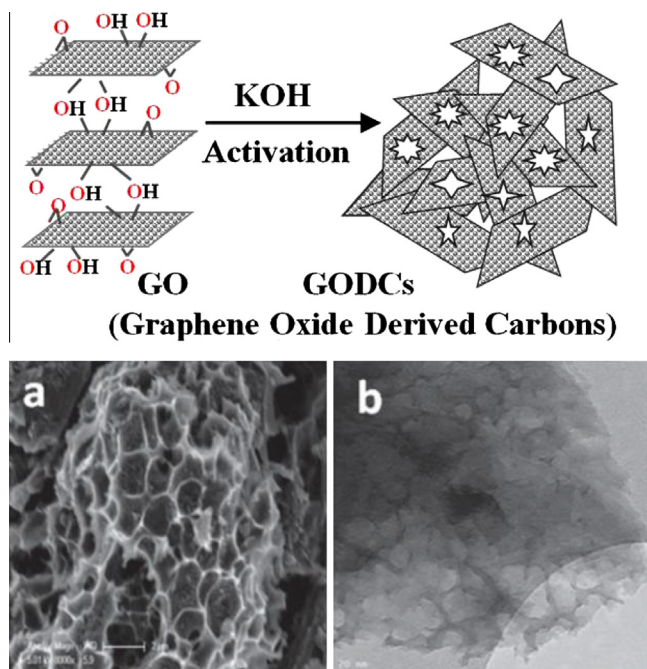

Fig. 23. Top: Schematic showing the chemical activation of GO with KOH that creates pores [263]. Bottom: Surface morphology of nitrogen doped KOH activated GO: (a) SEM image, and (b) TEM image [264].
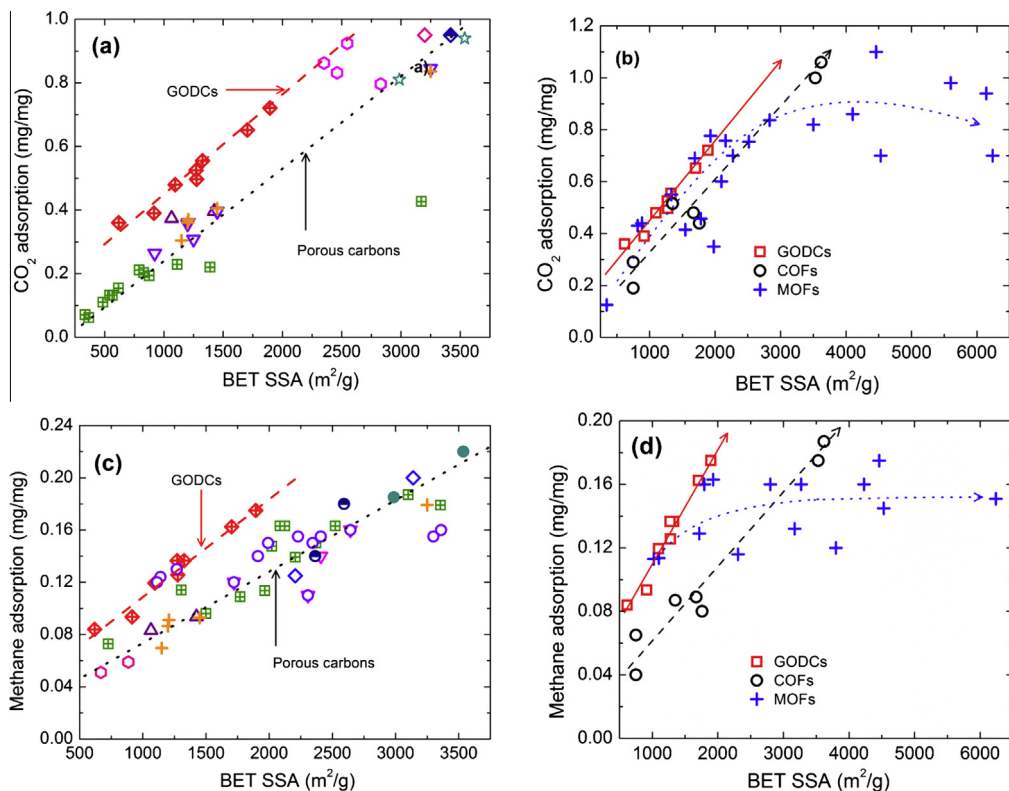
Fig. 24. The 300 K and high pressure CO_2 at 20 bar (a and b) and CH_4 at 35 bar (c and d) adsorption capacities of GODCs with respect to the BET surface area. (a and c) A comparative CO_2 and CH_4 adsorption capacities at 20 and 35 bar, respectively from a range of other porous carbons at around room temperature (298–300 K). (b and d) A comparative CO_2 and CH_4 adsorption capacities at 20 and 35 bar, respectively from a range of other porous organic frameworks; MOFs and COFs [263].

Furthermore, the N-and S-doping in GODCs with pyrrole and poly-thiophene, respectively show an enhancement in ambient CO_2 uptake ($\sim$4 mmol/g) and the selectivity over CH_4 and N_2 [264–266], The selectivity is an important factor for the application in flue gas capture. For example, as shown in Fig. 25, the S-doped graphene carbons show highly enhanced and stable recycling CO_2 adsorption capacity of >4.0 mmol/g over CH_4, N_2 and H_2 (which show much lower adsorption of <1 mmol/g) at 298 K and 1 bar. The capacity is twice as high as for the undoped activated graphene carbons ($\sim$2 mmol/g) [263]. The CO_2 capture capacity in the doped porous graphene seems comparable with or even higher than the various other porous media; N-doped porous carbons, amine functionalized silica and MOFs. The high microporosity and N-functionality show a high isosteric heat of CO_2 adsorption between (30 and 56) kJ/mol. The CO_2 adsorption of 1.82 mmol/g at 0.2 bar (is a partial pressure of CO_2 in the flue gas stream) in the S-doped sample is also comparatively larger than other porous carbons. The increase in activation temperature yields enhanced microporous samples but same time the N- and S-doping content reduces; reduction from (7 to 2.7) at% is observed at 700 °C, whereas the lower activation temperatures lead to a decrease in SSA. Using porous, layer structure MgO as a template, nanomesh of one- to two-layer graphene in a gram-scale is produced by CVD method using methane as a carbon precursor [267]. After acid treatment to remove MgO template, the graphene sheets show a large corrugations with nanopores of $\sim$1 nm, total pore volume of 2.35 cm^3/g and SSA of 2038 m^2/g. A high H_2, CH_4 and CO_2 adsorption of $\sim$1.5 wt%, 14.5 mmol/g (at 90 bar) and 36.5 mmol/g (at 31 bar), respectively at 274 K is reported.
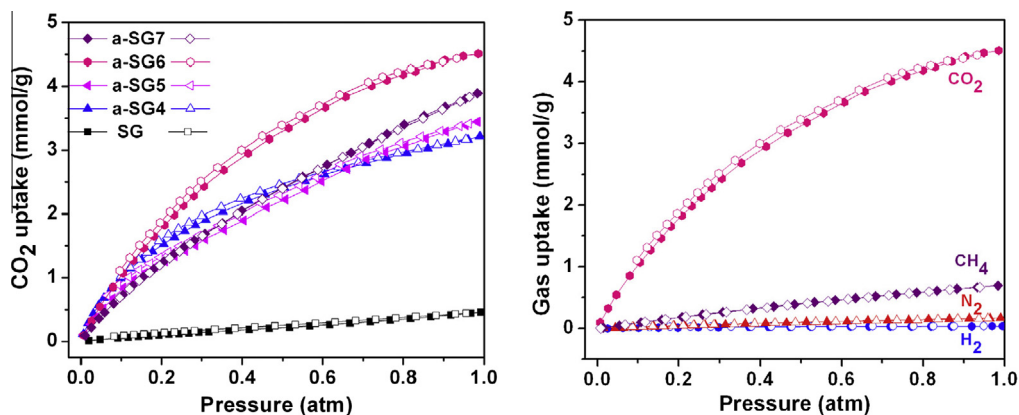
Fig. 25. Left: CO_2 adsorption isotherms for SG and a-SG samples at 298 K (filled symbols: adsorption, open symbols: desorption). Right: H_2, N_2, CH_4 and CO_2 adsorption–desorption isotherms of a-SG6 at 298 K [266].

4.6. Electrochemical hydrogen storage

The graphene materials with their high electrical conductivity and chemical stability also investigated for electrochemical H_2 storage via electro-decomposition of water on a cathodically polarised electrode. The adsorption–desorption mechanism during charge/discharge phenomenon is simply written in terms of the following equations: $[G] + nH_2O + ne^- \leftrightarrow [CH_n] + nOH^-$, where $[G]$ represents the graphene host. In steps; water reduces first ($H_2O + e^- \rightarrow H^+ + OH^-$) and the nascent hydrogen then adsorbs into the graphene network due to the electric polarisation of the electrode under the external applied potential. In the reversible process, the hydrogen atoms discharge from the graphene and recombine with OH^- to make H_2O. A reversible H_2 storage of $\sim$148 mA h/g is reported in a few layer graphene flakes that are synthesised through arc-discharging of pure graphite under hydrogen atmosphere [268]. The graphene working electrodes are prepared on Ni-foam using PVDF binder and press. The reversible H_2 storage seems highly dependent on the structural properties of graphene flakes; crystallite size, wrinkles, defects, and inter layer spacing. Graphene-porous cobalt-oxide (Co_3O_4) nanocomposites show a first discharge capacity of 241.9 mA h/g which is equal to 0.89 wt% of H_2 [269]. The nanocomposite on a sheet of nickel foam, $Ni(OH)_2$/NiOOH and Hg/HgO as a working, counter and reference electrode, respectively is employed in a 6 M KOH electrolyte at 298 K. As shown in Fig. 26 a further high discharge capacity of 1415 mA h/g, equivalent to 5.176 wt% of H_2 is observed in the fullerene-like orthorhombic-structured Co_3C nanoparticles, synthesised by ball-milling of Co and graphene powders [270]. Two obvious plateaus at 1.2 V and 0.4 V, respectively in the discharge curve of Co_3C nanoparticles reveal an existence of two different H_2 adsorption sites; first adsorbs into the interstitial sites/pores between Co_3C nanoparticles and then diffuses into the interstitial sites between Co_3C. The composition and ball-milling conditions show a profound effect on the cyclic stability of the composites. The continuous decay in a cyclic discharge capacity is attributed to the formation of β-Co(OH)$_2$. Overall, the Co_3C nanoparticles display a relatively high discharge capacity when compared with the traditional AB_5 type H_2 storage materials.

4.7. Chemical hydrogen storage

The hydrogenated graphene, also called as graphane, a covalently bonded hydrogen atoms to carbon atoms, (sp^3 C–H bonds on basal plane) is essentially different from the physical H_2 absorbed graphene structures. Number of synthesis methods; plasma, CVD, liquid and gas phase reactions are developed to obtain graphanes. Subrahmanyam et al. demonstrate that it can be used as a chemical H_2 storage material [271]. Birch reduction of a few-layer graphene with excess Li in liquid ammonia produce the hydrogenated graphene that contains up to 5 wt% of H_2 (Fig. 27). Spectroscopic studies
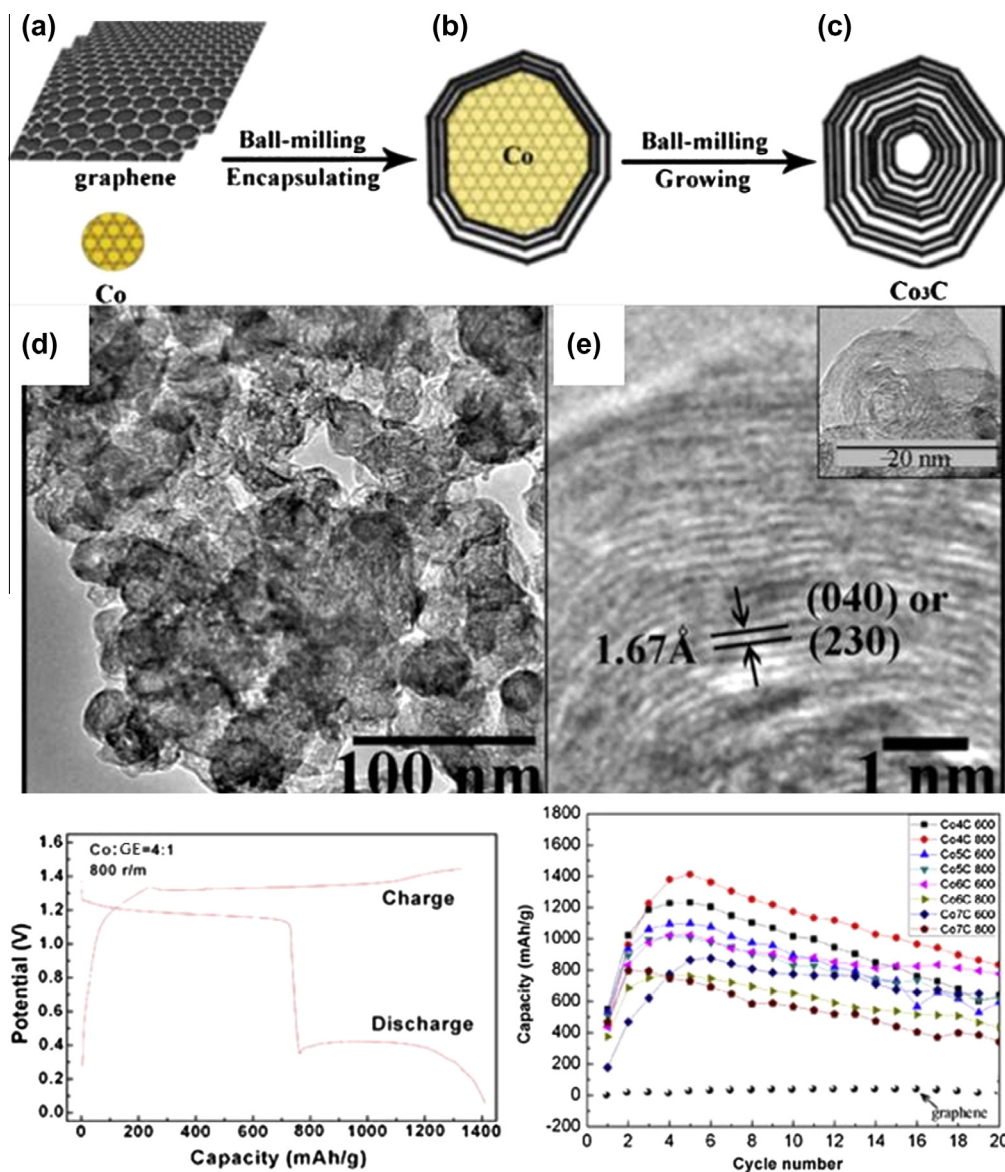
Fig. 26. Growth mechanism and hydrogenation behaviour of the fullerene-like Co$_3$C (weight ratios$_{Co:GE}$ = 4:1, 800 rpm): (a) starting nanoparticle of graphene and metal Co, (b) partly reacted Co$_3$C, encapsulated with layers of the graphene, (c) the final quasi-spherical closed-cage nanoparticle of Co$_3$C, (d and e) HRTEM images of the Co$_3$C and (f) charge–discharge curves. (g) Capacities and cycle stability of the as-obtained G and Co$_3$C electrodes (the composition Co$_x$C, represents the weight ratios of Co:G = x:1; x = 4–7) at a 30 mA/g discharge current density [270].

reveal the presence of sp^3 C–H bonds and the hydrogen can be released up on heating or irradiation with UV or laser. Indeed, the hydrogenation of various carbon structures, fullerenes, nanotubes, and graphites via a dissolved metal reduction method with Li and methanol in liquid ammonia has been demonstrated early in 2001 [272]. These structures release about (4–5.4) wt% of H$_2$ upon heating to 873 K. A simultaneous release of H$_2$ and a small amount of methane is observed during the decompo-

Fig. 27. Change in the weight percentage of hydrogen of EGH and HGH with temperature. (Inset) The evolution of H_2 is recorded by a gas chromatograph [271].

sition. Recently, a hydrogenated graphene with $\sim$6 wt% of H_2 ($C_{1.3}H)_n$, is synthesised directly from a Birch reduction of graphite powder [273].

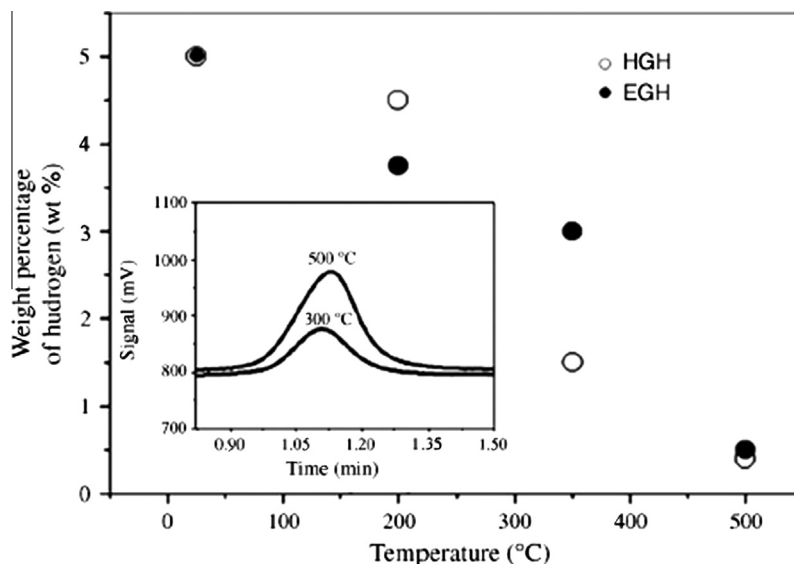Simplified techniques have also been developed to obtain chemical hydrogenated graphenes in a large scale compared to complexity involved in a hydrogenation of CVD/mechanically cleaved graphene in hydrogen plasma [274] or Birch reduction of graphene/graphite. For example, a gram scale of hydrogenated graphene directly from the GO is synthesised via in-situ generated atomic hydrogen through the H_2 spillover using nickel as an active catalyst under ambient conditions [275]. The hydrogenated graphenes also produced directly by exfoliating GO under high pressures, (60–150) bar of hydrogen at high temperatures, (473–773) K [276]. The hydrogen, fluorine, and oxygen gas phase atomic covalent functionalization to graphene is also explained [277].

Earlier, Orimo and his co-works report a hydrogen concentration up to 7.4 wt% ($CH_{0.95}$) in the ball-milled graphitic nanostructures (Fig. 28) [278–280]. Hydrogenation is attributed to the formation of dangling carbon bonds, the CH_x covalent bonds. Interestingly the milled graphite also shows $\sim$400 m^2/g of SSA and H_2 physisorption at cryogenic temperature because of random orientation of fragmented small coherent domains that consist of small stacks of 2–3 graphene layers. Very recently, a large scale (5 g for each batch), edge-hydrogenated graphene with 3 wt% of H_2 (which corresponds to C/H = 2.3) is produced by ball-milling of graphite powder in a hydrogen atmosphere [281]. Electron microscopy studies reveal the mechanochemical cracking of graphite into small grain sizes of (0.1–1) μm after milling of 48 h correspondingly, the SSA and pore volume increases respectively, (3–437) m^2/g and (0.002–0.391) cm^3/g. The edge-selective hydrogenation during the ball-milling process is expected due to the reaction between reactive carbon species (radicals and ions) at the broken edges of graphenes.

4.8. Graphene membranes and protection barriers

A monolayer graphene membrane is impermeable to standard gases including helium [282]. The nanopore graphene membrane as molecular sieves is demonstrated by measuring the transport of a range of gases (H_2, CO_2, Ar, N_2, CH_4 and SF_6) through the irradiated pores [283]. As shown in Fig. 29, a membrane fixed over predefined 5 mm diameter wells on SiO_2 and pressurised with H_2
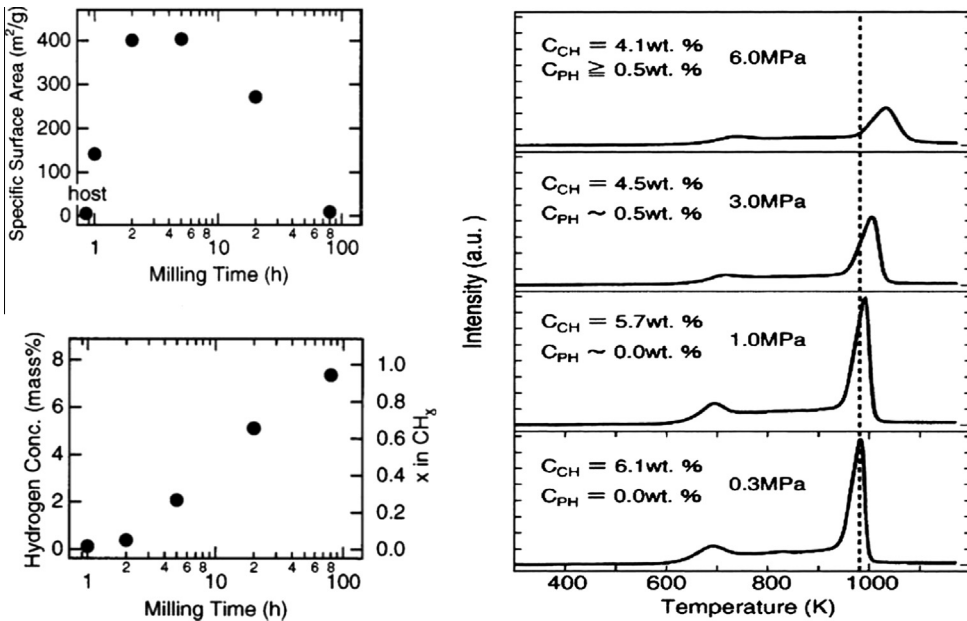
Fig. 28. Left-top: Surface area of the nanostructured graphite, as a function of milling time under initial H_2 pressure of 10 bar (1 MPa) at room temperature. Left-bottom: Total hydrogen concentration in the nanostructured graphite, as a function of milling time under initial hydrogen pressure of 10 bar at room temperature [280]. Right: Thermal desorption spectroscopic plots of H_2 for the nanostructured graphite prepared by milling for 80 h under various hydrogen pressures. Here, chemisorption hydrogen concentration (C_{CH}) determined by oxygen combustion method and physisorption-like hydrogen concentration (C_{PH}) at 60 bar (6 MPa) and 298 K determined by a volumetric method are listed as well [278].

gas is etched with ultraviolet light leads to a rapid leakage of H_2 but preventing N_2 from passing through it. A size selective permeation of gas molecules is demonstrated by creating different-size pores. The submicrometer thick, (0.1–10) μm and area $\sim$1 cm^2 of GO membranes are found to be completely impermeable to liquids, vapours and gases, including helium, while allowing unimpeded permeation of water (H_2O permeated through the membranes at least 10^{10} times faster than He) [284]. It is attributed to a low-friction flow of a monolayer of water through 2D capillaries formed by closely spaced graphene sheets. Diffusion of other molecules is blocked due to reversible narrowing of the capillaries in a low humidity and/or by their clogging with water. Mass-spectrometry measurements show that helium is less permeable in dry GO film than a 1-mm-thick glass. No permeation is detected for several polar and nonpolar organic liquids through GO membranes of 1 μm in thickness. Reduced GO membranes with an interlayer spacing of 0.4 nm are much less permeable to water. In recent studies, the graphene membranes are also tested for different solvent filtration (desalination) and separation [285,286].

The single layer graphene grown by a CVD method on Ru, Cu and Cu/Ni is found to protect the underneath metal from air oxidation even after heating them in air [287–291]. The surface oxidation of bare copper and oxidation resistance with surface grown graphene is clearly demonstrated in Fig. 30 by controlled CVD growth of graphene directly on Cu foils with partial to full surface coverage [289]. The colour change of bare copper foil indicates a surface oxidation, whereas the fully covered graphene surface shows no sign of oxidation. In other case, the oxidation resistance of Fe and Cu foils are also demonstrated by coating them with reduced GO layers [290]. Nilsson et al. investigate the limitations of graphene as an effective corrosion-inhibiting coating on Pt(100) surface for O_2 and CO using scanning tunnelling microscopy measurements and DFT calculations [291]. Graphene layer is found to protect Pt(100) surface against O_2 and CO exposure up to a certain pressures of 10^{-4} mbar
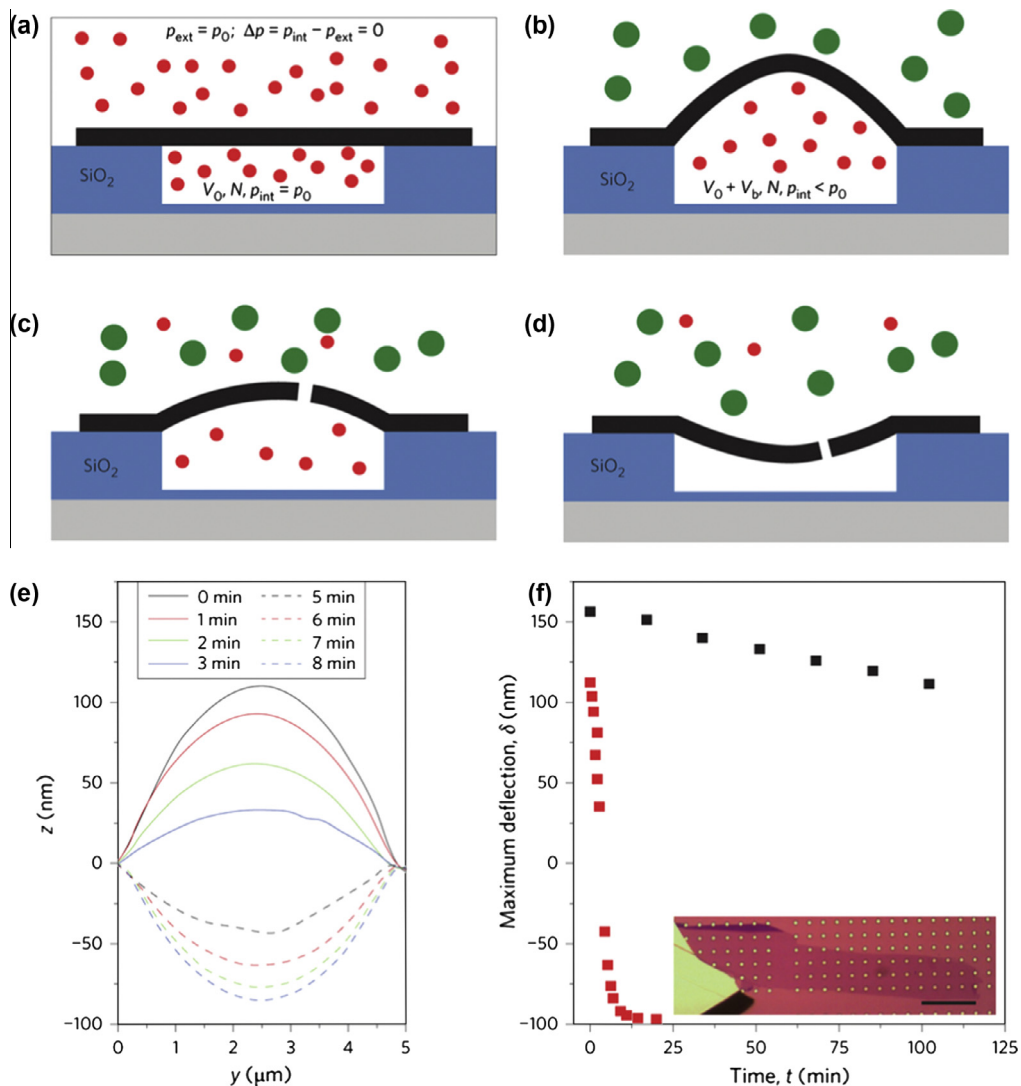
Fig. 29. (a) Schematic of a microscopic graphene membrane on a SiO$_2$ substrate. The microchamber filled with 2 bar (200 kPa) of H$_2$ (represented as red circles). Equilibrium was reached ($p_{int} = p_{ext}$) by diffusion through the SiO$_2$. (b) After $p_{int} > p_{ext}$ the membrane bulged upwards. Etching pore(s) in the graphene membrane bigger than H$_2$ but smaller than the air molecules (mostly N$_2$ and O$_2$, denoted as green circles) (c) leaks out the H$_2$ from microchamber, and (d) all the H$_2$ molecules have leaked out of the microchamber, the membrane deflected downwards. (e) Deflection versus position, measured from 0 min (black) to 8 min (dashed blue) after etching. (f) Maximum deflection δ versus t for one membrane separating H$_2$ from air, measured by AFM. Black symbols represent the H$_2$ leak rate before etching and red symbols the H$_2$ leak rate after introducing selective pores into the graphene. Inset: optical image of the bilayer graphene flake used in this study, which covers many cavities in the SiO$_2$ substrate (scale bar is 60 mm) [283].

and 10^{-6} mbar, respectively. At higher pressures, CO is observed to intercalate under the graphene coating layer.

Designing the polymer thin films or membranes to prevent gas or water molecules from permeating through is a major challenge in many applications for food and electronics. The graphene–polymer composites have been investigated as improved gas barriers due to the large aspect ratio of graphenes

Fig. 30. Photographs of bare Cu foil, partially and fully grown graphene on Cu-foils during oxidation at 443 K [289].

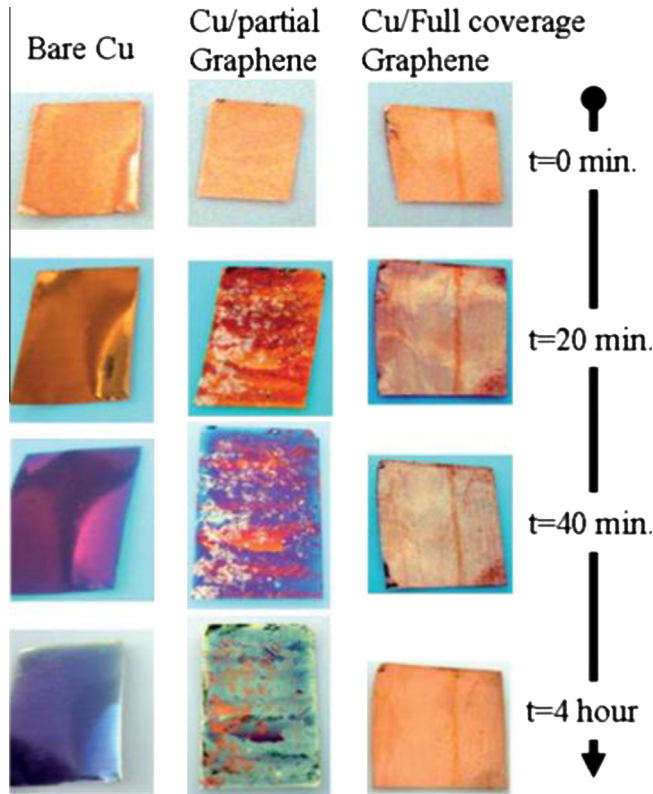[292–296]. For example, a poly(ethylene-2,6-naphthalate)-graphene nanocomposite film with the addition of just 4 wt% of graphene shows 60% decrease of the H_2 permeability [292]. Up to 90% decrease in N_2 permeation is observed in thermoplastic polyurethane films reinforced with isocyanate treated GO of 3 wt% [293]. Whereas, the solution filtration synthesised PEI (polyethylenimine) functionalized reduced GO thin films with a brick and mortar structure show a significant decrease in the H_2 permeation rate with increasing PEI content due to tight packing and filling up of gallery spacings of the film assembly [294]. A considerably reduced O_2 and CO_2 permeation is observed in a layer-by-layer assembly of GO and PEI composite (Fig. 31) [295]. A 10 bilayer film (~91 nm thick) with 0.1 wt% PEI and 0.2 wt% GO mixtures deposited on a 179 µm PET shows O_2 transmission rate of 0.12 cm³/m²/day. A high H_2/CO_2 gas separation with a selectivity higher than 383 is observed, could be due to strong binding of CO_2 with the amine groups. A solvent blending prepared graphene-poly(ethylene vinyl alcohol) (RGO/EVOH) thin film (a thickness of about 0.2 mm) with only 0.5 wt% of RGO loading shows a significantly decreased permeable coefficient of O_2 nearly 1671 times lower than that of neat EVOH film [296]. The permeability measurements are carried out by a differential volume-variable pressure method at room temperature with 37% relative humidity and O_2 flow at 1 bar on 80 mm diameter film. The interesting gas barrier properties are attributed to a tightly packed nanobrick wall structure that creates super tortuosity and diffusion length for gas molecules.

Ultrathin (up to 20 nm) graphene and GO based membranes also show excellent gas permeation selectivities [297,298]. CVD grown large-area monolayer graphene films with increasing numbers of graphene sheets deposited on a Poly(1-methylsilyl-1-propyne) (PTMSP) substrate show improved O_2/N_2 selectivity suggesting that the gas diffusion through irregularly aligned defective graphene pores as well as slit-like interlayer spacings [297]. The GO thin-film membranes deposited on polye-
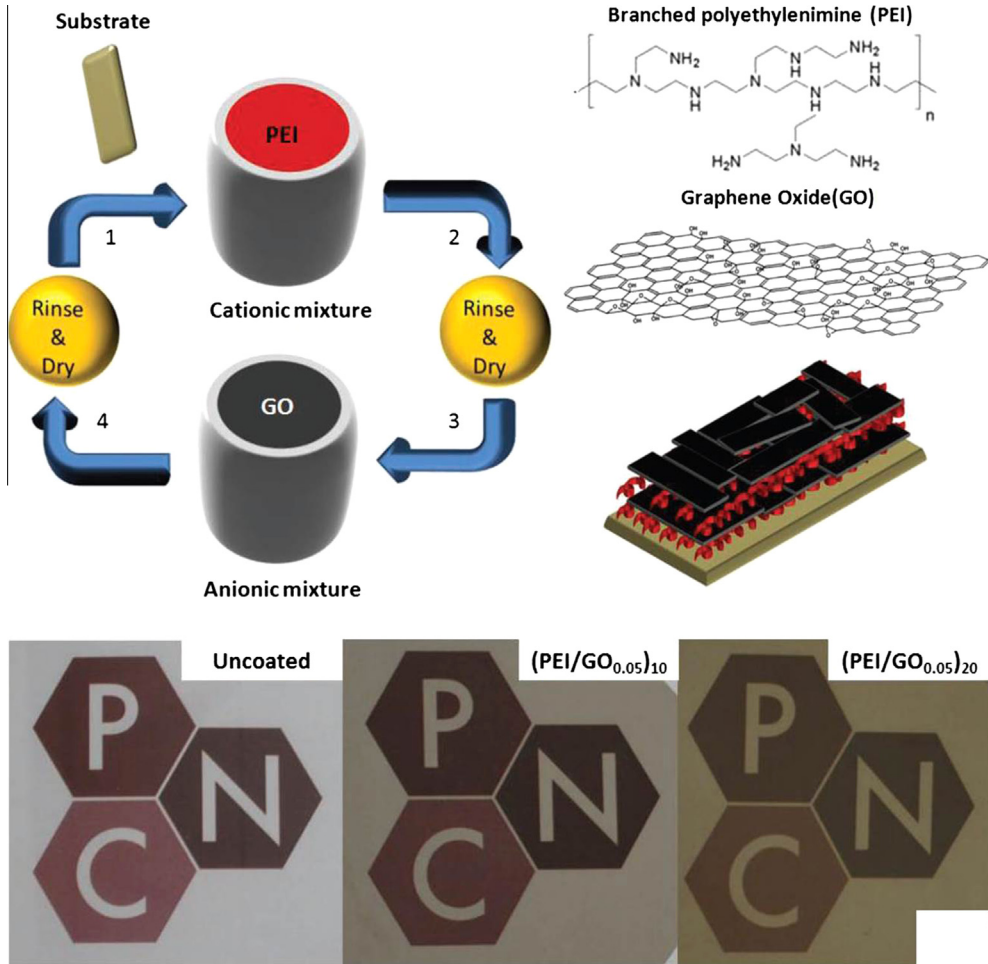
Fig. 31. Top: Schematic of the layer-by-layer deposition process. Steps 1–4 are repeated until the desired number of bilayers are achieved. Bottom: Images of (PEI/GO) 10 and (PEI/GO) 20 thin films on 179-μm PET to demonstrate transparency [295].

thersulphone supports in humidified state show a high selectivity of CO_2/N_2, which is ideal for post-combustion CO_2 capture. The gas permeance (in gas permeation units, GPUs) measured at a feed pressure of 1 bar, using the constant-pressure and variable-volume method shows very different gas transport behaviour (Fig. 32). Introduction of humidity in the feed stream enhances the CO_2 permeance leading to enhanced selectivities of CO_2/CH_4, CO_2/H_2 and CO_2/N_2. The highly interlocked layer structure of GO membranes shows a gas permeation in the order of $CO_2 > H_2 \geqslant He > CH_4 > O_2 > N_2$. As shown in Fig. 32d the separation performance of GO membrane in its dry and humidified state is higher than that reported for CO_2 for polymeric membranes, including thermally rearranged (TR) polymers, polymers of intrinsic microporosity (PIM), and inorganic membranes, such as carbons, silicas, and zeolites. A more permeable, H_2/CO_2 selective is demonstrated by creating thermally generated irreversible and small defective pores on the basal plane due to partly released surface oxygen-containing functional groups by thermal reduction of GO membranes. Overall the enhanced CO_2 selectivities are attributed to the CO_2-philic permeation behaviour, which is further enhanced by the presence of water. It is predicted that the incorporation of a carboxylic acid group lead to the highest isosteric heat. Although CO_2 is a nonpolar gas, the polarity of the individual C–O bonds
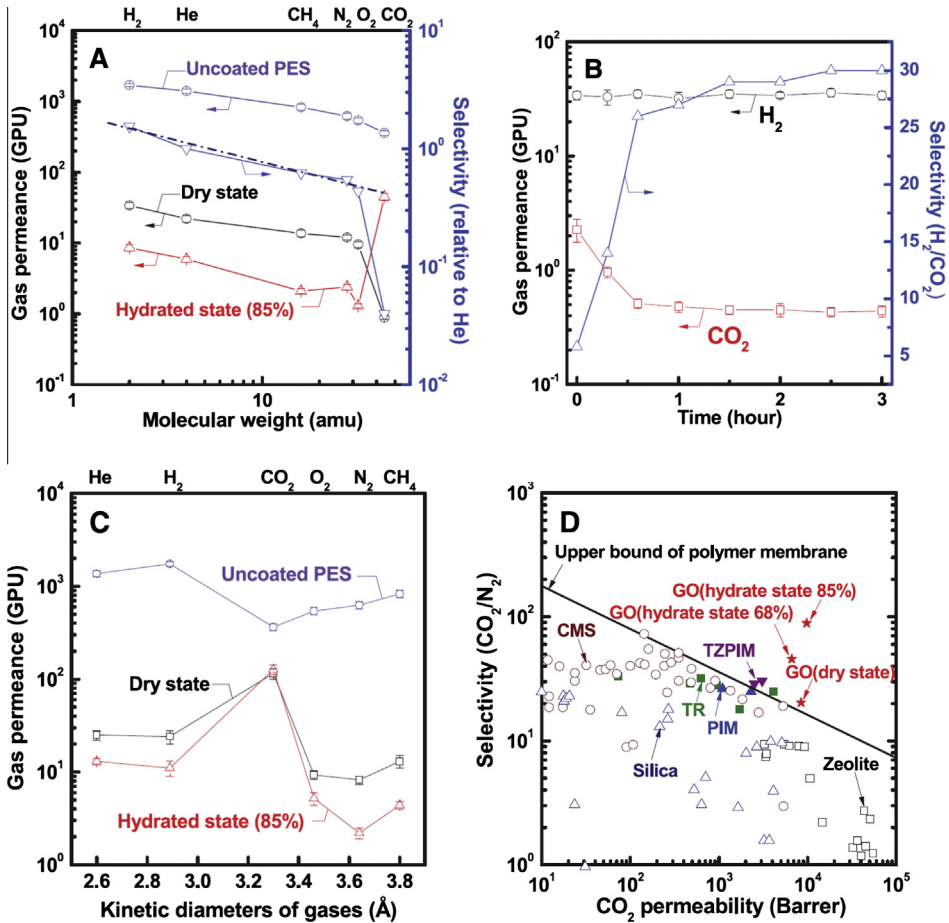
Fig. 32. Gas transport behaviour through ultrathin GO membranes. (A) Gas permeances of GO membranes as a function of molecular weight (method one; dashed line represents the ideal Knudsen selectivity) under dry and humidified conditions (amu, atomic mass unit). (B) H_2 and CO_2 permeances and H_2/CO_2 selectivity of method one GO membranes as a function of permeation time. (C) Gas permeances of GO membranes as a function of kinetic diameter (method two) under dry and humidified conditions. (D) Relation between CO_2 permeability and CO_2/N_2 selectivity of method two GO membranes under dry and humidified conditions [TR; tetrazole PIM (TZPIM) and PIM; CMS]. Error bars indicate the SD of all raw data [297].

in the molecule allows for interaction with polar groups in GO. Thus, CO_2 can act as a Lewis acid or a Lewis base and can participate in hydrogen bonding. Carboxylic acid groups on GO provide a preferential site for CO_2 adsorption, consequently retarding CO_2 transport in the nanopores by strongly trapping CO_2 molecules. This phenomenon is counterintuitive, because strong affinity between penetrant and nanopore walls often leads to surface diffusion of the penetrant preferentially sorbed on the pore wall, resulting in flux enhancement of highly sorbed or condensable penetrants. As such, these membranes are promising materials for industrial CO_2 separation processes related to petrochemical engineering (CO_2 removal from natural gas), the environment (CO_2 capture from flue gas), and biomass energy (CO_2 recovery from landfill gas).

Ultrathin (∼1.8–18 nm thickness) GO membranes prepared by vacuum filtration on anodic aluminium oxide (AAO) support from controlled dilution of GO dispersions show unusual H_2/CO_2 and H_2/N_2 separation selectivities as high as 3400 and 900 respectively, at 293 K [298]. Normally the micropo-

rous membranes show low H_2/CO_2 selectivity (<10) or are selective to CO_2 over H_2 at temperatures below 373 K due to a strong CO_2 adsorption and blocking of H_2 permeation. GO membranes with increasing thickness from 1.8 nm to 180 nm show exponential decrease in H_2 and He permeances. Here the gas permeance is mainly attributed to the selective structural defects within GO flakes. The GO interlayer spacing has minimal effect on molecular transport. The H_2/CO_2 separation selectivity decreased with increasing temperature, resulting from the faster increase of CO_2 permeance. A ~18 nm thick GO membrane on cellulous acetate support show H_2/CO_2 and H_2/N_2 separation selectivities of 1110 and 300, respectively. As shown in Fig. 33, the performance of the ultrathin GO membranes is far above the upper bound for polymeric (black line) and inorganic membranes.

4.9. NH_3, NO_2, H_2S and SO_2 sorption

The emissions of NH_3, NO_2, SO_2, and H_2S from the industrial plants during number of combustion processes, wastewater treatment, and food and compositing process are toxic, corrosive and malodor-

No.	Symbol	Membrane material	Temperature range, °C	Reference
1	●	Silica		(3)*
2	●	Silicon carbide		(26)
3	●	MFI Zeolite (modified)	100-300	(27)
4	●	ZIF-7		(28)
5	●	Zeolite composite		(29)
6	■	MFI zeolite (modified)		(30)
7	■	DDR zeolite	>300	(31)
8	■	Silica-titania		(32)
9	◆	MOF	<100	(33)
	■	GO (1.8-nm)		
10	●	GO (9-nm)	20-100	this work
	▲	GO (18-nm)		
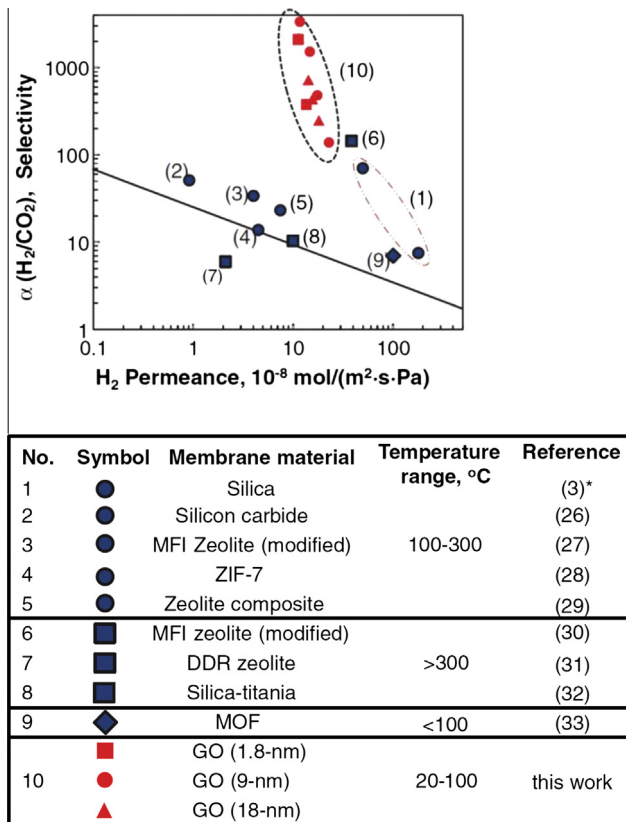
*Ideal selectivities and single gas permeances of H_2 from the reference

Fig. 33. Top: Comparison of ultrathin GO membranes with polymeric membranes and inorganic microporous membranes for H_2/CO_2 mixture separation (50:50 H_2/CO_2): selectivity versus H_2 permeance. The black line denotes the 2008 upper bound of the polymeric membrane for H_2/CO_2, assuming membrane thickness is 0.1 mm. Blue points (1–9) represent microporous inorganic membranes from the literatures; red points (10) indicate ultrathin GO membranes. The table at bottom explains points 1 through 10. ZIF, zeolitic imidazolate framework; MOF, metal–organic framework [298].

ous air pollutants. Due to growing demand for a more economical and improved process, there is always a need of search for new filtrate/adsorptive removal materials. Recently, the porous inorganic-graphene based materials for adsorptive removal of NH_3, NO_2, SO_2 and H_2S pollutants have been in focus of attention. Many theoretical and experimental studies are conducted for molecular adsorptive detection/capturing on graphene surfaces and GO based functionalised/inorganic hybrid porous structures. The DFT calculations suggest that adsorption of nitrogen oxides, NO_x: NO, NO_2, NO_3 on GO is generally stronger than that on pristine graphene due to the presence of active defect sites, such as the hydroxyl and carbonyl functional groups [299]. The interaction of NO_x with GO is expected to result in the formation of hydrogen bonds $OH\cdots O\,(N)$, weak covalent bonds $C\cdots N$ and $C\cdots O$, as well as the nitrous and nitric acid like moieties. First-principles calculations reveal that the oxygen groups on GO act as strong binding sites and induce dissociation of the NH_3 into the NH_2 or NH species by the H atom abstractions [300]. This further leads to the removal of surface oxygen species through the hydroxyl group hydrogenation and the ring opening of epoxy group. The reaction of NH_3 with the hydroxyl and epoxy groups is generally exothermic. From the first-principles calculations adsorption of H_2S onto pristine graphene is found to be very weak due to its small binding energy, large bonding distance and small net charge transfer [301]. Whereas, the Pt-decorated graphene bind up to seven H_2S molecules to one side of a Pt–graphene system due to large binding energy and a short Pt H_2S bonding length. The adsorption of several acidic gases (CO_2, NO_2 and SO_2) on light metal (Li, Al) decorated graphene oxide (GO) is also investigated with the first-principles calculations [302]. It is found that Li and Al could be anchored stably by hydroxyl and epoxy groups on GO and acts as strong adsorption sites for CO_2, NO_2 and SO_2 with improved binding energies up to (0.59, 2.29 and 1.08) eV, respectively, compared with Ti.

Experimentally, it is also identified that the acidic nature of GO with its carboxyl, hydroxyl, and epoxy groups act as energetic sites for chemical adsorption of gases, especially for polar molecules. A highly polar NH_3 interaction with the GO through gravimetric uptake measurements is demonstrated back in 1962 [303]. About 180 mg/g of NH_3 adsorption at room temperature and atmospheric pressure is observed. A physical adsorption at defective sites/or by hydrogen bonding with hydroxyl groups and a chemical interaction with the acidic sites and condensation in pores is proposed at low- and high-pressures, respectively. Therefore an increase in graphene inter layer distance proportional to the size of the ammonia molecule is observed.

Recently, there are renewed interests and increased investigations on NH_3 adsorption in various types of GO based materials, due to the development of promising and efficient new synthesis methods for obtaining GO and its composites. Bandosz's group have been actively exploring the NH_3, NO_2, H_2S and SO_2 adsorption and interaction properties in various types of GO and its composites with polymers, metal oxides, and MOFs [304–327]. The NO_2, NH_3 and H_2S molecules have a small kinetic diameter between (0.30–0.36) nm but exhibit different chemical properties (e.g., acid–base and redox properties). The amount of gas adsorption is demonstrated through the breakthrough measurements by passing a gas stream through a sample packed column with the option of either dry or up to 70% relative humidity at room temperature. The simple schematic of experimental setup is shown in Fig. 34 [304]. The effects of the degree of oxidation, reduction and exfoliation of the GO samples are examined for toxic gaseous adsorption. For example, a high NH_3 breakthrough capacity of 61 mg/g is observed in GO, dried at room temperature compared to 28 mg/g in GO dried at 393 K and 17 mg/g in GO exfoliated at 573 K [305–307]. The acid–base reactions and intercalations between the GO layers are identified as the main mechanisms of NH_3 retention. The NH_3 adsorption is very sensitive to the additional functional groups present in GO when different synthesis methods are employed. For example, GO prepared by the Brodie method, NH_3 is mainly retained via intercalation in the interlayer space of GO and reaction with the carboxylic groups at the edges of the graphene layers. On the contrary, the NH_3 reaction with the epoxy, carboxylic and sulphonic groups is observed in the Hummers GO [305]. In addition, the role played by surface texture, degree of oxidation and interlayer space/or pore structure on the NH_3 adsorptive retention is explained [306]. NH_3 dissolving in lamellar water as ammonium ions or by forming hydrogen bonding with epoxy and phenolic surface groups is also proposed [307,308]. The interaction of NH_3 with carboxylic groups is proposed as either Brønsted:
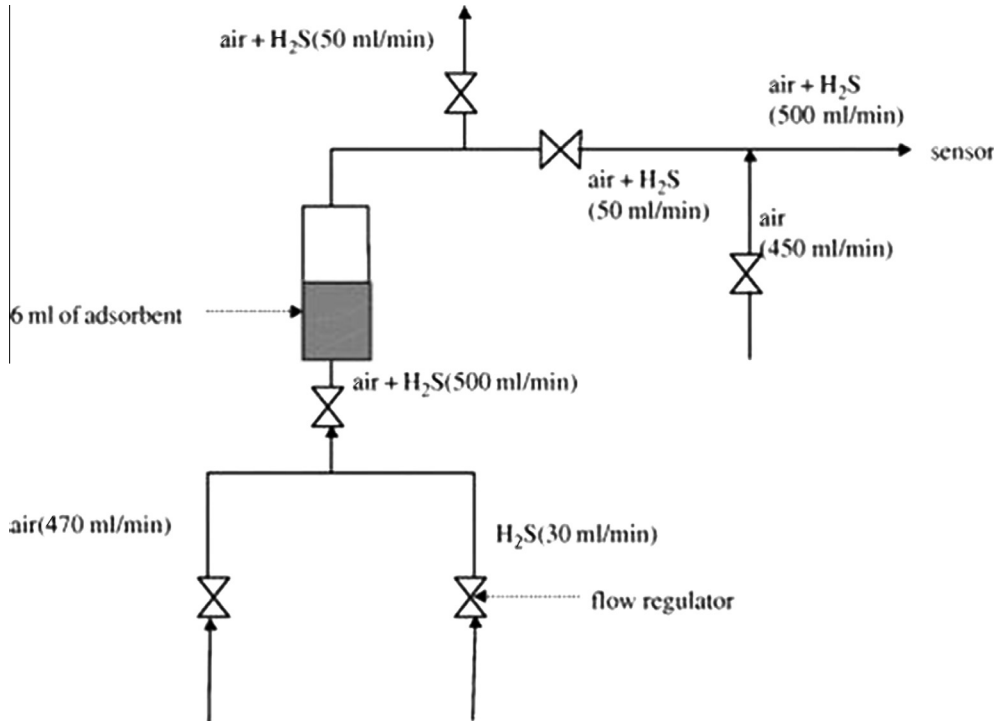
Fig. 34. Breakthrough capacity experimental set up [304].
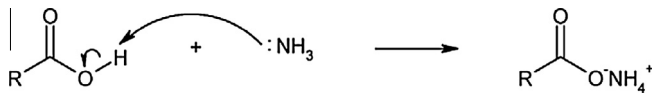
or Lewis acids:
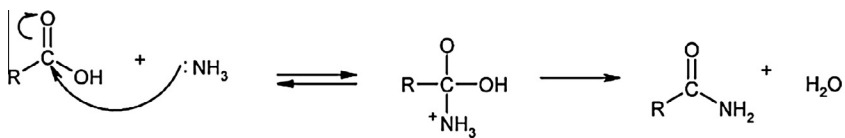
The second reaction seams more likely to happen in the dry conditions.

A variety of GO-composites are synthesised with the introduction of surface acidic groups, metal salts or solid acids. The intercalation of aluminium and aluminium–zirconium polyoxycations (also called Keggin type cations; in case of aluminium oxycation, the cations have one tetrahedral aluminium surrounded by twelve aluminium in octahedral coordinations, $[Al_{13}O_4(OH)_{24}(H_2O)_{12}]^{7+}$) in GO layers show a highly increased interlayer spacing (up to 1.5 nm) and NH_3 sorption due to additional Lewis and Brønsted acidic centres from the Keggin cations [310]. The GO–POM composites also show enhanced NH_3 sorption and retention than GO alone due to the interaction with the both bridging and terminal oxygens of POM (hydrogen bonded to the terminal oxygens of the POM could enhance the

acidity) [311]. POM is a kind of Keggin polyanion (consists of a central tetrahedron PO_4 surrounded by twelve octahedral MO_6 (M = W or Mo)) and exhibits a high acidity. The enhancement of NH_3 adsorption in clays–graphene composite is attributed to the synergistic effect of structure as well as graphene edge acidic groups and clay origin Brønsted or Lewis acidic centres [312]. The GO with simple metal-oxide (MnO_2) nanocomposites are also tested for NH_3 sorption [313].

Interestingly, GO in its dry condition show negligible adsorption for other pollutants; NO_2, H_2S and SO_2. However, an enhanced H_2S sorption (breakthrough capacity of 30 mg/g compared to zero in dry GO) is observed in a functionalised GO that is treated with NH_3 at 1223 K [314]. The NH_3 treatment results in decomposition and rearrangement of oxygen functional groups and incorporation of nitrogen mainly in pyridinic and quaternary entities. These nitrogen functionalities enhance the basicity and attract HS^- ions of dissociated H_2S via electrostatic interactions. The oxidation to elemental S and a smaller amount of SO_2 is also detected. The GO-metal oxide/hydroxide composites show enhanced sorption of NO_2, SO_2 and H_2S by forming nitrates, sulphide, sulphite and sulphates through the reactive paths (1) and (2) shown below [315–320]:

$$(1)$$

$$(2)$$
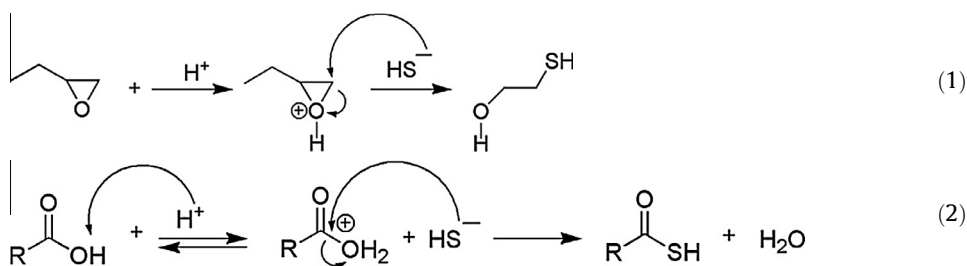
An iron-oxide (α-Fe_2O_3 and Fe_3O_4)-pillared graphene composite with a hydrophobic nanospace shows high activities for O_2, NO and NO_2 due to the interaction of NO with active γ-FeOOH and α-Fe_2O_3, and the formation of bridging nitrates [321,328]. Instant reduction of NO_2 to NO is noticed. A favourable adsorption and conversion of NO_2, and NO retention is also observed on GO-polyaniline (PANI) composites [322]. GO in its dry state show no NO_2 adsorption, however the sorption and retention of NO_2 is observed with the presence of N-methylformamide between GO layers due to polar and acid–base interactions.

The MOF-GO composites show an improved NH_3, NO_2, and H_2S sorption compared to the constituents because of synergistic effect related to the new pore space in the interface between MOF units and GO and a reactive interaction of metal sites and ligands either by hydrogen bonding (MOF-5) or coordination and subsequent complexation (HKUST-1) [323–327,329]. For example, the Lewis interactions of NH_3 and the Cu sites, (70–80) kJ/mol and the reaction of NH_3 with the ligands, (70–100) kJ/mol exhibit stronger binding energy. The NH_3 adsorption in Fe-MIL shows retention of the framework structure and thus could be useful for adsorbent regeneration. As shown in Figs. 35 and 36 initially dark blue HKUST-1 and its GO composites turned to light blue upon adsorption of NH_3, NO_2 and H_2S [323,329]. With the progress of the adsorption test, the colour of the sample further changed to a light blue or blackish tint during exposure to NH_3 and H_2S, respectively. The first colour change is attributed to the coordination to the Cu sites due to the presence of a lone pair of electrons on the adsorbate molecules. The second colour change is likely caused by the formation of new complexes like CuS. The reactive decomposition in HKSUT-1 is attributed to the formation of the $Cu(NH_3)_4^{2+}$, CuS and $Cu(NO_3)_2$ for adsorption of NH_3, H_2S and NO_2, respectively. In Zn-MOF-GO composites, NH_3 interact through hydrogen bonding with the oxygen atoms of the ZnO_4 units whereas for Fe-MIL-GO composites, the acid–base reaction thought to be the reactive pathway between the NH_3 and water coordinated Fe sites.

Long et al. show an oxidative absorption of SO_2 in the porous GO foams, prepared by freeze-drying technique [330]. As shown in Fig. 37 the GO foams exhibit a high porosity and resemble a sponge-like appearance. The oxidative adsorption of SO_2 to SO_3 by reduction of GO at room temperature is observed in a dry condition. Whereas, the reaction is intense with the GO water suspension; the GO is reduced quite fast and SO_2 becomes SO_4^{2-}.
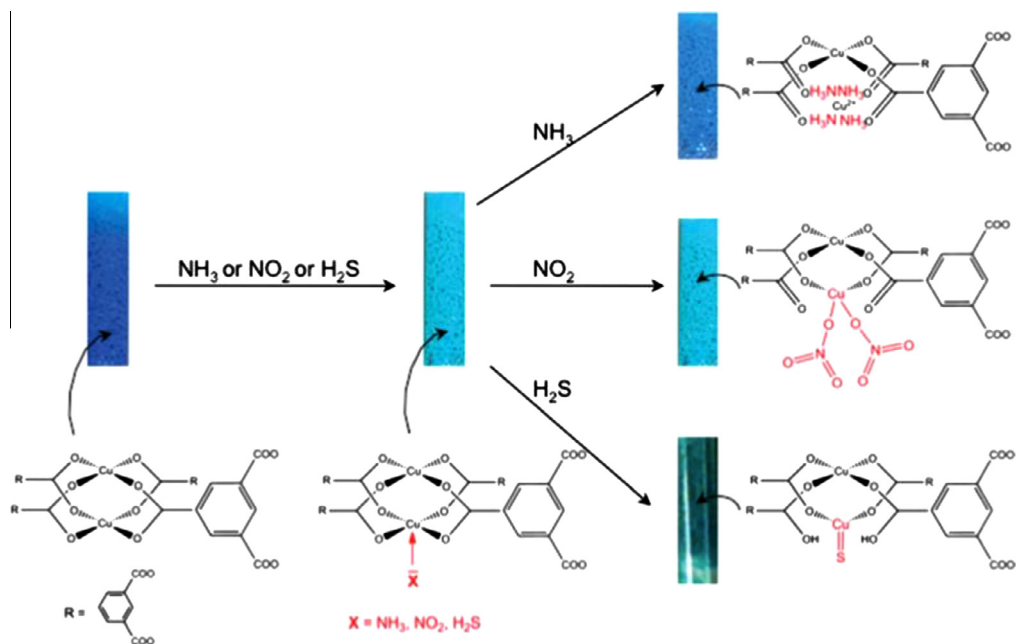
Fig. 35. Schematic of the adsorption process of NH_3, H_2S and NO_2 on the HKUST-1 with evidence of the colour changes and the identification of the reactions products [323].
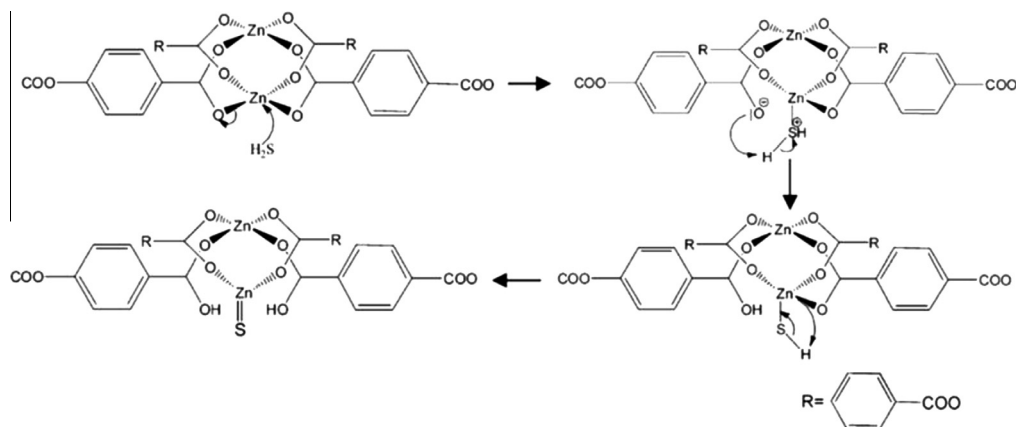
Fig. 36. Mechanism of the de-sulphurization process of MOF-5/GO composites [329].

5. Summary and perspectives

As discussed above and shown in Figs. 1 and 2, there exist a wide range of graphene/GO based materials; starting with expanded graphite, intercalation, exfoliation, chemical reduction, pillared layers, self-assembly, thin-film membranes, functionalization, doping, metal dispersion, porous template and chemical activation. Those are investigated for gas sorption, storage and separation. In particular, the experimental H_2 and CO_2 uptake results are comparatively analysed in various graphene based materials, as indicated in Tables 2–5, along with the SSA and the measurement conditions (particu-
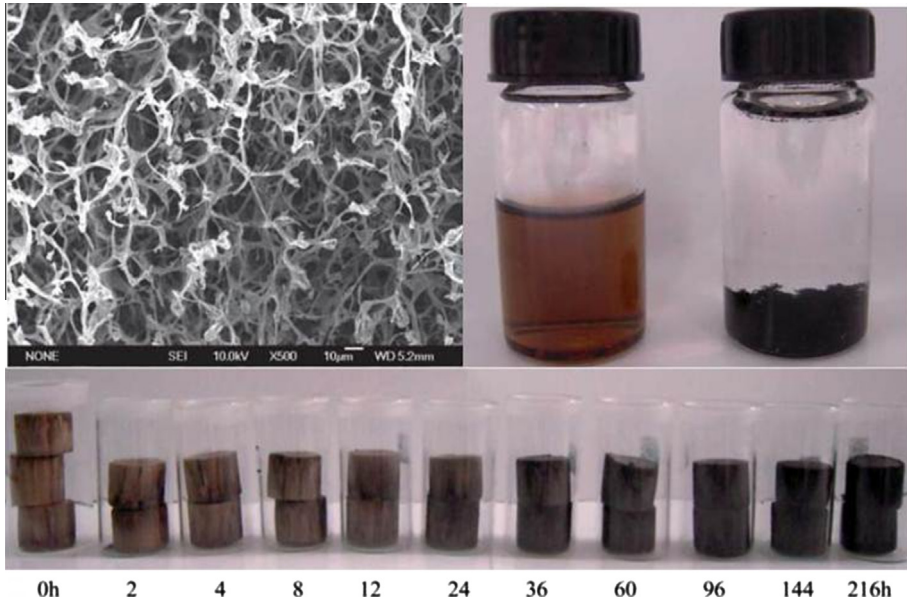
Fig. 37. Top: SEM image of GO foam, and GO solution before (brown) and after (dark) coming in contact with SO_2 gas, clearly showed a reduction of GO. Bottom: Colour change of GO foams exposed to SO_2 gas in dry form. The SO_2 gas is introduced into the column containing the GO foams, the colour of the foams gradually changed from brown to black. This suggests that the GO reacted with the SO_2 gas and the extent of the reaction gradually increased with time [330].

Table 2
Experimentally reported H_2 adsorption capacities in exfoliated and reduced GO based materials.

Sl. no.	Type of graphene material	Specific surface area (m^2/g)	H_2 uptake (wt%)		Ref.
			77 K	298–300 K	
1	Exfoliated GO	156	0.4 (1 bar)	<0.2 (60 bar)	[199]
2	Exfoliated GO	300	1.75 (54 bar)	0.1 (40 bar)	[200]
3	Exfoliated GO	470	–	0.7 (40 bar)	[249]
4	Exfoliated GO	477	1.2 (1 bar)	–	[202]
5	Exfoliated GO	477	1.4 (1 bar)	–	[254]
6	Diamond derived graphene	520	0.68 (1 bar)	2.5 (100 bar)	[207]
7	Expanded graphite nanofibers	67 & 555	0.19 & 0.39 (1 & 20 bar)	0.29 (20 bar)	[220]
			0.45 & 1.2 (1 & 20 bar)	0.03 (20 bar)	
8	Hydrazine reduced GO	640	0.68 & 1.2 (1 & 10 bar)	0.72 (100 bar)	[201]
9	Exfoliated GO	925	1.38 (1 bar)	3.1 (100 bar)	[207]
10	Glucose reduced GO	1206	–	2.7 (25 bar)	[203]
11	Outgassed GO and annealed GO	480 & 1305	1.4 & 4.0 (1 bar)	–	[208]
12	Magnesium combustion derived graphene	236	0.85 (65 bar)	0.9 (300 bar)	[205]
13	Camphor, Diamond and GO derived graphenes	46–1550	0.05–1.7 (1 bar)	–	[206]
14	Exfoliated GO by CO_2 pressure swing	141–547	–	0.7–1.8 (100 bar)	[204]

larly, pressure and temperature). As specific surface area and pore volume are the key porous parameters to determine the physisorption capacity Fig. 38 shows the H_2 uptake in a wide variety of graphenes against the SSA and pore volume. The structure modification effect on the binding, heat of H_2

Table 3
Experimentally reported H_2 adsorption capacities in various pillared graphene based materials.

Sl. no.	Type of graphene material	Specific surface area (m^2/g)	H_2 uptake (wt%)		Ref.
			77 K	298–300 K	
1	K-GIC, KC_{24}	–	1.2 (1 bar)	–	[218]
2	GO-MWCNTs	–	–	2.6 (50 bar)	[234]
	LC-GO			1.4 (50 bar)	
3	Self-pillared GO	57–192	1.1–4.8 (90 bar)	0.28–0.46 (90 bar)	[222]
4	Diazonium linked graphene	260–440	1–1.6 (2 bar)	–	[229]
5	GOFs	26–470	0.35–0.92 (1 bar)	–	[107,227]
6	GPOM	580 & 680	1.3 & 0.8 (1 bar)	–	[226]
7	GMNPs	418–901	0.88–1.44 (1 bar)	–	[225]
8	Silylated GO	562–942	–	0.2–0.4 (100 bar)	[233]

Table 4
Experimentally reported H_2 adsorption capacities in doped, functionalised, activated, templated, bottom up graphene based materials.

Sl. no.	Type of graphene material	Specific surface area (m^2/g)	H_2 uptake (wt%)		Ref.
			77 K	298–300 K	
1	20 wt% Pd–graphene	–	–	3.0 (40 bar)	[249]
2	N-doped	146	–	1.4 (40 bar)	[250–
	Pd–N–graphene			1.5 & 4.5 (40 bar)	252]
3	Expanded nanofibers	227	5 (100 bar)	–	[258]
4	Exfoliated GO–24 wt% Pd	80–230	0.3–0.5 (1 bar)	0.1–0.26 (1 bar)	[244]
5	Ni–B nanoalloy decorated graphene	–	2.8 (1 bar)	–	[253]
		272	4.4 (1 bar)	1.9 (1 bar, 273 K)	[254]
6	Exfoliated GO & its Pt and Pd composites	755	–	0.07 (57 bar & 303 K)	[247]
		480–545		0.16 (57 bar & 303 K)	
7	Pd–graphene/carbon composites	300/3328	–	0.82 (80 bar & 298 K)	[248]
6	12 wt% Pd_4Hg alloy decorated GLF	450	–	2.3–5.25 (20 bar)	[256]
7	10 wt% Pd decorated GLF	687	–	0.98 (100 bar)	[257]
8	Bottom up & functionalised graphenes	200–900	0.5–1.7 (2 bar)	–	[262]
9	Template CVD graphene	2038	–	1.5 (90 bar & 274 K)	[267]
10	Bottom up graphene	2139	–	0.9 (100 bar)	[261]

adsorption is shown Fig. 39. Earlier, the H_2 uptake capacity against the SSA of a wide range of other porous carbons is generalised and is normally accepted that for every 500 m^2/g of SSA, the H_2 uptake capacity at 77 K is increased by $\sim$0.5 wt% at 1 bar and $\sim$1 wt% at high pressures [82,331,332]. Similarly, at room temperature and pressures up to 100 bar the H_2 storage in a wide variety of porous carbons is found to be well below 1 wt% [333]. From Fig. 38 one can clearly understand that the modified graphenes with carefully tuned pore structure or pillaring or chemical modifications (doping, functionalization and metal dispersion) performed much better than simply exfoliated graphenes. At 77 K, most of the exfoliated/reduced graphenes seems to exhibit more or less similar uptake capacities compared to the other porous carbons with respect to the porosity. Normally the exfoliation leaves very high mesoporosity due to the highly curved nature of graphenes. However, it is understood that the modified graphenes enhance the microporosity and functional active sites. Thus comparatively a high H_2 uptake is seen in optimised GO structures, with doped, defective, and metal/alloy nanoparticle dispersed graphenes due to the synergistic effect of enhanced microporosity, binding sites or combined molecular and spillover/dissociative atomic hydrogen adsorption. Most importantly these graphene based materials exhibit very promising H_2 uptake capacities between (1–4) wt% at 300 K compared to the maximum of up to 1 wt% in most porous solid adsorbents, i.e. MOFs, zeolites and nanostructured carbons. This is further evidenced by a high heat of H_2 adsorption mostly between

Table 5
Experimentally reported CO_2 adsorption capacities in a variety of graphene based materials. The respective available surface area and references also included for readers further interests.

| Sl. no.	Type of graphene material	Specific surface area (m^2/g)	CO_2 uptake (mmol/g)	Ref.
1	GO	31	1.7 (1 bar & 273 K)	[242]
	GO-PEI hydrogel	253	2.5 (1 bar & 273 K)	
	Reduced GO	876	1.84 (1 bar & 273 K)	
2	Outgassed GO	477	0.7 (1 bar & 273 K)	[202]
2	Exfoliated GO	925	8.6 (1 bar & 195 K)	[207]
3	Hydrogen exfoliated GO	443	21.6 (11 bar & 298 K)	[210]
4	Exfoliated nanoplatelets	480	56 (30 bar & 298 K)	[211]
5	Exfoliated GO	701	39 (30 bar & 298 K)	[211]
6	Graphene–polyanilene	–	70 (10 bar & 298 K)	[213]
7	Amine grafted GO	Nonporous	1.2 (15% CO_2, 40 ml/min, 303 K)	[212]
8	GO–Mn_3O_4	541	2.5 (1 bar & 298 K)	[224]
9	GOFs	470	2.7 (4 bar & 300 K)	[107]
10	GLF	510	2.0 (10 bar & 298 K)	[255]
11	Exf-GO by CO_2 pressure swing	140–547	2.3–6.4 (30 bar & 298 K)	[204]
12	KOH activated GO	1894	2.0 & 19 (1 bar & 26 bar & 298 K)	[263]
13	KOH activated GO & N-doping	1360	4.0 (1 bar & 300 K)	[264]
14	KOH activated polythiophene-reduced GO	1396	4.5 (1 bar & 298 K)	[266]
15	Template CVD graphenes	2038	36.5 (31 bar & 274 K)	[267]
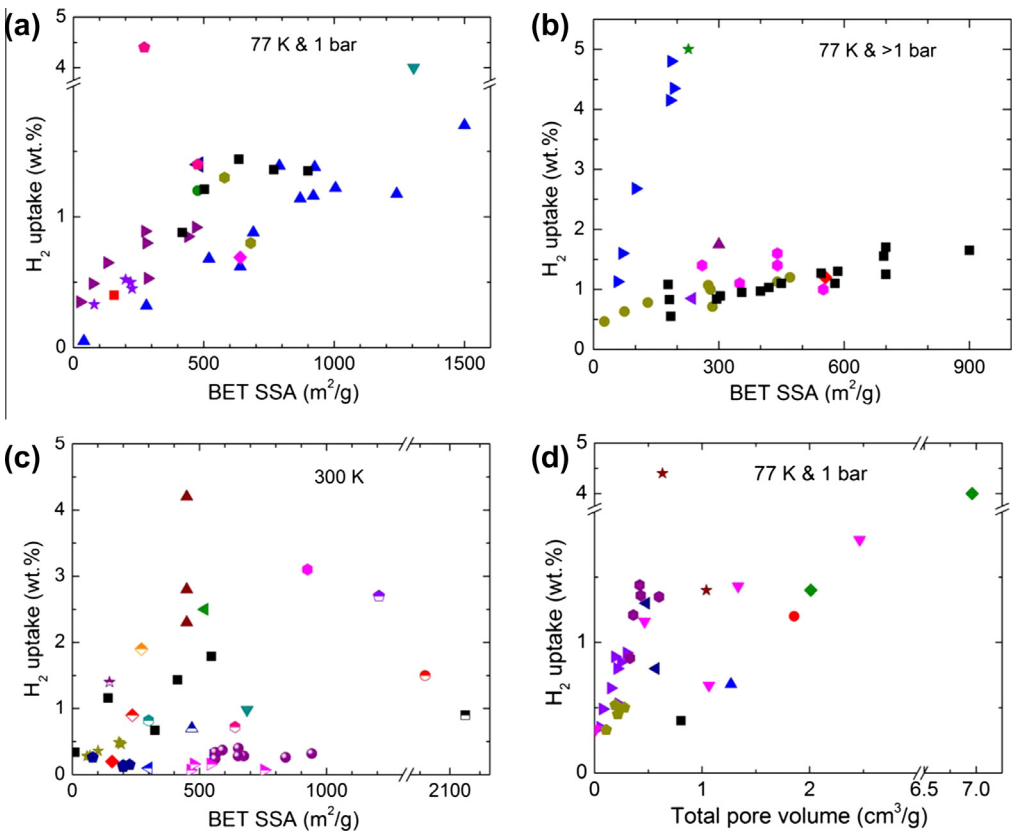
Fig. 38. Experimentally obtained H_2 uptake capacity versus surface area in various types of graphene based materials; (a) 77 K and 1 bar, (b) 77 K and high pressure, >1 bar, (c) ~300 K and all pressures. (d) H_2 uptake capacity at 77 K and 1 bar against pore volume of various graphenes. The materials can be identified with the corresponding values given in Tables 2–4.
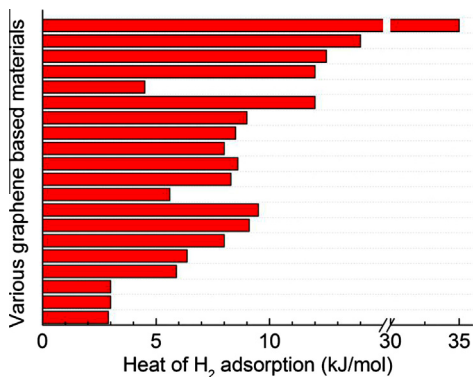
Fig. 39. Experimentally derived heat of H_2 adsorption in various types of graphene based materials.

(8–15) kJ/mol in the modified graphenes, compared to a typical (4–6) kJ/mol in other porous carbon adsorbents. These facts are clearly encouraging and help to minimise the gap between DOE targets and experimental results. Similarly, the highest CO_2 capacity is reported in functionalised/doped and highly porous activated graphene materials (Table 5). The graphene based materials are also found to exhibit enhanced CH_4 storage that surpasses the DOE target and other traditional highly porous carbons and most of the MOFs. The graphene-based composites also show enhanced NH_3, NO_2, SO_2 and H_2S sorption and retention. The theoretical and experimental results on the graphene related membranes for gas separations are very encouraging.

Because of multifunctionality of the graphene-based materials many approaches have been adapted to develop various robust interconnected porous network architectures with various functional groups. Clearly, by controlling the synthesis parameters and tuning the pore parameters; increasing SSA and microporosity, the chemical modification of graphenes could be a very promising in obtaining practicable gas sorption, storage and separation. There are many possible routes still available to engineer graphene structures. For example, a number of robust 3D hierarchical porous graphene structures have been developed through self-assembly, sol–gel and cross-linking chemistry [43,334–338]. A vacuum centrifugal evaporation has been introduced as a strategy for a large scale synthesis of GO sponges with 3D interconnected network hierarchical structure [334]. Subsequent thermal annealing of the GO sponges result in recovery of sp^2 graphene structure, forming graphene sponges with a large SSA and typical porous structure. An autoclaved leavening and steaming of GO layer films lead to reduced GO foams with open porous and continuously cross-linked structures [335]. Compared to reduced GO films, the reduced GO foams show greatly improved performance as selective organic absorbents. Furthermore, the doping of the graphene foams is performed to enhance its functionalizability. These graphene foams and its thin film forms could be ideal candidates for an efficient gaseous separation.

Optimised pillared graphene structures with amine-based functional groups could produce superior CO_2 adsorbents (pillared GOs with NH_2 groups like silicas with NH_2). Much stable structures may be developed due to strong nucleophilicity of amines and epoxy groups on GO through a ring opening reaction without any activation. Using sol–gel method low-density graphene aerogels with tuneable SSA, (584–1200) m^2/g and very high pore volume, (2.96–6.4) cm^3/g are synthesised [336]. In another method by gelation of a GO suspension under basic conditions, a robust 3D macroassembly of graphene sheets is obtained with SSA > 1300 m^2/g [337]. Furthermore, the chemical activation of graphene aerogels with KOH results in highly increased microporosity (up to 0.69 cm^3/g) and SSA (up to 1715 m^2/g) [338]. Similarly, CO_2 activation of the mechanically robust, centimetre sized self-assembled interconnected networks of single-layer graphene aerogel monolith increases the SSA up to 3000 m^2/g compared to the typically 400 m^2/g for the non-activated foam [339]. Thus, adjusting synthetic parameters allow a wide range of control over surface area, pore volume and pore size, as

well as the nature of the chemical cross-links (sp^2 versus sp^3) making these materials promising candidates for gas sorption and storage applications.

A method for preparing functionalized 3D carbon-based architectures, consisting of high SSA mesoporous carbon spheres (MCS) with a particle size of 60 nm intercalated between graphene sheets (GS) is demonstrated by Lei et al. [340]. The MCS itself consists of graphene sheets in small domains and exhibits a SSA and pore volume of 2396 m^2/g and 2.9 cm^3/g, respectively, obtained from silica template and ferrocene by CVD method. MCS-GS composite shows hierarchical porous architecture with SSA of 1496 m^2/g and pore volume of 3.36 cm^3/g with enhanced microporosity. Further thermal treatment of GMC-GS in NH_3 yields N-doped product. The N-containing basic groups could be very useful in obtaining improved CO_2 adsorption at low-pressures due to enhanced acid–base interactions. In addition, a wide variety of high and tuneable surface area and pore structure assemblies of graphenes with chemical functionalization are demonstrated through template, pyrolysis and chemical activation methods [341,342]. For example, the silica and zeolite based templates are conveniently used to produce a very high SSA and pore volume graphenes and carbons. In particular, by controlling the pore size of silica one could obtain much more enhanced microporosity than the reported methods of producing mesoporous graphene structures. Other possible methods, such as soft co-polymer or sacrificial salt or nanoparticle templating, could provide desirable structures as well. The chemical activation is another promising method in which the tailor made porous graphene structures are highly possible by simply choosing the right activator; KOH, NaOH, Na_2CO_3, CO_2, steam, etc. together with concentration and temperature [342]. The chemical modification, functionalization and hybrid structures of graphene based highly porous materials [343–368] could have attractive gas sorption and storage properties. The boron- and nitrogen co-doped and porous graphene like materials should help in obtaining higher gas sorption and storage. Zhang et al. show that a very efficient and industrially scalable approach of synthesising defect/wrinkle mesopore structure graphene sheets with a very high SSA up to 3523 m^2/g and total pore volume up to 2.4 cm^3/g [366]. The material obtained through the following two standard industry steps: (1) in-situ hydrothermal polymerisation/carbonisation of the mixture of cheap biomass or industry carbon sources with GO to get the 3D hybrid precursors; and then (2) a KOH chemical activation step. An enhanced surface area and pore volume is also obtained with the addition of GO to mesoporous carbon. Tuneable surface area and porosity parameters are also demonstrated in mesoporous carbons with the controllable addition of GO.

Recently, graphenic type fragments are synthesised from zeolites/MOFs as templates, with either self- or addition of small molecular carbon precursors [369–375]. Upon carbonisation, the organic linker ligand in MOF transforms into single layers functionalised graphene fragments with new hierarchical high slit-like micropores and mesopores while retaining the MOF framework porosity. These carbons with new pore types show ultrahigh porosities i.e., simultaneous high surface area (up to 3300 m^2/g) and micro- and total-pore volumes (up to 5.53 cm^3/g) [369,372]. These functionalised carbons yield exceptionally high H_2, CH_4 and CO_2 uptakes compared with the capacities of those benchmark microporous materials under identical conditions. In particular, a gravimetric (volumetric) H_2 uptake of 3.25 wt% and 7.3 wt% (50 g/l) are achieved at 77 K under 1 bar and 20 bar, respectively [369,370]. At 100 bar and 298 K, these carbons show ~0.94 wt% of H_2 storage. The functionalised MOF carbons also show record high CH_4 and CO_2 uptakes [372–375]. For example, the room temperature uptake of up to 4.6 mmol/g at 1 bar and over 27 mmol/g (119 wt%) at 30 bar are again some of the highest values reported in the literature for porous carbons. The overall synthesis and gas uptake mechanism of such graphenic type MOF carbons is schematically shown in Fig. 40.

The novel ultrathin, robust nanocomposite membranes by incorporating GO sheets into silk fibroin matrix through heterogeneous surface interactions in organised layer-by-layer manner show outstanding mechanical properties, with a tensile modulus of 1.45×10^6 bar (145 GPa), an ultimate stress of more than 3000 bar (300 MPa), and a toughness of above 2.2 MJ/m^3 [376]. These nanocomposite membranes in their support and free-standing state could be valuable for potential applications in protective molecular coatings, permeable membranes for separation and delivery. A new avenue for graphene-based ultra-films anchored on solid supports with a high stability and controlled thickness via a layer-by-layer assembly is demonstrated using amino-substituted π-conjugated compounds, including 1,4-diaminobenzene, benzidine, etc., as cross-linkages [377]. A thermal annealing leads to a reduction of the films thus could yield suitable pore space for molecular sieving. Furthermore, the
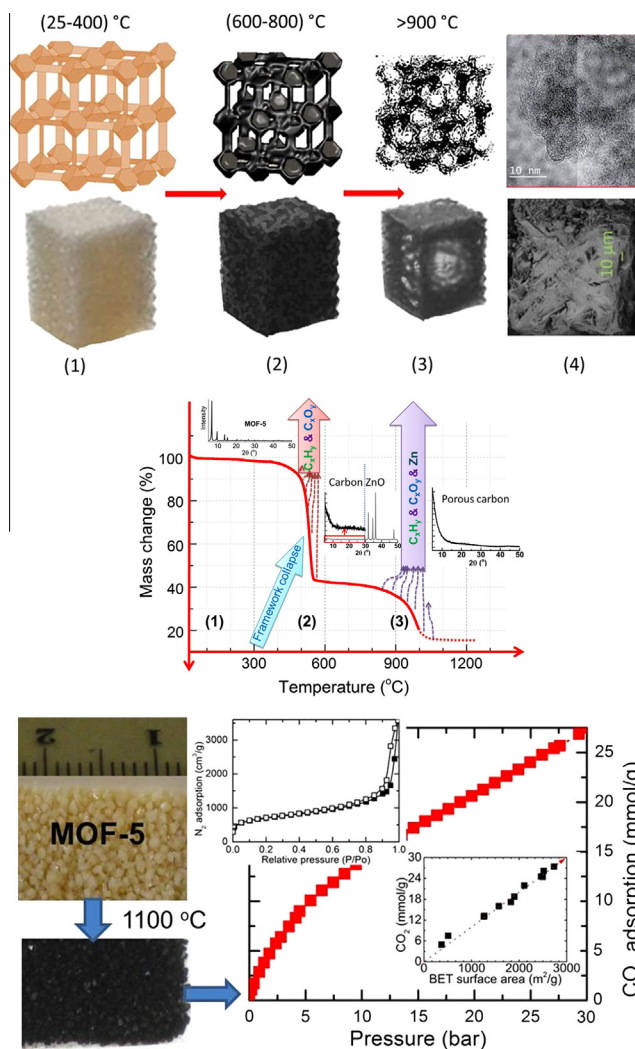
Fig. 40. Top: Schematic illustration for steps in fabricating hierarchical porous graphene carbons (HPCs) from a precursor MOF-5; (1) MOF framework/crystal structure (up to 400 °C) with well-defined pore structure in the micropore region, (2) decomposition, and metal-oxide formation, ZnO and carbon between 600 and 800 °C yielding poor pore development, (3) at >900 °C, ZnO reduction and evaporation of Zn and CO yields highly porous carbon with a hierarchical pore structure and (4) surface morphology of HPCs by TEM and SEM. Middle: Mechanism involved in the carbonisation process of MOF-5 through simultaneous thermogravimetric analysis (TGA), mass spectroscopy (MS) and powder X-ray diffraction (PXRD). The first mass-loss between 400 °C and 600 °C, is attributed to the framework decomposition leading to a major release of carbon containing gaseous products (mostly CO_2, CO, C_6H_6 and a small amount of H_2 and C_xH_y hydrocarbon mixtures), where a formation of crystalline hexagonal ZnO occurs (sharp XRD peaks). The second mass-loss starting at ~900 °C is due to further release of CO_2 and CO with Zn through the reduction of ZnO by carbon via ZnO + C/Zn(g) + CO. The carbonisation yields materials with either a featureless XRD pattern or very weak and broad XRD peaks between 20° and 25°, and at ~45° of two-theta indicating the disorderly oriented tiny graphenic type fragments in the structures. It is worth noting that the reduction of ZnO by carbon during carbonisation yields a pure porous carbon. Bottom: Porosity and CO_2 uptake characteristics of HPCs. The 77 K N_2 adsorption isotherms on the millimetre-sized MOF-5 derived HPCs show simultaneously high surface area, up to 2734 m^2/g, and exceptionally high total pore volume, up to 5.53 cm^3/g. In the HPCs, micropores are mostly retained and meso- and macro-pores are generated from defects in the individual crystals, which is made possible by structural inheritance from the MOF precursor. The resulting HPCs show a significant amount of CO_2 adsorption, over 27 mmol/g (119 wt%) at 30 bar and 27 °C. Inset also show a direct relationship between the CO_2 adsorption capacity and the surface area: a CO_2 uptake of 10 mmol/g for every 1000 m^2/g increase of surface area under 30 bar and 27 °C [372].

amine groups could show selective gas permeations. A simple and effective method of preparing functional nanoporous graphene/carbon composite membranes from MOFs is also demonstrated and reviewed [378,379]. The resulting symmetric dense or asymmetric composite membranes exhibit good performance in gas separation and liquid separation via pervaporation.

6. Conclusion

In summary, the rich chemistry of graphene nanosheets have offered great potential for the design and development of many combinations of interconnected porous graphene-based materials as promising molecular adsorbents, with high thermal/chemical stability, tuneable specific surface area and pore structure. The other advantages are the relatively low cost and easy scale-up associated with the manufacturing of the porous graphene carbons. Graphene and its composites have been used as adsorbents for low temperature physisorption and high temperature chemisorption of H_2, CO_2, CH_4, etc., showing promising results, especially when compared with conventional high surface area activated carbons. As highlighted in this report, the interest in gas sorption and storage by physical adsorption has grown considerably over the last few years. While many computational studies prove strong potential of graphene and its derivatives, practical developments have advanced markedly in molecular pillaring, metal dispersion, doping, functionalization and 3D interconnected networks to enhance gas sorption and storage. Clearly, there still exist several challenges in practice, such as the effective control of the desirable binding sites, porosities and functionalities; the balance of functional properties with structural integrity; and further tuning of molecular selectivities in gas mixtures for purification and sensing.

More specifically, there have been many attempts to use carbon adsorbents as reversible H_2 storage materials. Most of the measurements so far have been conducted at 77 K, which limits the practicality. Similarly, carbon capture at ambient conditions is not satisfactory. As summarised in Tables 2–5, and Figs. 38 and 39, the remarkable synergistic properties from combining GO hybrid structures showed promising room temperature H_2 storage and high pressure CH_4 and CO_2 adsorption capacities. For the given rich chemistry and functionalizability of graphene, the number of new compounds are continuously being tailor-made. Thus if carefully tuned the microporosity and the high surface area of the chemically modified graphene materials could be very promising for H_2 and CH_4 storage and CO_2 capture. Similarly, the gas permeation separation on graphene and GO based membranes is highly dependent on GO sheet size and thickness, layer structure and assembly, residual lamellar water content, and deformation of thin-layered structures during dewetting can all effect. There is much scope in tuning and controlling the parameters to develop practically useful membranes.

Acknowledgement

References

[1] Pierson HO. Handbook of carbon, graphite, diamond and fullerenes. NJ, USA: Noyes; 1993.
[2] Dai L, Chang DW, Baek JB, Lu W. Carbon nanomaterials for advanced energy conversion and storage. Small 2012;8:1130–66.
[3] Dreyer DR, Ruoff RS, Bielawski CW. From conception to realization: an historial account of graphene and some perspectives for its future. Angew Chem Int Ed 2012;51:7640–54.
[4] Novoselov KS, Falko VI, Colombo L, Gellert PR, Schwab MG, Kim K. A roadmap for graphene. Nature 2012;490:192–200.
[5] Sarma SD, Adam S, Hwang EH, Rossi E. Electronic transport in two-dimensional graphene. Rev Mod Phys 2011;83:407–70.
[6] Abergel DSL, Apalkov V, Berashevich J, Ziegler K, Chakraborty T. Properties of graphene: a theoretical perspective. Adv Phys 2010;59:261–482.
[7] Georgakilas V, Otyepka M, Bourlinos AB, Chandra V, Kim N, Kemp KC, et al. Functionalization of graphene: covalent and non-covalent approaches, derivatives and applications. Chem Rev 2012;112:6156–214.
[8] Chen Y, Zhang B, Liu G, Zhuang X, Kang ET. Graphene and its derivatives: switching ON and OFF. Chem Soc Rev 2012;41:4688–707.
[9] Wei W, Qu X. Extraordinary physical properties of functionalized graphene. Small 2012;8:2138–51.
[10] Kuila T, Bose S, Mishra AK, Khanra P, Kim NH, Lee JH. Chemical functionalization of graphene and its applications. Prog Mater Sci 2012;57:1061–105.

[11] Sun Z, James DK, Tour JM. Graphene chemistry: synthesis and manipulation. J Phys Chem Lett 2011;2:2425–32.
[12] Huang X, Qi X, Boey F, Zhang H. Graphene-based composites. Chem Soc Rev 2012;41:666–86.
[13] Singh V, Joung D, Zhai L, Das S, Khondaker SI, Seal S. Graphene based materials: past, present and future. Prog Mater Sci 2011;56:1178–271.
[14] Huang X, Yin Z, Wu S, Qi X, He Q, Zhang Q, et al. Graphene-based materials: synthesis, characterization, properties, and applications. Small 2011;7:1876–902.
[15] Weiss NO, Zhou H, Liao L, Liu Y, Jiang S, Huang Y, et al. Graphene: an emerging electronic material. Adv Mater 2012;24:5782–825.
[16] Bonaccorso F, Sun Z, Hasan T, Ferrari AC. Graphene photonics and optoelectronics. Nat Photon 2010;4:611–22.
[17] Yavari F, Koratkar N. Graphene-based chemical sensors. J Phys Chem Lett 2012;3:1746–53.
[18] Huang X, Zeng Z, Fan Z, Liu J, Zhang H. Graphene-based electrodes. Adv Mater 2012;24:5979–6004.
[19] Xiang Q, Yu J, Jaroniec M. Graphene-based semiconductor photocatalysts. Chem Soc Rev 2012;41:782–96.
[20] Basu S, Bhattacharyya P. Recent developments on graphene and graphene oxide based solid state gas sensors. Sens Actuat B 2012;173:1–21.
[21] Zhao G, Wen T, Chen C, Wang X. Synthesis of graphene-based nanomaterials and their application in energy related and environmental-related areas. RSC Adv 2012;2:9286–303.
[22] Zhang N, Zhang Y, Xu YJ. Recent progress on graphene-based photocatalysts: current status and future perspectives. Nanoscale 2012;4:5792–813.
[23] Shao Y, Wang J, Wu H, Liu J, Aksay IA, Lin Y. Graphene based electrochemical sensors and biosensors: a review. Electroanalysis 2010;22:1027–36.
[24] Choi HJ, Jung SM, Seo JM, Chang DW, Dai L, Baek JB. Graphene for energy conversion and storage in fuel cells and supercapacitors. Nano Energy 2012;1:534–51.
[25] Machado BF, Serp P. Graphene-based materials for catalysis. Catal Sci Technol 2012;2:54–75.
[26] Malig J, Jux N, Guldi DM. Toward multifunctional wet chemically functionalized graphene-integration of oligomeric, molecular, and particulate building blocks that reveal photoactivity and redox activity. Acc Chem Res 2013;46:53–64.
[27] Sahoo NG, Pan Y, Li L, Chan SH. Graphene-based materials for energy conversion. Adv Mater 2012;24:4203–10.
[28] Kim K, Choi JY, Kim T, Cho SH, Chung HJ. A role for graphene in silicon-based semiconductor devices. Nature 2011;479:338–44.
[29] Soldano C, Mahmood A, Dujardin E. Production, properties and potential of graphene. Carbon 2010;48:2127–50.
[30] Wei D, Liu Y. Controllable synthesis of graphene and its applications. Adv Mater 2010;22:3225–41.
[31] Zhu Y, Murali S, Cai W, Li X, Suk JW, Potts JR, et al. Graphene and graphene oxide: synthesis, properties, and applications. Adv Mater 2010;22:3906–24.
[32] Chen L, Hernandez Y, Feng X, Mullen K. From nanographene and graphene nanoribbons to graphene sheets: chemical synthesis. Angew Chem Int Ed 2012;51:7640–54.
[33] Chen D, Feng H, Li J. Graphene oxide: preparation, functionalization, and electrochemical applications. Chem Rev 2012;112:6027–53.
[34] Zhu Y, James DK, Tour JM. New routes to graphene, graphene oxide and their related applications. Adv Mater 2012;24:4924–55.
[35] Eda G, Chhowalla M. Chemically derived graphene oxide: towards large-area thin-film electronics and optoelectronics. Adv Mater 2010;22:2392–415.
[36] Rao CNR, Sood AK, Subrahmanyam KS, Govindaraj A. Graphene: the new two-dimensional nanomaterial. Angew Chem Int Ed 2009;48:7752–77.
[37] Luo J, Kim J, Huang J. Material processing of chemically modified graphene: some challenges and solutions. Acc Chem Res 2013;46:2225–34.
[38] Bai S, Shen X. Graphene-inorganic nanocomposites. RSC Adv 2012;2:64–98.
[39] Quintana M, Vazquez E, Prato M. Organic functionalization of graphene in dispersions. Acc Chem Res 2013;46:138–48.
[40] Wang H, Maiyalagan T, Wang X. Review on recent progress in nitrogen-doped graphene: synthesis, characterization, and its potential applications. ACS Catal 2012;2:781–94.
[41] Biro LP, Nemes-Incze P, Lambin P. Graphene: nanoscale processing and recent applications. Nanoscale 2012;4:1824–39.
[42] Luo B, Liu S, Zhi L. Chemical approaches toward graphene-based nanomaterials and their applications in energy-related areas. Small 2012;8:630–46.
[43] Li C, Shi G. Three-dimensional graphene architectures. Nanoscale 2012;4:5549–63.
[44] Bai H, Li C, Shi G. Functional composite materials based on chemically converted graphene. Adv Mater 2011;23:1089–115.
[45] Inagaki M, Kim YA, Endo M. Graphene: preparation and structural perfection. J Mater Chem 2011;21:3280–94.
[46] Zhang Y, Zhang L, Zhou C. Review of chemical vapor deposition of graphene and related applications. Acc Chem Res 2013;46:2329–39.
[47] Kuilla T, Bhadra S, Yao D, Kim NH, Bose S, Lee JH. Recent advances in graphene based polymer composites. Prog Polym Sci 2010;35:1350–75.
[48] Terrones M, Botello-Méndez AR, Campos-Delgado J, López-Urías F, Vega-Cantú YI, Rodríguez-Macías FJ, et al. Graphene and graphite nanoribbons: morphology, properties, synthesis, defects and applications. Nano Today 2010;5:351–72.
[49] Cai M, Thorpe D, Adamson DH, Schniepp HC. Methods of graphite exfoliation. J Mater Chem 2012;22:24992–5002.
[50] Mao S, Pu H, Chen J. Graphene oxide and its reduction: modeling and experimental progress. RSC Adv 2012;2:2643–62.
[51] Dreyer DR, Park S, Bielawski CW, Ruoff RS. The chemistry of graphene oxide. Chem Soc Rev 2010;39:228–40.
[52] Kim J, Cote LJ, Huang J. Two dimensional soft material: new faces of graphene oxide. Acc Chem Res 2012;45:1356–64.
[53] Chu S, Majumdar A. Opportunities and challenges for a sustainable energy future. Nature 2012;288:294–303.
[54] Lackner KS, Brennan S, Matter JM, Park AHA, Wright A, van der Zwaan B. The urgency of the development of CO_2 capture from ambient air. Proc Natl Acad Sci 2012;109:13156–62.
[55] Scott V, Gilfillan S, Markusson N, Chalmers H, Haszeldine RS. Last chance for carbon capture and storage. Nat Clim Change 2013;3:105–11.

[56] Eberle U, Muller B, von Helmolt R. Fuel cell electric vehicles and hydrogen infrastructure: status 2012. Energy Environ Sci 2012;5:8780–98.
[57] Jena P. Materials for hydrogen storage: past, present, and future. J Phys Chem Lett 2011;2:206–11.
[58] Yang J, Sudik A, Wolvertonb C, Siegel DJ. High capacity hydrogen storage materials: attributes for automotive applications and techniques for materials discovery. Chem Soc Rev 2010;39:656–75.
[59] Graetz J. New approaches to hydrogen storage. Chem Soc Rev 2009;38:7–82.
[60] Sahaym U, Norton MG. Advances in the application of nanotechnology in enabling a 'hydrogen economy'. J Mater Sci 2008;43:5395–429.
[61] van den Berg AWC, Arean CO. Materials for hydrogen storage: current research trends and perspectives. Chem Commun 2008:668–81.
[62] Felderhoff M, Weidenthaler C, von Helmolt R, Eberle U. Hydrogen storage: the remaining scientific and technological challenges. Phys Chem Chem Phys 2007;9:2643–53.
[63] Murray LJ, Dinca M, Long JR. Hydrogen storage in metal-organic frameworks. Chem Soc Rev 2009;38:1294–314.
[64] Drage TC, Snape CE, Stevens LA, Wood J, Wang J, Cooper AI, et al. Materials challenges for the development of solid sorbents for post-combustion carbon capture. J Mater Chem 2012;22:2815–23.
[65] Markewitz P, Kuckshinrichs W, Leitner W, Linssen J, Zapp P, Bongartz R, et al. Worldwide innovations in the development of carbon capture technologies and the utilization of CO_2. Energy Environ Sci 2012;5:7281–305.
[66] Zhang X, Zhang X, Dong H, Zhao Z, Zhang S, Huang Y. Carbon capture with ionic liquids: overview and progress. Energy Environ Sci 2012;5:6668–81.
[67] Samanta A, Zhao A, Shimizu GKH, Sarkar P, Gupta R. Post-combustion CO_2 capture using solid sorbents: a review. Ind Eng Chem Res 2012;51:1438–63.
[68] Wang Q, Luo J, Zhong Z, Borgna A. CO_2 capture by solid adsorbents and their applications: current status and new trends. Energy Environ Sci 2011;4:42–55.
[69] Sayari A, Belmabkhout Y, Serna-Guerrero R. Flue gas treatment via CO_2 adsorption. Chem Eng J 2011;171:760–74.
[70] Wang S, Yan S, Ma X, Gong J. Recent advances in capture of carbon dioxide using alkali-metal-based oxides. Energy Environ Sci 2011;4:3805–19.
[71] D'Alessandro DM, Smit B, Long JR. Carbon dioxide capture: prospects for new materials. Angew Chem Int Ed 2010;49:6058–82.
[72] Choi S, Drese JH, Jones CW. Adsorbent materials for carbon dioxide capture from large anthropogenic point sources. ChemSusChem 2009;2:796–854.
[73] Bastos-Neto M, Patzschke C, Lange M, Mollmer J, Moller A, Fichtner S, et al. Assessment of hydrogen storage by physisorption in porous materials. Energy Environ Sci 2012;5:8294–303.
[74] Li JR, Sculley J, Zhou HC. Metal-organic frameworks for separations. Chem Rev 2012;112:869–932.
[75] Sumida K, Rogow DL, Mason JA, McDonald TM, Bloch ED, Herm ZR, et al. Carbon dioxide capture in metal-organic frameworks. Chem Rev 2012;112:724–81.
[76] Dawson R, Cooper AI, Adams DJ. Nanoporous organic polymer networks. Prog Polym Sci 2012;37:530–63.
[77] Vilela F, Zhang K, Antonietti M. Conjugated porous polymers for energy applications. Energy Environ Sci 2012;5:7819–32.
[78] Feng X, Ding X, Jiang D. Covalent organic frameworks. Chem Soc Rev 2012;41:6010–22.
[79] Holst JR, Trewin A, Cooper AI. Porous organic molecules. Nat Chem 2010;2:915–20.
[80] Wang L, Yang RT. Hydrogen storage on carbon-based adsorbents and storage at ambient temperature by hydrogen spillover. Cat Rev: Sci Eng 2010;52:411–61.
[81] Yurum Y, Taralp A, Veziroglu TN. Storage of hydrogen in nanostructured carbon materials. Int J Hydrogen Energy 2009;34:3784–98.
[82] Thomas KM. Adsorption and desorption of hydrogen on metal-organic framework materials for storage applications: comparison with other nanoporous materials. Dalton Trans 2009:1487–505.
[83] http://www1.eere.energy.gov/hydrogenandfuelcells/storage/pdfs/targets_onboard_hydro_storage_explanation.pdf.
[84] http://www1.eere.energy.gov/cleancities/pdfs/ngvtf11_pfeifer.pdf.
[85] http://www.npc.org/FTF_Topic_papers/2Advanced_Storage_Technologies.pdf.
[86] Peng Y, Srinivas G, Wilmer CE, Eryazici I, Snurr RQ, Hupp JT, et al. Simultaneously high gravimetric and volumetric methane uptake characteristics of the metal-organic framework NU-111. Chem Commun 2013;49:2992–4.
[87] Pumera M. Graphene-based nanomaterials for energy storage. Energy Environ Sci 2011;4:668–74.
[88] Lee SY, Park SJ. Comprehensive review on synthesis and adsorption behaviors of graphene-based materials. Carbon Lett 2012;13:73–87.
[89] Lu Y, Feng YP. Adsorptions of hydrogen on graphene and other forms of carbon structures: first principle calculations. Nanoscale 2011;3:2444–53.
[90] Li JR, Kuppler RJ, Zhou HC. Selective gas adsorption and separation in metal-organic frameworks. Chem Soc Rev 2009;38:1477–504.
[91] Yang RT. Adsorbents: fundamentals and applications. Hoboken: John Wiley Sons; 2003.
[92] Zuttel A, Sudan P, Mauron P, Wenger P. Model for the hydrogen adsorption on carbon nanostructures. Appl Phys A 2004;78:941–6.
[93] Deng WQ, Xu X, Goddard WA. New alkali doped pillared carbon materials designed to achieve practical reversible hydrogen storage for transportation. Phys Rev Lett 2004;92:166103.
[94] Patchkovskii S, Tse JS, Yurchenko SN, Zhechkov L, Heine T, Seifert G. Graphene nanostructures as tunable storage media for molecular hydrogen. Proc Natl Acad Sci 2005;102:10439–44.
[95] Aga RS, Fu CL, Krčmar M, Morris JR. Theoretical investigation of the effect of graphite interlayer spacing on hydrogen absorption. Phys Rev B 2007;76:165404.
[96] Arellano JS, Molina LM, Rubio A, Alonso JA. Density functional study of adsorption of molecular hydrogen on graphene layers. J Chem Phys 2000;112:8114–9.
[97] Heine T, Zhechkov L, Seifert G. Hydrogen storage by physisorption on nanostructured graphite platelets. Phys Chem Chem Phys 2004;6:980–4.

[98] Peng L, Morris JR. Prediction of hydrogen adsorption properties in expanded graphite model and in nanoporous carbon. J Phys Chem C 2010;114:15522–9.

[99] Kuc A, Zhechkov L, Patchkovskii S, Seifert G, Heine T. Hydrogen sieving and storage in fullerene intercalated graphite. Nano Lett 2007;7:1–5.

[100] Mpourmpakis G, Tylianakis E, Froudakis GE. Carbon nanoscrolls: a promising material for hydrogen storage. Nano Lett 2007;7:1893–7.

[101] Zhao Y, Kim YH, Simpson LJ, Dillon AC, Wei SH, Heben MJ. Opening space for H$_2$ storage: cointercalation of graphite with lithium and small organic molecules. Phys Rev B 2008;78:144102.

[102] Dimitrakakis GK, Tylianakis E, Froudakis GE. Pillared graphene: a new 3-D network nanostructure for enhanced hydrogen storage. Nano Lett 2008;8:3166–70.

[103] Wu CD, Fang TH, Lo JY. Effects of pressure, temperature, and geometric structure of pillared graphene on hydrogen storage capacity. Int J Hydrogen Energy 2012;37:14211–6.

[104] Lamari FD, Levesque D. Hydrogen adsorption on functionalized graphene. Carbon 2011;49:5196–200.

[105] Kuchta B, Firlej L, Pfeifer P, Wexler C. Numerical estimation of hydrogen storage limits in carbon-based nanospaces. Carbon 2010;48:223–31.

[106] Kuchta B, Firlej L, Cepel R, Pfeifer P, Wexler C. Structural and energetic factors in designing a nanoporous sorbent for hydrogen storage. Colloids Surf A: Physicochem Eng Aspects 2010;357:61–6.

[107] Burress JW, Gadipelli S, Ford J, Simmons JM. Graphene oxide framework materials: theoretical predictions and experimental results. Angew Chem Int Ed 2010;49:8902–4.

[108] Chan Y, Hill JM. Hydrogen storage inside graphene-oxide frameworks. Nanotechnology 2011;22:305403.

[109] Tylianakis E, Psofogiannakis GM, Froudakis GE. Li-doped pillared graphene oxide: a graphene-based nanostructured material for hydrogen storage. J Phys Chem Lett 2010;1:2459–64.

[110] Wang L, Lee K, Sun YY, Lucking M, Chen Z, Zhao JJ, et al. Graphene oxide as an ideal substrate for hydrogen storage. ACS Nano 2009;3:2995–3000.

[111] Park N, Hong S, Kim G, Jhi SH. Computational study of hydrogen storage characteristics of covalent-bonded graphenes. J Am Chem Soc 2007;129:8999–9003.

[112] Kubas J. Metal-dihydrogen and σ-bond coordination: the consummate extension of the Dewar-Chatt-Duncanson model for metal-olefin π bonding. J Organomet Chem 2001;635:37–68.

[113] Ding F, Yakobson BI. Challenges in hydrogen adsorptions: from physisorption to chemisorption. Front Phys 2011;6:142–50.

[114] Bodrenko IV, Avdeenkov AV, Bessarabov DG, Bibikov AV, Nikolaev AV, Taran MD, et al. Hydrogen storage in aromatic carbon ring based molecular materials decorated with alkali or alkali-earth metals. J Phys Chem C 2012;116:25286–92.

[115] Lochan RC, Head-Gordon M. Computational studies of molecular hydrogen binding affinities: the role of dispersion forces, electrostatics, and orbital interactions. Phys Chem Chem Phys 2006;8:1357–70.

[116] Kim G, Jhi SH. Effective metal dispersion in pyridinelike nitrogen doped graphenes for hydrogen storage. Appl Phys Lett 2008;92:013106.

[117] Jhi SH, Kim G, Park N. First-principles studies of metal-dispersed graphene fragments for hydrogen storage. J Kor Phys Soc 2008;52:1217–20.

[118] Liu W, Zhao YH, Nguyen J, Li Y, Jiang Q, Lavernia EJ. Electric field induced reversible switch in hydrogen storage based on single-layer and bilayer graphenes. Carbon 2009;47:3452–60.

[119] Ataca C, Aktürk E, Ciraci S, Ustunel H. High-capacity hydrogen storage by metallized graphene. Appl Phys Lett 2008;93:043123.

[120] Du A, Zhu Z, Smith SC. Multifunctional porous graphene for nanoelectronics and hydrogen storage: new properties revealed by first principle calculations. J Am Chem Soc 2010;132:2876–7.

[121] Durgun E, Ciraci S, Zhou W, Yildirim T. Transition-metal-ethylene complexes as high-capacity hydrogen-storage media. Phys Rev Lett 2006;97:226102.

[122] Zhou W, Zhou J, Shen J, Ouyang C, Shi S. First-principles study of high-capacity hydrogen storage on graphene with Li atoms. J Phys Chem Solids 2012;73:245–51.

[123] Li J, Wang X, Liu K, Sun Y, Chen L. High hydrogen-storage capacity of B-adsorbed graphene: first-principles calculation. Solid State Commun 2012;152:386–9.

[124] Liu Y, Ren L, He Y, Cheng HP. Titanium-decorated graphene for high-capacity hydrogen storage studied by density functional simulations. J Phys: Condens Matter 2010;22:445301.

[125] Li S, Zhao HM, Jena P. Ti-doped nano-porous graphene: a material for hydrogen storage and sensor. Front Phys 2011;6:204–8.

[126] Zhou M, Lu Y, Zhang C, Feng YP. Strain effects on hydrogen storage capability of metal-decorated graphene: a first-principles study. Appl Phys Lett 2010;97:103109.

[127] Tozzini V, Pellegrini V. Reversible hydrogen storage by controlled buckling of graphene layers. J Phys Chem C 2011;115:25523–8.

[128] Zhou YG, Zu XT, Gao F, Nie JL, Xiao HY. Adsorption of hydrogen on boron-doped graphene: a first-principles prediction. J Appl Phys 2009;105:014309.

[129] Firlej L, Kuchta B, Wexler C, Pfeifer P. Boron substituted graphene: energy landscape for hydrogen adsorption. Adsorption 2009;15:312–7.

[130] An H, Liu CS, Zeng Z, Fan C, Ju X. Li-doped B$_2$C graphene as potential hydrogen storage medium. Appl Phys Lett 2011;98:173101.

[131] Liu CS, Zeng Z. Boron-tuned bonding mechanism of Li-graphene complex for reversible hydrogen storage. Appl Phys Lett 2010;96:123101.

[132] Beheshti E, Nojeh A, Servati P. A first-principles study of calcium-decorated, boron-doped graphene for high capacity hydrogen storage. Carbon 2011;49:1561–7.

[133] Park HL, Yi SC, Chung YC. Hydrogen adsorption on Li metal in boron-substituted graphene: an ab initio approach. Int J Hydrogen Energy 2010;35:3583–7.

[134] Park HL, Chung YC. Hydrogen storage in Al and Ti dispersed on graphene with boron substitution: first-principles calculations. Comput Mater Sci 2010;49:S297–301.
[135] Lu R, Rao D, Lu Z, Qian J, Li F, Wu H, et al. Prominently improved hydrogen purification and dispersive metal binding for hydrogen storage by substitutional doping in porous graphene. J Phys Chem C 2012;116:21291–6.
[136] Li D, Ouyang Y, Li J, Sun Y, Chen L. Hydrogen storage of beryllium adsorbed on graphene doping with boron: first-principles calculations. Solid State Commun 2012;152:422–5.
[137] Cho JH, Yang SJ, Lee K, Park CR. Si-doping effect on the enhanced hydrogen storage of single walled carbon nanotubes and graphene. Int J Hydrogen Energy 2011;36:12286–95.
[138] Ataca C, Aktürk E, Ciraci S. Hydrogen storage of calcium atoms adsorbed on graphene: first-principles plane wave calculations. Phys Rev B 2009;79:041406(R).
[139] Yang X, Zhang RQ, Ni J. Stable calcium adsorbates on carbon nanostructures: applications for high-capacity hydrogen storage. Phys Rev B 2009;79:075431.
[140] Kim G, Jhi SH, Lim S, Park N. Crossover between multipole Coulomb and Kubas interactions in hydrogen adsorption on metal-graphene complexes. Phys Rev B 2009;79:155437.
[141] Wang V, Mizuseki H, He HP, Chen G, Zhang SL, Kawazoe Y. Calcium-decorated graphene for hydrogen storage: a van der Waals density functional study. Comput Mater Sci 2012;55:180–5.
[142] Reunchan P, Jhi SH. Metal-dispersed porous graphene for hydrogen storage. Appl Phys Lett 2011;98:093103.
[143] Lee H, Ihm J, Cohen ML, Louie SG. Calcium-decorated graphene-based nanostructures for hydrogen storage. Nano Lett 2010;10:793–8.
[144] Kim G, Jhi SH. Ca-decorated graphene-based three-dimensional structures for high-capacity hydrogen storage. J Phys Chem C 2009;113:20499–503.
[145] Chen C, Zhang J, Zhang B, Duan HM. Hydrogen adsorption of Mg-doped graphene oxide: a first-principles study. J Phys Chem C 2013;117:4337–44.
[146] Ao ZM, Jiang Q, Zhang RQ, Tan TT, Li S. Al doped graphene: a promising material for hydrogen storage at room temperature. J Appl Phys 2009;105:074307.
[147] Ao ZM, Peeters FM. High-capacity hydrogen storage in Al-adsorbed graphene. Phys Rev B 2010;81:205406.
[148] Carrete J, Longo RC, Gallego LJ, Vega A, Balbas LC. Al enhances the H₂ storage capacity of graphene at nanoribbon borders but not at central sites: a study using nonlocal van derWaals density functionals. Phys Rev B 2012;85:125435.
[149] Durgun E, Ciraci S, Yildirim T. Functionalization of carbon-based nanostructures with light transition-metal atoms for hydrogen storage. Phys Rev B 2008;77:085405.
[150] Wu M, Gao Y, Zhang Z, Zeng XC. Edge-decorated graphene nanoribbons by scandium as hydrogen storage media. Nanoscale 2012;4:915–20.
[151] Sigal A, Rojas MI, Leiva EPM. Interferents for hydrogen storage on a graphene sheet decorated with nickel: a DFT study. Int J Hydrogen Energy 2011;36:3537–46.
[152] Hussain T, Pathak B, Ramzan M, Maark TA, Ahuja R. Calcium doped graphane as a hydrogen storage material. Appl Phys Lett 2012;100:183902.
[153] Sluiter MHF, Kawazoe Y. Cluster expansion method for adsorption: application to hydrogen chemisorption on graphene. Phys Rev B 2003;68:085410.
[154] Antipina LY, Avramov PV, Sakai S, Naramoto H, Ohtomo M, Entani S, et al. High hydrogen-adsorption-rate material based on graphane decorated with alkali metals. Phys Rev B 2012;86:085435.
[155] Hussain T, Pathak B, Maark TA, Araujo CM, Scheicher RH, Ahuja R. Ab initio study of lithium-doped graphane for hydrogen storage. EPL 2011;96:27013.
[156] Hussain T, Sarkar AD, Ahuja R. Strain induced lithium functionalized graphane as a high capacity hydrogen storage material. Appl Phys Lett 2012;101:103907.
[157] Miura Y, Kasai H, Dino W, Nakanishi H, Sugimoto T. First principles studies for the dissociative adsorption of H₂ on graphene. J Appl Phys 2003;93:3395–400.
[158] Doi K, Onishi I, Kawano S. Dissociative adsorption of H₂ molecules on steric graphene surface: ab initio MD study based on DFT. Comput Theor Chem 2012;994:54–64.
[159] Liu Z. H⁺ ions on graphene electrode as hydrogen storage reservoirs. Comput Mater Sci 2011;50:3257–64.
[160] Wu HY, Fan X, Kuo JL, Deng WQ. DFT study of hydrogen storage by spillover on graphene with boron substitution. J Phys Chem C 2011;115:9241–9.
[161] Han SS, Jung H, Jung DH, Choi SH, Park N. Stability of hydrogenation states of graphene and conditions for hydrogen spillover. Phys Rev B 2012;85:155408.
[162] Psofogiannakis George M, Froudakis George E. Fundamental studies and perceptions on the spillover mechanism for hydrogen storage. Chem Commun 2011;47:7933–43.
[163] Cabria I, Lopez MJ, Fraile S, Alonso JA. Adsorption and dissociation of molecular hydrogen on palladium clusters supported on graphene. J Phys Chem C 2012;116:21179–89.
[164] Lopez-Corral I, German E, Volpe MA, Brizuela GP, Juan A. Tight-binding study of hydrogen adsorption on palladium decorated graphene and carbon nanotubes. Int J Hydrogen Energy 2010;35:2377–84.
[165] Kayanuma M, Nagashima U, Nishihara H, Kyotani T, Ogawa H. Adsorption and diffusion of atomic hydrogen on a curved surface of microporous carbon: a theoretical study. Chem Phys Lett 2010;495:251–5.
[166] Rangel E, Ramirez-Arellano JM, Carrillo I, Magana LF. Hydrogen adsorption around lithium atoms anchored on graphene vacancies. Int J Hydrogen Energy 2011;36:13657–62.
[167] Lueking AD, Psofogiannakis G, Froudakis GE. Atomic hydrogen diffusion on doped and chemically modified graphene. J Phys Chem C 2013;117:6312–9.
[168] Ao ZM, Peeters FM. Electric field activated hydrogen dissociative adsorption to nitrogen-doped graphene. J Phys Chem C 2010;114:14503–9.
[169] Ao ZM, Hernandez-Nieves AD, Peeters FM, Li S. The electric field as a novel switch for uptake/release of hydrogen for storage in nitrogen doped graphene. Phys Chem Chem Phys 2012;14:1463–7.

[170] Terzyk AP, Furmaniak S, Gauden PA, Kowalczyk P. Fullerene-intercalated graphene nano-containers–mechanism of argon adsorption and high-pressure CH_4 and CO_2 storage capacities. Adsor Sci Technol 2009;27:281–96.
[171] Chen JJ, Li WW, Li XL, Yu HQ. Improving biogas separation and methane storage with multilayer graphene nanostructure via layer spacing optimization and lithium doping: a molecular simulation investigation. Environ Sci Technol 2012;46:10341–8.
[172] Carrillo I, Rangel E, Magana LF. Adsorption of carbon dioxide and methane on graphene with a high titanium coverage. Carbon 2009;47:2752–60.
[173] Wang L, Zhao J, Wang L, Yan T, Sun YY, Zhang SB. Titanium-decorated graphene oxide for carbon monoxide capture and separation. Phys Chem Chem Phys 2011;13:21126–31.
[174] Liu Y, Wilcox J. CO_2 adsorption on carbon models of organic constituents of gas shale and coal. Environ Sci Technol 2011;45:809–14.
[175] Cabrera-Sanfelix P. Adsorption and reactivity of CO_2 on defective graphene sheets. J Phys Chem A 2009;113:493–8.
[176] Shayeganfar F, Neek-Amal M. Methane molecule over the defected and rippled graphene sheet. Solid State Commun 2012;152:1493–6.
[177] Thierfelder C, Witte M, Blankenburg S, Rauls E, Schmidt WG. Methane adsorption on graphene from first principles including dispersion interaction. Surf Sci 2011;605:746–9.
[178] Cazorla C, Shevlin SA, Guo ZX. Calcium-based functionalization of carbon materials for CO_2 capture: a first-principles computational study. J Phys Chem C 2011;115:10990–5.
[179] Ohba T, Kanoh H. Intensive edge effects of nanographenes in molecular adsorptions. J Phys Chem Lett 2012;3:511–6.
[180] Wood BC, Bhide SY, Dutta D, Kandagal VS, Pathak AD, Punnathanam SN, et al. Methane and carbon dioxide adsorption on edge-functionalized graphene: a comparative DFT study. J Chem Phys 2012;137:054702.
[181] Kandagal VS, Pathak A, Ayappa KG, Punnathanam SN. Adsorption on edge-functionalized bilayer graphene nanoribbons: assessing the role of functional groups in methane uptake. J Phys Chem C 2012;116:23394–403.
[182] Katsnelson MI, Fasolino A. Graphene as a prototype crystalline membrane. Acc Chem Res 2013;46:97–105.
[183] Leenaerts O, Partoens B, Peeters FM. Graphene: a perfect nanoballoon. Appl Phys Lett 2008;93:193107.
[184] Miao M, Nardelli MB, Wang Q, Liu Y. First principles study of the permeability of graphene to hydrogen atoms. Phys Chem Chem Phys 2013;15:16132–7.
[185] Tsetseris L, Pantelides ST. Graphene: an impermeable or selectively permeable membrane for atomic species? Carbon 2014;67:58–63.
[186] Jiang D, Cooper VR, Dai S. Porous graphene as the ultimate membrane for gas separation. Nano Lett 2009;9:4019–24.
[187] Liu H, Dai S, Jiang D. Insights into CO_2/N_2 separation through nanoporous graphene from molecular dynamics. Nanoscale 2013;5:9984–7.
[188] Li Y, Zhou Z, Shen P, Chen Z. Two-dimensional polyphenylene: experimentally available porous graphene as a hydrogen purification membrane. Chem Commun 2010;46:3672–4.
[189] Blankenburg S, Bieri M, Fasel R, Müllen K, Pignedoli CA, Passerone D. Porous graphene as an atmospheric nanofilter. Small 2010;6:2266–71.
[190] Qin X, Meng Q, Feng Y, Gao Y. Graphene with line defect as a membrane for gas separation: design via a first-principles modelling. Surf Sci 2013;607:153–8.
[191] Du H, Li J, Zhang J, Su G, Li X, Zhao Y. Separation of hydrogen and nitrogen gases with porous graphene membrane. J Phys Chem C 2011;115:23261–6.
[192] Drahushuk LW, Strano MS. Mechanisms of gas permeation through single layer graphene membranes. Langmuir 2012;28:16671–8.
[193] Tao Y, Xue Q, Liu Z, Shan M, Ling C, Wu T, et al. Tunable hydrogen separation in porous graphene membrane: first-principle and molecular dynamic simulation. ACS Appl Mater Interf 2014;6:8048–58.
[194] Hauser AW, Schwerdtfeger P. Methane-selective nanoporous graphene membranes for gas purification. Phys Chem Chem Phys 2012;14:13292–8.
[195] Shan M, Xue Q, Jing N, Ling C, Zhang T, Yan Z, et al. Influence of chemical functionalization on the CO_2/N_2 separation performance of porous graphene membranes. Nanoscale 2012;4:5477–82.
[196] Schrier J. Fluorinated and nanoporous graphene materials as sorbents for gas separations. ACS Appl Mater Interf 2011;3:4451–8.
[197] Jungthawan S, Reunchan P, Limpijumnong S. Theoretical study of strained porous graphene structures and their gas separation properties. Carbon 2013;54:359–64.
[198] Brunauer S, Emmett PH, Teller E. Adsorption of gases in multimolecular layers. J Am Chem Soc 1938;60:309–19.
[199] Ma LP, Wu ZS, Li J, Wu ED, Ren WC, Cheng HM. Hydrogen adsorption behavior of graphene above critical temperature. Int J Hydrogen Energy 2009;34:2329–32.
[200] Zheng Q, Ji X, Gao S, Wang X. Analysis of adsorption equilibrium of hydrogen on graphene sheets. Int J Hydrogen Energy 2013;38:10896–902.
[201] Srinivas G, Zhu Y, Piner R, Skipper N, Ellerby M, Ruoff R. Synthesis of graphene-like nanosheets and their hydrogen adsorption capacity. Carbon 2010;48:630–5.
[202] Wang Y, Guan C, Wang K, Guo CX, Li CM. Nitrogen, hydrogen, carbon dioxide, and water vapor sorption properties of three-dimensional graphene. J Chem Eng Data 2011;56:642–5.
[203] Yuan W, Li B, Li L. A green synthetic approach to graphene nanosheets for hydrogen adsorption. Appl Surf Sci 2011;257:10183–7.
[204] Lee SY, Park SJ. Isothermal exfoliation of graphene oxide by a new carbon dioxide pressure swing method. Carbon 2014;68:112–7.
[205] Cunning BV, Pyle DS, Merritt CR, Brown CL, Webb CJ, Gray EM. Hydrogen adsorption characteristics of magnesium combustion derived graphene at 77 and 293 K. Int J Hydrogen Energy 2014;39:6783–8.
[206] Ghosh A, Subrahmanyam KS, Krishna KS, Datta S, Govindaraj A, Pati SK, et al. Uptake of H_2 and CO_2 by graphene. J Phys Chem C 2008;112:15704–7.

[207] Subrahmanyam KS, Vivekchand SRC, Govindaraj A, Rao CNR. A study of graphenes prepared by different methods: characterization, properties and solubilisation. J Mater Chem 2008;18:1517–23.

[208] Guo CX, Wang Y, Li CM. Hierarchical graphene-based material for over 4.0 wt.% physisorption hydrogen storage capacity. ACS Sustain Chem Eng 2013;1:14–8.

[209] Asai M, Ohba T, Iwanaga T, Kanoh H, Endo M, Campos-Delgado J, et al. Marked adsorption irreversibility of graphitic nanoribbons for CO_2 and H_2O. J Am Chem Soc 2011;133:14880–3.

[210] Mishra AK, Ramaprabhu S. Carbon dioxide adsorption in graphene sheets. AIP Adv 2011;1:032152.

[211] Meng LY, Park SJ. Effect of exfoliation temperature on carbon dioxide capture of graphene nanoplates. J Colloid Interface Sci 2012;386:285–90.

[212] Zhao Y, Ding H, Zhong Q. Preparation and characterization of aminated graphite oxide for CO_2 capture. Appl Surf Sci 2012;258:4301–7.

[213] Mishra AK, Ramaprabhu S. Nanostructured polyaniline decorated graphene sheets for reversible CO_2 capture. J Mater Chem 2012;22:3708–12.

[214] Enoki T, Suzuki M, Endo M. Graphite intercalation compounds and applications. Oxford: Oxford University Press; 2003.

[215] Wood CR, Skipper NT, Gillan MJ. Ca-intercalated graphite as a hydrogen storage material: stability against decomposition into CaH_2 and graphite. J Solid State Chem 2011;184:1561–5.

[216] Srinivas G, Howard CA, Bennington SM, Skipper NT, Ellerby M. Effect of hydrogenation on structure and superconducting properties of CaC_6. J Mater Chem 2009;19:5239–43.

[217] Srinivas G, Lovell A, Howard CA, Skipper NT, Ellerby M, Bennington SM. Structure and phase stability of hydrogenated first-stage alkali- and alkaline-earth metal-graphite intercalation compounds. Synth Met 2010;160:1631–5.

[218] Purewal JJ, Keith JB, Ahn CC, Fultz B, Brown CM, Tyagi M. Adsorption and melting of hydrogen in potassium-intercalated graphite. Phys Rev B 2009;79:054305.

[219] Lovell A, Fernandez-Alonso F, Skipper NT, Refson K, Bennington SM, Parker SF. Quantum delocalization of molecular hydrogen in alkali-graphite intercalates. Phys Rev Lett 2008;101:126101.

[220] Lueking AD, Pan L, Narayanan DL, Clifford CEB. Effect of expanded graphite lattice in exfoliated graphite nanofibers on hydrogen storage. J Phys Chem B 2005;109:12710–7.

[221] Kim BH, Hong WG, Moon HR, Lee SM, Kim JM, Kang S, et al. Investigation on the existence of optimum interlayer distance for H_2 uptake using pillared-graphene oxide. Int J Hydrogen Energy 2012;37:14217–22.

[222] Kim BH, Hong WG, Yu HY, Han YK, Lee SM, Chang SJ, et al. Thermally modulated multilayered graphene oxide for hydrogen storage. Phys Chem Chem Phys 2012;14:1480–5.

[223] Hong WG, Kim BH, Lee SM, Yu HY, Yun YJ, Jun Y, et al. Agent-free synthesis of graphene oxide/transition metal oxide composites and its application for hydrogen storage. Int J Hydrogen Energy 2012;37:7594–9.

[224] Ding Z, Qing L, Yi CQ, Chao ZY, Yi C, Tao W, et al. Graphene-manganese oxide hybrid porous material and its application in carbon dioxide adsorption. Chin Sci Bull 2012;57:3059–64.

[225] Zhou D, Zhang TL, Han BH. One-step solvothermal synthesis of an iron oxide-graphene magnetic hybrid material with high porosity. Microporous Mesoporous Mater 2013;165:234–9.

[226] Zhou D, Han BH. Graphene-based nanoporous materials assembled by mediation of polyoxometalate nanoparticles. Adv Funct Mater 2010;20:2717–22.

[227] Srinivas G, Burress JW, Ford J, Yildirim T. Porous graphene oxide frameworks: synthesis and gas sorption properties. J Mater Chem 2011;21:11323–9.

[228] Severin K. Boronic acids as building blocks for molecular nanostructures and polymeric materials. Dalton Trans 2009:5254–64.

[229] Jin Z, Lu W, O'Neill KJ, Parilla PA, Simpson LJ, Kittrell C, et al. Nano-engineered spacing in graphene sheets for hydrogen storage. Chem Mater 2011;23:923–5.

[230] Zhou D, Cheng QY, Cui Y, Wang T, Li X, Han BH. Graphene–terpyridine complex hybrid porous material for carbon dioxide adsorption. Carbon 2014;66:592–8.

[231] Alhwaige AA, Agag T, Ishida H, Qutubuddin S. Biobased chitosan hybrid aerogels with superior adsorption: role of graphene oxide in CO_2 capture. RSC Adv 2013;3:16011–20.

[232] Tsoufis T, Katsaros F, Sideratou Z, Romanos G, Ivashenko O, Rudolf P, et al. Tailor-made graphite oxide–DAB poly(propylene imine) dendrimer intercalated hybrids and their potential for efficient CO_2 adsorption. Chem Commun 2014;50:10967–70.

[233] Matsuo Y, Ueda S, Konishi K, Marco-Lozar JP, Lozano-Castello D, Cazorla-Amoros D. Pillared carbons consisting of silsesquioxane bridged graphene layers for hydrogen storage materials. Int J Hydrogen Energy 2012;37:10702–8.

[234] Aboutalebi SH, Aminorroaya-Yamini S, Nevirkovets I, Konstantinov K, Liu HK. Enhanced hydrogen storage in graphene oxide-MWCNTs composite at room temperature. Adv Energy Mater 2012;2:1439–46.

[235] Ruiz-García C, Pérez-Carvajal J, Berenguer-Murcia A, Darder M, Aranda P, Cazorla-Amorós D, et al. Clay-supported graphene materials: application to hydrogen storage. Phys Chem Chem Phys 2013;15:18635–41.

[236] Ruiz-García C, Jiménez R, Pérez-Carvajal J, Berenguer-Murcia A, Darder M, Aranda P, et al. Graphene-clay based nanomaterials for clean energy storage. Sci Adv Mater 2014;6:151–8.

[237] Petit C, Burress J, Bandosz TJ. The synthesis and characterization of copper-based metal-organic framework/graphite oxide composites. Carbon 2011;49:563–72.

[238] Liu S, Sun L, Xu F, Zhang J, Jiao C, Li F, et al. Nanosized Cu-MOFs induced by graphene oxide and enhanced gas storage capacity. Energy Environ Sci 2013;6:818–23.

[239] Huang W, Zhou X, Xia Q, Peng J, Wang H, Li Z. Preparation and adsorption performance of GrO@Cu-BTC for separation of CO_2/CH_4. Ind Eng Chem Res 2014;53:11176–84.

[240] Zhao Y, Seredych M, Zhong Q, Bandosz TJ. Aminated graphite oxides and their composites with copper-based metal–organic framework: in search for efficient media for CO_2 sequestration. RSC Adv 2013;3:9932–41.

[241] Yang S, Zhan L, Xu X, Wang Y, Ling L, Feng X. Graphene-based porous silica sheets impregnated with polyethyleneimine for superior CO_2 capture. Adv Mater 2013;25:2130–4.

[242] Sui ZY, Cui Y, Zhu JH, Han BH. Preparation of three-dimensional graphene oxide-polyethylenimine porous materials as dye and gas adsorbents. ACS Appl Mater Interf 2013;5:9172–9.

[243] Prins R. Hydrogen spillover: facts and fiction. Chem Rev 2012;112:2714–38.

[244] Hu ZL, Aizawa M, Wang ZM, Yoshizawa N, Hatori H. Synthesis and characteristics of graphene oxide-derived carbon nanosheet-Pd nanosized particle composites. Langmuir 2010;26:6681–8.

[245] Srinivas G, Sankaranarayanana V, Ramaprabhu S. Influence of hydrogen absorption–desorption on structural properties of $Dy_{1-x}Mm_xCo_2$ alloys. J Phys: Condens Matter 2008;20:255224.

[246] Srinivas G, Sankaranarayanana V, Ramaprabhu S. Thermodynamic and hydrogen-induced structural properties of $Ho_{1-x}Mm_xCo_2$-hydrides. J Phys D: Appl Phys 2007;40:1183–9.

[247] Huang CC, Pu NW, Wang CA, Huang JC, Sung Y, Ger MD. Hydrogen storage in graphene decorated with Pd and Pt nano-particles using an electroless deposition technique. Sep Purif Technol 2011;82:210–5.

[248] Chen CH, Chung TY, Shen CC, Yu MS, Tsao CS, Shi GN, et al. Hydrogen storage performance in palladium-doped graphene/carbon composites. Int J Hydrogen Energy 2013;38:3681–8.

[249] Parambhath VB, Nagar R, Sethupathi K, Ramaprabhu S. Investigation of spillover mechanism in palladium decorated hydrogen exfoliated functionalized graphene. J Phys Chem C 2011;115:15679–85.

[250] Parambhath VB, Nagar R, Ramaprabhu S. Effect of nitrogen doping on hydrogen storage capacity of palladium decorated graphene. Langmuir 2012;28:7826–33.

[251] Vinayan BP, Sethupathi K, Ramaprabhu S. Facile synthesis of triangular shaped palladium nanoparticles decorated nitrogen doped graphene and their catalytic study for renewable energy applications. Int J Hydrogen Energy 2013;38:2240–50.

[252] Vinayan BP, Nagar R, Ramaprabhu S. Solar light assisted green synthesis of palladium nanoparticle decorated nitrogen doped graphene for hydrogen storage application. J Mater Chem A 2013;1:11192–9.

[253] Wang Y, Liu J, Wang K, Chen T, Tan X, Li CM. Hydrogen storage in NiB nanoalloy-doped 2D graphene. Int J Hydrogen Energy 2011;36:12950–4.

[254] Wang Y, Guo CX, Wang X, Guan C, Yang H, Wang K, et al. Hydrogen storage in a Ni-B nanoalloy-doped three-dimensional graphene material. Energy Environ Sci 2011;4:195–200.

[255] Bourlinos AB, Steriotis TA, Karakassides M, Sanakis Y, Tzitzios V, Trapalis C, et al. Synthesis, characterization and gas sorption properties of a molecularly-derived graphite oxide-like foam. Carbon 2007;45:852–7.

[256] Psofogiannakis GM, Steriotis TA, Bourlinos AB, Kouvelos EP, Charalambopoulou GC, Stubos AK, et al. Enhanced hydrogen storage by spillover on metal-doped carbon foam: an experimental and computational study. Nanoscale 2011;3:933–6.

[257] Wang L, Yang FH, Yang RT, Miller MA. Effect of surface oxygen groups in carbons on hydrogen storage by spillover. Ind Eng Chem Res 2009;48:2920–6.

[258] Wu HC, Li YY, Sakoda A. Synthesis and hydrogen storage capacity of exfoliated turbostratic carbon nanofibers. Int J Hydrogen Energy 2010;35:4123–30.

[259] Choucair M, Thordarson P, Stride JA. Gram-scale production of graphene based on solvothermal synthesis and sonication. Nat Nanotechnol 2009;4:30–3.

[260] Deng D, Pan X, Yu L, Cui Y, Jiang Y, Qi J, et al. Toward N-doped graphene via solvothermal synthesis. Chem Mater 2011;23:1188–93.

[261] Wang L, Stuckert NR, Yang RT. Unique hydrogen adsorption properties of graphene. AIChE 2011;57:2902–8.

[262] Jin Z, Sun Z, Simpson LJ, O'Neill KJ, Parilla PA, Li Y, et al. Solution-phase synthesis of heteroatom-substituted carbon scaffolds for hydrogen storage. J Am Chem Soc 2010;132:15246–51.

[263] Srinivas G, Burress J, Yildirim T. Graphene oxide derived carbons (GODCs): synthesis and gas adsorption properties. Energy Environ Sci 2012;5:6453–9.

[264] Chandra V, Yu SU, Kim SH, Yoon YS, Kim DY, Kwon AH, et al. Highly selective CO_2 capture on N-doped carbon produced by chemical activation of polypyrrole functionalized graphene sheets. Chem Commun 2012;48:735–7.

[265] Kemp KC, Chandra V, Saleh M, Kim KS. Reversible CO_2 adsorption by an activated nitrogen doped graphene/polyaniline material. Nanotechnology 2013;24:235703.

[266] Seema H, Kemp KC, Le NH, Park SW, Chandra V, Lee JW, et al. Highly selective CO_2 capture by S-doped microporous carbon materials. Carbon 2014;66:320–6.

[267] Ning G, Xu C, Mu L, Chen G, Wang G, Gao J, et al. High capacity gas storage in corrugated porous graphene with a specific surface area-lossless tightly stacking manner. Chem Commun 2012;48:6815–7.

[268] Guo GF, Huang H, Xue FH, Liu CJ, Yu HT, Quan X, et al. Electrochemical hydrogen storage of the graphene sheets prepared by DC arc-discharge method. Surf Coat Technol 2013;228:S120–5.

[269] Chen Y, Wang Q, Zhu C, Gao P, Ouyang Q, Wang T, et al. Graphene/porous cobalt nanocomposite and its noticeable electrochemical hydrogen storage ability at room temperature. J Mater Chem 2012;22:5924–7.

[270] Gao P, Wang Y, Yang S, Chen Y, Xue Z, Wang L, et al. Mechanical alloying preparation of fullerene-like Co_3C nanoparticles with high hydrogen storage ability. Int J Hydrogen Energy 2012;37:17126–30.

[271] Subrahmanyam KS, Kumar P, Maitra U, Govindaraj A, Hembram KPSS, Waghmare UV, et al. Chemical storage of hydrogen in few-layer graphene. Proc Natl Acad Sci 2011;108:2674–7.

[272] Pekker S, Salvetat JP, Jakab E, Bonard JM, Forro L. Hydrogenation of carbon nanotubes and graphite in liquid ammonia. J Phys Chem B 2001;105:7938–43.

[273] Yang Z, Sun Y, Alemany LB, Narayanan TN, Billups WE. Birch reduction of graphite. Edge and interior functionalization by hydrogen. J Am Chem Soc 2012;134:18689–94.

[274] Elias DC, Nair RR, Mohiuddin TMG, Morozov SV, Blake P, Halsall MP, et al. Control of graphene's properties by reversible hydrogenation: evidence of graphane. Science 2009;323:610–3.

[275] Krishna R, Titus E, Costa LC, Menezes JCJMDS, Correia MRP, Pinto S, et al. Facile synthesis of hydrogenated reduced graphene oxide via hydrogen spillover mechanism. J Mater Chem 2012;22:10457–9.

[276] Poh HL, Sanek F, Sofer Z, Pumera M. High-pressure hydrogenation of graphene: towards graphane. Nanoscale 2012;4:7006–11.

[277] Johns JE, Hersam MC. Atomic covalent functionalization of graphene. Acc Chem Res 2013;46:77–86.

[278] Chen DM, Ichikawa T, Fujii H, Ogita N, Udagawa M, Kitano Y, et al. Unusual hydrogen absorption properties in graphite mechanically milled under various hydrogen pressures up to 6 MPa. J Alloys Compd 2003;354:L5–9.

[279] Orimo S, Matsushima T, Fujii H, Fukunaga T, Majer G. Hydrogen desorption property of mechanically prepared nanostructured graphite. J Appl Phys 2001;90:1545–9.

[280] Orimo S, Majer G, Fukunaga T, Zuttel A, Schlapbach L, Fujii H. Hydrogen in the mechanically prepared nanostructured graphite. Appl Phys Lett 1999;75:3093–5.

[281] Jeon I-Y, Choi H-J, Jung S-M, Seo J-M, Kim M-J, Dai L, et al. Large-scale production of edge-selectively functionalized graphene nanoplatelets via ball milling and their use as metal-free electrocatalysts for oxygen reduction reaction. J Am Chem Soc 2013;135:1386–93.

[282] Bunch JS, Verbridge SS, Alden JS, van der Zande AM, Parpia JM, Craighead HG, et al. Impermeable atomic membranes from graphene sheets. Nano Lett 2008;8:2458–62.

[283] Koenig SP, Wang L, Pellegrino J, Bunch JS. Selective molecular sieving through porous graphene. Nat Nanotechnol 2012;7:728–32.

[284] Nair RR, Wu HA, Jayaram PN, Grigorieva IV, Geim AK. Unimpeded permeation of water through helium-leak–tight graphene-based membranes. Science 2012;335:442–4.

[285] O'Hern SC, Stewart CA, Boutilier MSH, Idrobo JC, Bhaviripudi S, Das SK, et al. Selective molecular transport through intrinsic defects in a single layer of CVD graphene. ACS Nano 2012;6:10130–8.

[286] Cohen-Tanugi D, Grossman JC. Water desalination across nanoporous graphene. Nano Lett 2012;12:3602–8.

[287] Sutter E, Albrecht P, Camino FE, Sutter P. Monolayer graphene as ultimate chemical passivation layer for arbitrarily shaped metal surfaces. Carbon 2010;48:4414–20.

[288] Chen S, Brown L, Levendorf M, Cai W, Ju SY, Edgeworth J, et al. Oxidation resistance of graphene-coated Cu and Cu/Ni alloy. ACS Nano 2011;5:1321–7.

[289] Gadipelli S, Calizo I, Ford J, Cheng G, Walker ARH, Yildirim T. A highly practical route for large-area, single layer graphene from liquid carbon sources such as benzene and methanol. J Mater Chem 2011;21:16057–65.

[290] Kang D, Kwon JY, Cho H, Sim JH, Hwang HS, Kim CS, et al. Oxidation resistance of iron and copper foils coated with reduced graphene oxide multilayers. ACS Nano 2012;6:7763–9.

[291] Nilsson L, Andersen M, Balog R, Lægsgaard E, Hofmann P, Besenbacher F, et al. Graphene coatings: probing the limits of the one atom thick protection layer. ACS Nano 2012;6:10258–66.

[292] Kim H, Macosko CW. Morphology and properties of polyester/exfoliated graphite nanocomposites. Macromolecules 2008;41:3317–27.

[293] Kim H, Miura Y, Macosko CW. Graphene/polyurethane nanocomposites for improved gas barrier and electrical conductivity. Chem Mater 2010;22:3441–50.

[294] Liu H, Kuila T, Kim NH, Ku BC, Lee JH. In situ synthesis of the reduced graphene oxide-polyethyleneimine composite and its gas barrier properties. J Mater Chem A 2013;1:3739–46.

[295] Yang Y-H, Bolling L, Priolo MA, Grunlan JC. Super gas barrier and selectivity of graphene oxide-polymer multilayer thin films. Adv Mater 2013;25:503–8.

[296] Yang J, Bai L, Feng G, Yang X, Lv M, Zhang C, et al. Thermal reduced graphene based poly(ethylene vinyl alcohol) nanocomposites: enhanced mechanical properties, gas barrier, water resistance, and thermal stability. Ind Eng Chem Res 2013;52:16745–54.

[297] Kim HW, Yoon HW, Yoon SM, Yoo BM, Ahn BK, Cho YH, et al. Selective gas transport through few-layered graphene and graphene oxide membranes. Science 2013;342:91–5.

[298] Li H, Song Z, Zhang X, Huang Y, Li S, Mao Y, et al. Ultrathin, molecular-sieving graphene oxide membranes for selective hydrogen separation. Science 2013;342:95–8.

[299] Tang S, Cao Z. Adsorption of nitrogen oxides on graphene and graphene oxides: insights from density functional calculations. J Chem Phys 2011;134:044710.

[300] Tang S, Cao Z. Adsorption and dissociation of ammonia on graphene oxides: a first-principles study. J Phys Chem C 2012;116:8778–91.

[301] Ganji MD, Sharifi N, Ardjmand M, Ahangari MG. Pt-decorated graphene as superior media for H_2S adsorption: a first-principles study. Appl Surf Sci 2012;261:697–704.

[302] Chen C, Xu K, Ji X, Miao L, Jiang J. Enhanced adsorption of acidic gases (CO_2, NO_2 and SO_2) on light metal decorated graphene oxide. Phys Chem Chem Phys 2014;16:11031–6.

[303] Slabaugh WH, Seiler BC. Interactions of ammonia with graphite oxide. J Phys Chem 1962;66:396–401.

[304] Nguyen-Thanh D, Block K, Bandosz TJ. Adsorption of hydrogen sulfide on montmorillonites modified with iron. Chemosphere 2005;59:343–53.

[305] Petit C, Seredych M, Bandosz TJ. Revisiting the chemistry of graphite oxides and its effect on ammonia adsorption. J Mater Chem 2009;19:9176–85.

[306] Seredych M, Petit C, Tamashausky AV, Bandosz TJ. Role of graphite precursor in the performance of graphite oxides as ammonia adsorbents. Carbon 2009;47:445–56.

[307] Seredych M, Bandosz TJ. Combined role of water and surface chemistry in reactive adsorption of ammonia on graphite oxides. Langmuir 2010;26:5491–8.

[308] Seredych M, Rossin JA, Bandosz TJ. Changes in graphite oxide texture and chemistry upon oxidation and reduction and their effect on adsorption of ammonia. Carbon 2011;49:4392–402.

[309] Bandosz TJ. Towards understanding reactive adsorption of small molecule toxic gases on carbonaceous materials. Cat Today 2012;186:20–8.

[310] Seredych M, Bandosz TJ. Graphite oxide/AlZr polycation composites: surface characterization and performance as adsorbents of ammonia. Mater Chem Phys 2009;117:99–106.

[311] Petit C, Bandosz TJ. Graphite oxide/polyoxometalate nanocomposites as adsorbents of ammonia. J Phys Chem C 2009;113:3800–9.

[312] Seredych M, Tamashausky AV, Bandosz TJ. Surface features of exfoliated graphite/bentonite composites and their importance for ammonia adsorption. Carbon 2008;46:1241–52.

[313] Seredych M, Bandosz TJ. Manganese oxide and graphite oxide/MnO$_2$ composites as reactive adsorbents of ammonia at ambient conditions. Microporous Mesoporous Mater 2012;150:55–63.
[314] Seredych M, Bandosz TJ. Adsorption of hydrogen sulfide on graphite derived materials modified by incorporation of nitrogen. Mater Chem Phys 2009;113:946–52.
[315] Seredych M, Mabayoje O, Bandosz TJ. Interactions of NO$_2$ with zinc (hydr)oxide/graphene phase composites: visible light enhanced surface reactivity. J Phys Chem C 2012;116:2527–35.
[316] Seredych M, Mabayoje O, Bandosz TJ. Visible-light-enhanced interactions of hydrogen sulfide with composites of zinc (oxy)hydroxide with graphite oxide and graphene. Langmuir 2012;28:1337–46.
[317] Seredych M, Bandosz TJ. Effects of surface features on adsorption of SO$_2$ on graphite oxide/Zr(OH)$_4$ composites. J Phys Chem C 2010;114:14552–60.
[318] Seredych M, Bandosz TJ. Reactive adsorption of hydrogen sulfide on graphite oxide/Zr(OH)$_4$ composites. Chem Eng J 2011;166:1032–8.
[319] Mabayoje O, Seredych M, Bandosz TJ. Cobalt (hydr)oxide/graphite oxide composites: importance of surface chemical heterogeneity for reactive adsorption of hydrogen sulphide. J Colloid Interface Sci 2012;378:1–9.
[320] Mabayoje O, Seredych M, Bandosz TJ. Enhanced reactive adsorption of hydrogen sulfide on the composites of graphene/graphite oxide with copper (hydr)oxychlorides. ACS Appl Mater Interf 2012;4:3316–24.
[321] Bashkova S, Bandosz TJ. Adsorption/reduction of NO$_2$ on graphite oxide/iron composites. Ind Eng Chem Res 2009;48:10884–91.
[322] Seredych M, Pietrzak R, Bandosz TJ. Role of graphite oxide (GO) and polyaniline (PANI) in NO$_2$ reduction on GO-PANI composites. Ind Eng Chem Res 2007;46:6925–35.
[323] Petit C, Bandosz TJ. Exploring the coordination chemistry of MOF–graphite oxide composites and their applications as adsorbents. Dalton Trans 2012;41:4027–35.
[324] Petit C, Bandosz TJ. Synthesis, characterization, and ammonia adsorption properties of mesoporous metal-organic framework (MIL(Fe))-graphite oxide composites: exploring the limits of materials fabrication. Adv Funct Mater 2011;21:2108–17.
[325] Petit C, Wrabetz S, Bandosz TJ. Microcalorimetric insight into the analysis of the reactive adsorption of ammonia on Cu-MOF and its composite with graphite oxide. J Mater Chem 2012;22:21443–7.
[326] Petit C, Levasseur B, Mendoza B, Bandosz TJ. Reactive adsorption of acidic gases on MOF/graphite oxide composites. Microporous Mesoporous Mater 2012;154:107–12.
[327] Bandosz TJ, Petit C. MOF/graphite oxide hybrid materials: exploring the new concept of adsorbents and catalysts. Adsorption 2011;17:5–16.
[328] Morishige K, Hamada T. Iron oxide pillared graphite. Langmuir 2005;21:6277–81.
[329] Huang ZH, Liu G, Kang F. Glucose-promoted Zn-based metal-organic framework/graphene oxide composites for hydrogen sulfide removal. ACS Appl Mater Interf 2012;4:4942–7.
[330] Long Y, Zhang C, Wang X, Gao J, Wang W, Liu Y. Oxidation of SO$_2$ to SO$_3$ catalyzed by graphene oxide foams. J Mater Chem 2011;21:13934–41.
[331] Nijkamp MG, Raaymakers JEMJ, van Dillen AJ, de Jong KP. Hydrogen storage using physisorption-materials demands. Appl Phys A 2001;72:619–23.
[332] Zhao W, Fierro V, Zlotea C, Aylon E, Izquierdo MT, Latroche M, et al. Activated carbons with appropriate micropore size distribution for hydrogen adsorption. Int J Hydrogen Energy 2011;36:5431–4.
[333] Texier-Mandoki N, Dentzer J, Piquero T, Saadallah S, David P, Vix-Guterl C. Hydrogen storage in activated carbon materials: role of the nanoporous texture. Carbon 2004;42:2744–7.
[334] Liu F, Seo TS. A controllable self-assembly method for large-scale synthesis of graphene sponges and free-standing graphene films. Adv Funct Mater 2010;20:1930–6.
[335] Niu Z, Chen J, Hng HH, Ma J, Chen X. A leavening strategy to prepare reduced graphene oxide foams. Adv Mater 2012;24:4144–50.
[336] Worsley MA, Jonathan TYO, Lee RI, Willey TM, Nielsen MH, Roberts SK, et al. High surface area, sp^2-cross-linked three-dimensional graphene monoliths. J Phys Chem Lett 2011;2:921–5.
[337] Worsley MA, Kucheyev SO, Mason HE, Merrill MD, Mayer BP, Lewicki J, et al. Mechanically robust 3D graphene macroassembly with high surface area. Chem Commun 2012;48:8428–30.
[338] Zhang K, Ang BT, Zhang LL, Zhao XS, Wu J. Pyrolyzed graphene oxide/resorcinol-formaldehyde resin composites as high-performance supercapacitor electrodes. J Mater Chem 2011;21:2663–70.
[339] Biener J, Dasgupta S, Shao L, Wang D, Worsley MA, Wittstock A, et al. Macroscopic 3D nanographene with dynamically tunable bulk properties. Adv Mater 2012;24:5083–7.
[340] Lei Z, Christov N, Zhao XS. Intercalation of mesoporous carbon spheres between reduced graphene oxide sheets for preparing high-rate supercapacitor electrodes. Energy Environ Sci 2011;4:1866–73.
[341] Huang X, Qian K, Yang J, Zhang J, Li L, Yu C, et al. Functional nanoporous graphene foams with controlled pore sizes. Adv Mater 2012;24:4419–23.
[342] Zhang L, Yang X, Zhang F, Long G, Zhang T, Leng K, et al. Controlling the effective surface area and pore size distribution of sp^2 carbon materials and their impact on the capacitance performance of these materials. J Am Chem Soc 2013;135:5921–9.
[343] Guardia L, Suárez-García F, Paredes JI, Solís-Fernández P, Rozada R, Fernández-Merino MJ, et al. Synthesis and characterization of graphene–mesoporous silica nanoparticle hybrids. Microporous Mesoporous Mater 2012;160:18–24.
[344] Yang S, Zhi L, Tang K, Feng X, Maier J, Müllen K. Efficient synthesis of heteroatom (N or S)-doped graphene based on ultrathin graphene oxide-porous silica sheets for oxygen reduction reactions. Adv Funct Mater 2012;22:3634–40.
[345] Yavari F, Chen Z, Thomas AV, Ren W, Cheng HM, Koratkar N. High sensitivity gas detection using a macroscopic three-dimensional graphene foam network. Sci Rep 2011;1:166.
[346] Shan C, Tang H, Wong T, He L, Lee ST. Facile synthesis of a large quantity of graphene by chemical vapor deposition: an advanced catalyst carrier. Adv Mater 2012;24:2491–5.

[347] Wen Z, Wang X, Mao S, Bo Z, Kim H, Cui S, et al. Crumpled nitrogen-doped graphene nanosheets with ultrahigh pore volume for high-performance supercapacitor. Adv Mater 2012;24:5610–6.

[348] Lin TW, Su CY, Zhang XQ, Zhang W, Lee YH, Chu CW, et al. Converting graphene oxide monolayers into boron carbonitride nanosheets by substitutional doping. Small 2012;8:1384–91.

[349] Lin Z, Waller G, Liu Y, Liu M, Wong CP. Facile synthesis of nitrogen-doped graphene via pyrolysis of graphene oxide and urea, and its electrocatalytic activity toward the oxygen-reduction reaction. Adv Energy Mater 2012;2:884–8.

[350] Guo J, Morris JR, Ihm Y, Contescu CI, Gallego NC, Duscher G, et al. Topological defects: origin of nanopores and enhanced adsorption performance in nanoporous carbon. Small 2012;8:3283–8.

[351] Zhu X, Ning G, Fan Z, Gao J, Xu C, Qian W, et al. One-step synthesis of a graphene-carbon nanotube hybrid decorated by magnetic nanoparticles. Carbon 2012;50:2764–71.

[352] Seredych M, Chen R, Bandosz TJ. Effects of the addition of graphite oxide to the precursor of a nanoporous carbon on the electrochemical performance of the resulting carbonaceous composites. Carbon 2012;50:4144–54.

[353] Zhang D, Wen X, Shi L, Yan T, Zhang J. Enhanced capacitive deionization of graphene/mesoporous carbon composites. Nanoscale 2012;4:5440–6.

[354] Wang L, Sun L, Tian C, Tan T, Mu G, Zhang H, et al. A novel soft template strategy to fabricate mesoporous carbon/graphene composites as high-performance supercapacitor electrodes. RSC Adv 2012;2:8359–67.

[355] Hu C, Zhao Y, Cheng H, Hu Y, Shi G, Dai L, et al. Ternary $Pd_2/PtFe$ networks supported by 3D graphene for efficient and durable electrooxidation of formic acid. Chem Commun 2012;48:11865–7.

[356] Sridhar V, Kim HJ, Jung JH, Lee C, Park S, Oh IK. Defect-engineered three-dimensional graphene-nanotube-palladium nanostructures with ultrahigh capacitance. ACS Nano 2012;6:10562–70.

[357] Zhong M, Natesakhawat S, Baltrus JP, Luebke D, Nulwala H, Matyjaszewski K, et al. Copolymer-templated nitrogen-enriched porous nanocarbons for CO_2 capture. Chem Commun 2012;48:11516–8.

[358] Kumar N, Subrahmanyam KS, Chaturbedy P, Raidongia K, Govindaraj A, Hembram K, et al. Remarkable uptake of CO_2 and CH_4 by graphene-like borocarbonitrides, $B_xC_yN_z$. ChemSusChem 2011;4:1662–70.

[359] Lai L, Chen L, Zhan D, Sun L, Liu J, Lim SH, et al. One-step synthesis of NH_2-graphene from in situ graphene-oxide reduction and its improved electrochemical properties. Carbon 2011;49:3250–7.

[360] Liang J, Jiao Y, Jaroniec M, Qiao SZ. Sulfur and nitrogen dual-doped mesoporous graphene electrocatalyst for oxygen reduction with synergistically enhanced performance. Angew Chem Int Ed 2012;51:11496–500.

[361] Fechler N, Fellinger TP, Antonietti M. "Salt templating": a simple and sustainable pathway toward highly porous functional carbons from ionic liquids. Adv Mater 2013;25:75–9.

[362] Li Y, Fu ZY, Su BL. Hierarchically structured porous materials for energy conversion and storage. Adv Funct Mater 2012;22:4634–67.

[363] Li X-H, Antonietti M. Polycondensation of boron- and nitrogen-codoped holey graphene monoliths from molecules: carbocatalysts for selective oxidation. Angew Chem Int Ed 2013;52:4572–6.

[364] Weng Q, Wang X, Zhi C, Bando Y, Golberg D. Boron nitride porous microbelts for hydrogen storage. ACS Nano 2013;7:1558–65.

[365] Li Y, Li Z, Shen PK. Simultaneous formation of ultrahigh surface area and three-dimensional hierarchical porous graphene-like networks for fast and highly stable supercapacitors. Adv Mater 2013;25:2474–80.

[366] Zhang L, Zhang F, Yang X, Long G, Wu Y, Zhang T, et al. Porous 3D graphene-based bulk materials with exceptional high surface area and excellent conductivity for supercapacitors. Sci Rep 2013;3:1408.

[367] Shen W, Fan W. Nitrogen-containing porous carbons: synthesis and application. J Mater Chem A 2013;1:999–1013.

[368] Li J, Lin J, Xu X, Zhang X, Xue Y, Mi J, et al. Porous boron nitride with a high surface area: hydrogen storage and water treatment. Nanotechnology 2013;24:155603.

[369] Masika E, Mokaya R. Exceptional gravimetric and volumetric hydrogen storage for densified zeolite templated carbons with high mechanical stability. Energy Environ Sci 2014;7:427–34.

[370] Yang SJ, Kim T, Im JH, Kim YS, Lee K, Jung H, et al. MOF-derived hierarchically porous carbon with exceptional porosity and hydrogen storage capacity. Chem Mater 2012;24:464–70.

[371] Jiang HL, Liu B, Lan YQ, Kuratani K, Akita T, Shioyama H, et al. From metal-organic framework to nanoporous carbon: toward a very high surface area and hydrogen uptake. J Am Chem Soc 2011;133:11854–7.

[372] Srinivas G, Krungleviciute V, Guo ZX, Yildirim T. Exceptional CO_2 capture in a hierarchically porous carbon with simultaneous high surface area and pore volume. Energy Environ Sci 2014;7:335–42.

[373] Lee HJ, Choi S, Oh M. Well-dispersed hollow porous carbon spheres synthesized by direct pyrolysis of core-shell type metal-organic frameworks and their sorption properties. Chem Commun 2014;50:4492–5.

[374] Li Y, Ben T, Zhang B, Fu Y, Qiu S. Ultrahigh gas storage both at low and high pressures in KOH-activated carbonized porous aromatic frameworks. Sci Rep 2013;2:2420.

[375] Wang Q, Xia W, Guo W, An L, Xia D, Zou R. Functional zeolitic-imidazolate-framework-templated porous carbon materials for CO_2 capture and enhanced capacitors. Chem Asian J 2013;8:1879–85.

[376] Hu K, Gupta MK, Kulkarni DD, Tsukruk VV. Ultra-robust graphene oxide-silk fibroin nanocomposite membranes. Adv Mater 2013;25:2301–7.

[377] Ou X, Chen P, Jiang L, Shen Y, Hu W, Liu M. Π-conjugated molecules crosslinked graphene-based ultrathin films and their tunable performances in organic nanoelectronics. Adv Funct Mater 2013;24:543–54.

[378] Zhong Z, Yao J, Low ZX, Chen R, He M, Wang H. Carbon composite membrane derived from a two-dimensional zeolitic imidazolate framework and its gas separation properties. Carbon 2014;72:242–9.

[379] Yao J, Wang H. Zeolitic imidazolate framework composite membranes and thin films: synthesis and applications. Chem Soc Rev 2014;43:4470–93.